Quantum Electrodynamics in Photonic Crystal Waveguides

Nielsen, Henri Thyrrestrup; Lodahl, Peter

Publication date:
2011

Document Version
Publisher's PDF, also known as Version of record

Quantum Electrodynamics in Photonic Crystal Waveguides

A dissertation
submitted to the Department of Photonics Engineering
at the Technical University of Denmark
in partial fulfillment of the requirements
for the degree of
philosophiae doctor

Henri Thyrrestrup Nielsen
April 18, 2011

Quantum Electrodynamics in Photonic Crystal Waveguides

Preface

This thesis presents work carried out in Quantum Photonics Group under the supervision of associate professor Peter Lodahl in the Department of Photonics Engineering at the Technical University of Denmark between April 2008 and April 2011. This thesis is mainly concerned with quantum electrodynamics (QED) effects in waveguides, although in a broad sense as a large part of it covers cavity QED effect in the Anderson localized regime of photonic crystal (PhC) waveguides. When I started the project, we set out to study a single photon source based on a PhC waveguide and a quantum dot emitter, which was relatively new concept. During a measurements series to verify our results on a set of new samples, we observed a series of random cavity peaks. This was quickly realized to be Anderson localization, thanks to Peter's interest in multiple scattering. There was already a small activity in the group related to multiple scattering, and disordered PhCs was already fabricated. At least for my part, this started the quest to study Anderson localization in PhC waveguides. I would like to thank Peter for introducing me to the interesting but sometimes confusing field of multiple scattering and Anderson localization.

The content of the thesis has been carried out in collaboration with many people. First, I would like to thank my supervisor Peter for general supervision, ideas, and discussions. During most of my Ph.d. I worked closely with Luca Sapienza, and I will especially like to thank him for the collaboration on the QED experiments and his unlimited patience in reading and correcting articles drafts and for general discussions. The project in the present form would not have been possible without the samples and both the initial waveguide samples, and the disordered samples were fabricated by Søren Stobbe. The final statistical measurements on disordered PhC used in the thesis were performed by Kristian Romlund Rix and Tau Bernstorff Lehmann. I have also had the

privilege to work with Stephan Smolka, who provided the one-dimensional optical model in Sec. 3 and helped with analyzing the statistical data. His never ending optimism has been a great inspiration, and I am grateful for the many discussions on multiple scattering. Philip Kristensen has been a helpful support in developing the density of state cavity coupling model in Sec. 3.

I am also grateful for the general collaborating atmosphere in the Quantum Photonics, and would like to also express my appreciations towards: Serkan Ates, Jin Liu, Mads Lykke Andersen, Qin Wang, David Garcia-Férnandez, Kristian Høeg Madsen and Immo Söllner. I have enjoyed the many discussions; both scientific and nonscientific. Before the Ph.d. I made my Master project in the Quantum Photonics group as well, which spawn the interest in optical experiments and I was introduced to Picolab by Toke Lund-Hansen and Brian Julsgaard whose skillful approach to alignment has been a big inspiration.

During my Ph.d. some of my collages have become good friends; especially Elaine Barretto, Martin Schubert, Stephan Smolka, Jin Liu, Pernille Klarskov and Roza Shirazi whose company I have enjoyed, both on an off campus, and I appreciate their support during the three years.

Abstract

In this thesis we have performed quantum electrodynamics (QED) experiments in photonic crystal (PhC) waveguides and cavity QED in the Anderson localized regime in disordered PhC waveguides. Decay rate measurements of quantum dots embedded in PhC waveguides has been used to map out the variations in the local density of states (LDOS) in PhC waveguides. From decay rate measurements on quantum dot lines temperature tuned in the vicinity of the waveguide band edge, a β-factor for a single quantum dot of more then 85% has been extracted. Finite difference time domain simulations (FDTD) for disordered PhC waveguides have been used to confirm the existence of a densely packed spectrum of strongly confined Anderson localized modes near the waveguide band edge. An one-dimensional disordered model is used to model the statistical properties of Anderson localized modes. As the localization lengths decrease, a simultaneous increase in the average Q-factor and decrease in mode volume is observed, which leads to a large probability of observing strong coupling in disorder PhC waveguides. The effect of losses is shown to reduce the largest Q-factors in the distribution and drastically lower the strong coupling probability. The Q-factor distributions of Anderson localized modes have been measured in PhC waveguides with artificial induced disorder with embedded emitters. The largest Q-factors are found in the sample with the smallest amount of disorder. From a comparison with the waveguide model the localization length is shown to increase from $3-7$ μm for no intentional disorder to 25 μm for 6% disorder. A distribution of losses is seen to be necessary to explain the measured Q-factor distributions. Finally we have performed a cavity QED experiment between single quantum dots and an Anderson localized mode, where a β-factor of 94% has been measured.

Resumé

I denne afhandling har vi udført kvante-elektrodynamiske (QED) målinger i fotoniske krystal bølgeledere og kavitets-QED i det Anderson lokaliserede regime i uordentlige fotoniske krystal bølgeledere. Henfaldsmålinger af kvantepunkter indlejret i fotoniske krystal bølgeledere er blevet brugt til at kortlægge variationer i den lokale tilstandstæthed. Henfaldskurver målt på temperaturtunede kvantepunkter i nærheden af båndkanten for en fotonisk krystal bølgeleder er brugt til at udtrækket en β-faktor på over 85% for et enkelt kvantepunkt. Der er udført finite difference time domain (FDTD) simuleringer af ordnede fotoniske krystal bølgeledere. De viser at der et tæt pakket spektrum af kraftigt lokaliserede Anderson tilstande i nærheden af båndkanten for uordnede fotoniske krystal bølgeleder. En en-dimensionel model for uordnede bølgeledere er brugt til at modellere de statistiske egenskaber af Anderson lokaliserede tilstande. Det er observeret at en formindskelse af lokaliseringslængden både giver en stigning i den gennemsnitlige Q-faktor og et fald i mode-volumenet. Det resulterer i en stor sandsynlighed for at observere stærk kobling i uorden fotoniske krystal bølgeledere for små lokaliseringslængder. Det er vist at tab reducerer den største Q-faktorer i fordelingen og drastisk sænker sandsynligheden for at observere stærke kobling. Q-faktor distributioner for Anderson lokaliserede tilstande er blevet målt i fotoniske krystal bølgeledere med indlejrede kvantepunkter og med kunstig induceret uorden. De største Q-faktorer er fundet i prøver med kun fabrikationsuorden. Ved at sammenligne de målte Q-faktor distributioner med de tilsvarende i modellen er det vist at lokaliseringslængden stiger fra $3-7$ μm for en prøver uden uorden til 25 μm for 6% uorden. Det er vist at en fordeling af tab er nødvendig for at forklare de målte Q-faktor distributioner. Til sidst har vi udført kavitets-QED målinger for et enkelt kvantepunkt koblet til en Anderson lokaliseret mode hvor en β-faktor på 94% er blevet målt.

List of Publications

The work performed in the work of this Ph.D.-project has resulted in the publications listed below:

Journal Publications

1. T. Lund-Hansen, S. Stobbe, B. Julsgaard, H. Thyrrestrup, T. Sünner, M. Kamp, A. Forchel, P. Lodahl, *Experimental Realization of Highly Efficient Broadband Coupling of Single Quantum Dots to a Photonic Crystal Waveguide*, Physical Review Letters, **101**, 113903 (2008).

2. L. Sapienza, H. Thyrrestrup, S. Stobbe, P.D. Garcia, S. Smolka, P. Lodahl, *Cavity Quantum Electrodynamics with Anderson-Localized Modes*, Science, **327**, 1352 (2010).

3. H. Thyrrestrup, L. Sapienza, P. Lodahl, *Extraction of the beta-factor for single quantum dots coupled to a photonic crystal waveguide*, Applied Physics Letters, **96**, 231106 (2010).

4. Q. Wang, S. Stobbe, H. Thyrrestrup, H. Hofmann, M. Kamp, T. W. Schlereth, S. Höfling, and P. Lodahl, *Highly anisotropic decay rates of single quantum dots in photonic crystal membranes*, Optics Letters, **35**, 2768 (2010).

Journal Publications in Preparation

1. S. Smolka, H. Thyrrestrup, L. Sapienza, T.B. Lehmann, K.R. Rix, P.T. Kristensen, L.S. Froufe-Pérez, P.D. Garcia, P. Lodahl, *Probing statistical properties of Anderson localization with quantum emitters*, arXiv, *arXiv:1103.5941v1* (2011).

2. H. Thyrrestrup, S. Smolka, P.T. Kristensen, L. Sapienza, P. Lodahl, *Light-matter coupling between single emitters and Anderson-localized modes in one-dimensional disordered systems*, In preparation.

Conference Contributions

1. P. Lodahl, L. Sapienza, H. Thyrrestrup, S. Stobbe, P. D. Garcia, S. Smolka, *Cavity Quantum Electrodynamics in Disordered Photonic Crystals*, PECS IX, Granada, Spain, (2010).

2. L. Sapienza, H. Thyrrestrup, S. Stobbe, P. D. Garcia, S. Smolka, P. Lodahl, *Spontaneous emission of quantum dots in disordered photonic crystal waveguides*, International Conference on Physics of Semiconductors, Seoul, Korea, (2010).

3. L. Sapienza, H. Thyrrestrup, S. Stobbe, P. D. Garcia, S, Smolka, P. Lodahl, *Spontaneous emission of quantum dots in disordered photonic crystal waveguides*, SPIE NanoScience + Engineering, California, USA, 2010

4. L. Sapienza, H. Thyrrestrup, S. Stobbe, P. D. Garcia, S. Smolka, P. Lodahl, Cavity Quantum Electrodynamics in the Anderson-localized Regime, CLEO/QELS, San Jose, California, USA, (2010).

5. J. Mørk, W. Xue, F. Öhman, P.K. Nielsen, H.T. Nielsen, T. Roland, *Exploring carrier dynamics in semiconductors for slow light*, IEEE LEOS Winter Topicals, Innsbruck, Austria, (2009).

6. H. Thyrrestrup, T. Lund-Hansen, P. Lodahl, *Tuning the Coupling of a Single Quantum Dot to a Photonic Crystal Waveguide*, CLEO/IQEC, Baltimore, USA, (2009).

7. H. Thyrrestrup, T. Lund-Hansen, P. Lodahl, *Direct measurement of the coupling between a single quantum dot and a photonic crystal waveguide by temperature tuning*, PECS VIII, Sydney, Australien, (2009).

8. M. Schubert, L.H. Frandsen, T. Suhr, T. Lund-Hansen, H. Thyrrestrup, P. Lodahl, J.M. Hvam, K. Yvind, *Sub-threshold wavelength splitting in coupled photonic crystal cavity arrays*, PECS VIII, Sydney, Australien, (2009).

9. M. Schubert, L.H. Frandsen, T. Suhr, T. Lund-Hansen, H. Thyrrestrup, M. Bichler, J.J. Finley, P. Lodahl, J.M. Hvam, K. Yvind, *Sub-threshold investigation of two coupled photonic crystal cavities*, CLEO/IQEC, Baltimore, USA, (2009).

10. H. Thyrrestrup, T. Lund-Hansen, P. Lodahl, *Purcell enhanced coupling of quantum dot emission to photonic crystal nano-cavities*, Danish Physical Society annual meeting, Nyborg, Denmark, 2008

Contents

Chapter 1

Introduction

At the core of mesoscopic quantum optics is quantum electrodynamics (QED) with its description of light matter–interaction. Already in the simplified model where a two-level emitter interacts with the quantized electromagnetic vacuum field leads to a number of interesting phenomena. This includes spontaneous emission, the electromagnetic Lamb shift, and Rabi flopping, where the excitation oscillates between the emitter and a single photon of the electromagnetic field. All of these phenomena depend on the optical density of states seen by the emitter. Rabi flopping is only realized in the limit of a strongly varying density of states where the emitter is strongly coupled to a single optical mode. This has been realized in cavity QED systems, with for example atoms [1], ions [2], and semiconductor quantum dots [3, 4, 5]. Cavity QED has been used to generate entangled emitter–photon states and thus constitutes a fundamental building block in quantum information devices [6].

Another key component in quantum information and quantum cryptography is a single photon source, where (coherent) single photons are emitted on demand into a well-defined mode [7]. Harvesting photons into a single mode has typically been done by embedding an emitter into a resonant, but weakly coupled cavity. This is done because of the strong field enhancement and the consequently enhanced spontaneous emitter decay rate into the cavity mode. The large decay rate improves both the coupling efficiency to the targeted mode and the coherence of the emitted photon due to the shorter interaction time with decoherence processes in the emitter. One disadvantage of cavities entails

that any emitted photons propagate out-of-plane as a result of their geometry. It defies the general idea of on-chip quantum computing where it is desirable that the photons decay into an in-plane propagating mode. In fact, the effect of enhanced emission rates, due to the local density of optical states, is not limited to confined modes, but can be achieved in open systems. When the emitter interacts with a slowly propagating mode the same effect can take place, as shown by Keppler for metallic nano-wires [8]. This can also be achieved in photonic crystal (PhC) waveguides [9, 10] where slow light propagation is obtained for the propagating mode near the band edge. An advantage of this is that the dispersion of the propagating mode can be tailored to design the light matter interaction [11].

Multiple scattering is a general wave phenomenon that has implications in many fields. In three-dimensional disordered systems the ensemble averaged light propagation is normally described by a diffusion process where light spreads out over time [12]. However, for very pronounced scattering, when the mean free path is on the order of the wavelength, interference effects survive the ensemble averaging and light can localizes around the source with a characteristic localization length [13, 14]. In three-dimensional system, this requirement is in general difficult to achieve. For lower dimensional systems the lower propagation phase space makes it easier and Anderson localization has been observed in various systems with light [15, 16], in matter waves [17] and with sound [18]. In one-dimensional systems light always localizes for infinite samples.

The strong fields in both cavity QED and slow light waveguides have many applications where strong light matter interaction is desired, e.g. for non-linear interactions [19] sensing applications [20] and quantum information science. It also means that the interaction with disorder is enhanced and disorder in such nano-structured devises are normally seen as a nuisance that leads to excessive losses. Especially in cavity QED systems disorder is detrimental, as highly engineered cavities with nano-scale accuracy are needed. As discussed, disorder also result in multiple scattering events and in disordered PhC waveguide structures this can lead to strongly localized modes. This thus offers an alternative route to light confinement for QED experiments where disorder is not seen as a nuisance but as a resource.

The outline of he thesis: In Chapter 2, the coupling between an emitter and

a PhC waveguide mode is described and it is shown experimentally that single quantum dots can couple to the waveguide mode over a broad frequency range with very high efficiency. Tuning of the transition energies of the quantum dots in the vicinity of the band edge is used to extract the single quantum dot coupling efficiencies and map out the band edge density of stats. Chapter 3 discusses the effect of disorder in PhC waveguides and shows that strongly confined Anderson localized modes are formed near the PhC band edge. A model is used to study the statistical properties of one-dimensional disordered media and a theory for the non-Markovian dynamics between the confined modes and an emitter is described. The local density of states (LDOS) is used as the fundamental coupling parameter. At last, the probability distributions of the light confinement factors and coupling strengths for emitters to the confined modes are evaluated. Chapter 4 describes measurements where the statistical properties of Anderson localized modes are studied by embedding emitters into intentionally disordered PhC waveguides. The measured spectral distributions are compared to a statistical model from which both the localization and loss length are extracted. Finally we report on QED experiments where single quantum dots are coupled to an Anderson localized modes. In Chapter 5 the conclusions are presented.

Chapter 2

Extraction of the β-Factor for Single Quantum Dots in Photonic Crystal Waveguides

2.1 Introduction

Photonic crystals are periodic dielectric media that have been extensively studied in the literature due to their exciting properties to strongly confine light to a size on the order of the wave length [21]. For certain realizations of PhCs the reflection off the periodic interfaces will lead to destructive interference in all directions. In this case, the propagation of electromagnetic fields inside the PhC can be completely prohibited in certain frequency bands, co-called band gaps. Introducing defects in such structures can create localized optical states bound to the defects with frequencies inside the otherwise empty band gaps. Defects can either be point defects or line defects. In point defects light is confined in all dimensions of the PhC forming a cavity structure whereas line defects form a waveguide in which light can propagate. PhC waveguides has gained a of lot of interests due to the ability to engineer the dispersion of the

waveguide mode and in this way slow down the group velocity of the propagating wave to almost zero [11]. For low group velocities the interaction time between the slow light wave and the surrounding material increases. Slow light has been predicted to increase non-linear effects [22], to increases scattering losses on imperfections from the ideal crystal structure [23], and to increase the interaction with embedded emitters [9]. PhC waveguides can therefore act as efficient collectors of the emitted photons and form the basis of a on-chip in-plane single photon source. In the chapter we first describe the light propagation and spontaneous emission in PhC waveguides. We then describe and analyze our experiments - to the best of our knowledge the first experiments where single emitters have been coupled to a waveguide mode.

2.1.1 Photonic Crystal Waveguides

The dielectric function for a PhC fulfill $\varepsilon(r) = \varepsilon(\boldsymbol{r} + \boldsymbol{R})$ where $\boldsymbol{R} = n\boldsymbol{a}_1 + m\boldsymbol{a}_2 + l\boldsymbol{a}_3$ and $(\boldsymbol{a}_1, \boldsymbol{a}_3, \boldsymbol{a}_3)$ is a set of lattice vectors and (n, m, l) are integers. Photonic crystals with lower dimensions than three can be obtained by letting any of the lattice vectors be zero. In this case the periodicity only occurs along the remaining lattice vectors and for the rest of the dimensions the structure is translationally invariant. The length of the lattice vectors determine the periodicity. One can construct a reciprocal lattice where the lattice vectors $\boldsymbol{G}$ fulfill $\boldsymbol{G} \cdot \boldsymbol{R} = 2\pi N$ and a Fourier transform of any solution to Maxwell's equations in the periodic structure can be expanded using only these vectors.

The calculation of electromagnetic modes in periodic structures can be simplified by using Bloch's theorem, which is described in more details in Ref. [21]. Using this theorem the electric and magnetic fields can be written on the Bloch form, $\boldsymbol{H}_{\boldsymbol{k}}(\boldsymbol{r}) = \mathrm{e}^{i\boldsymbol{k}\cdot\boldsymbol{r}} u_{\boldsymbol{k}}(\boldsymbol{r})$ and $\boldsymbol{E}_{\boldsymbol{k}}(\boldsymbol{r}) = \mathrm{e}^{i\boldsymbol{k}\cdot\boldsymbol{r}} u_{\boldsymbol{k}}(\boldsymbol{r})$, where $u_{\boldsymbol{k}}(\boldsymbol{r})$ is a periodic function with the same periodicity as the dielectric function $u_{\boldsymbol{k}}(\boldsymbol{r}) = u_{\boldsymbol{k}}(\boldsymbol{r}+\boldsymbol{R})$ and $\boldsymbol{k}$ is a wave vector in the crystal that labels the specific state. As a result of the periodicity it is only necessary to calculate for $\boldsymbol{k}$-vector in a region of the first Brillouin zone as solution for larger k-values can be mapped back into this k-vector region by adding a lattice vector. These states form higher order bands in the first Brillouin zone and we can label them by their band number. For a rectangular lattice with lattice constant a_i in the i-direction the edge of the first Brillouin zone is at $k_i = \pm\pi/a_i$.

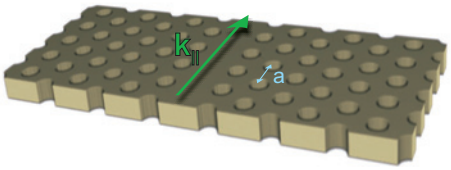

Figure 2.1: Sketch of a PhC membrane waveguide showing 5 periods of the waveguide structure (the 5 missing holes along the green arrow).

Inserting the Bloch form into the wave equation for the $\boldsymbol{H}$-field

$$\nabla \times \left(\frac{1}{\varepsilon(\boldsymbol{r})} \nabla \times \boldsymbol{H}(\boldsymbol{r}) \right) = \left(\frac{\omega}{c} \right)^2 \boldsymbol{H}(\boldsymbol{r}) \tag{2.1}$$

we obtain the following equation

$$(i\boldsymbol{k} + \nabla) \times \frac{1}{\varepsilon(\boldsymbol{r})} (i\boldsymbol{k} + \nabla) \times \boldsymbol{u}_{\boldsymbol{k}}(\boldsymbol{r}) = \left(\frac{\omega(\boldsymbol{k})}{c} \right)^2 \boldsymbol{u}_{k}(\boldsymbol{r}), \tag{2.2}$$

which is an eigenvalue problem in $\boldsymbol{u}_{\boldsymbol{k}}$ with $\omega(\boldsymbol{k})$ as eigenfrequencies. The operator in the equation is Hermitian, which insures that the eigenfrequencies $\omega(\boldsymbol{k})$ are strictly positive. And since $\boldsymbol{k}$ is a continuous variable the states form a band. We have solved the eigenvalue problem in Eq. (2.2) using the MPB software package [24]. The equivalent equations in the $\boldsymbol{E}$-field are not Hermitian and the $\boldsymbol{H}$-field is therefore mostly used in numerical calculations. The $\boldsymbol{E}$-field can be obtained afterwards from

$$\boldsymbol{E}(\boldsymbol{r}) = \frac{i}{\omega \varepsilon_0 \varepsilon(\boldsymbol{r})} \nabla \times \boldsymbol{H}(\boldsymbol{r}). \tag{2.3}$$

In this thesis we consider the propagation of light in a PhC membrane waveguide, as sketched in Fig. 2.1. It consists of a thin membrane in which a number of air holes have been introduced. The holes are arranged in a 2D hexagonal PhC lattice with a lattice constant a. The band structure for the 2D hexagonal lattice without the waveguide can be calculated by considering the hexagonal primitive unit cell containing one air hole. The type of waveguide we have focused on is formed by removing a single row of holes along one of the principal axes of the crystal. To ease discussion we introduce an xyz-coordinate system where the x-direction is along the waveguide, the y-direction is the in-plane direction orthogonal to the waveguide and the z-direction is out of the

plane. The membrane PhC is a special case of a 2D PhC. The membrane lacks translational symmetry in the z-direction and the presence of the waveguide itself breaks the periodicity of the PhC in the y-direction. However, since the MPB software requires periodic boundary conditions we use a rectangular super cell in the y and z-direction large enough to make the artifacts of the periodic boundary conditions negligible. The x-direction is periodic so we only need to calculate for $\boldsymbol{k} = (k_x, 0, 0)$ where $k_x = [0, \pi/a]$ is in the first Brillouin zone. The simulated structure will effectively consist of an infinity set of waveguides but as we are only interested in modes confined to the waveguide structure and the effect of the periodic boundaries fall off exponentially with the size of the super cell. With the increase in super cell size the number of bands that we need to calculate to reach the interesting waveguide bands increases due to band folding. We found that a super cell, which consists of 7 row of holes on either side of the waveguide and 2 lattice constant above the membrane was sufficient to the make the cross talk between periodic images negligible.

In Fig. 2.2a we have plotted the band structure for the PhC membrane waveguide with hole radius $r = 0.29a$, membrane thickness $h = 0.59a$ and refractive index 3.44. The lattice constant a can be freely chosen since Maxwell's equations are scale invariant. We have plotted the band structure along the k_x-direction to the edge of the first Brillouin zone $k_x = [0, \pi/a]$ since this is region relevant for the propagation along the waveguide. The shaded/colored areas mark the projected band structure from all other $\boldsymbol{k}$-vectors and here a continuum of modes exist. The plot only shows modes that have an even mirror symmetry around the $z = 0$ plane as the odd modes do not have an in-plane band gap for the hexagonal lattice. The lines with blue background show the index guided bands of the membrane where the electric field is extended in the membrane. States above the light line $\omega = k_x c$, marked by the blue area, are not guided by total interval refraction inside the membrane and they form a continuum set of modes that propagation out the structure. Coupling to these modes results in radiation losses. Below the light line we see a gap in the index guided modes approximately between $\nu = 0.25 - 32a/\lambda$ where there are no states, this corresponds to the band gap of the PhC. 2D membrane PhCs do not have a complete band gap as there is still states at these frequencies above the light line. The waveguide defect introduces several states below the light line where light is confined to the waveguide and propagate along the

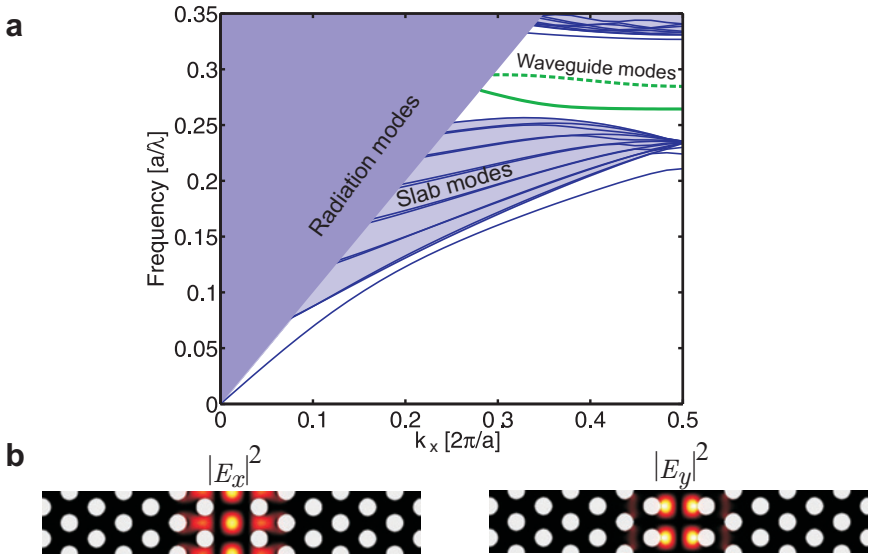

Figure 2.2: (a) Projected band structure for k-vectors parallel to a PhC waveguide membrane with $r = 0.29a$, $h = 0.59a$ showing the even modes in the z-direction perpendicularly to the membrane. States above the light cone $\omega = k_x c$ form a continuum of radiation (dark blue area). Below the light cone are the slab guide mode (blue lines). In the band gap of the 2D PhC are the two gap guided waveguide, and at the lowest frequencies below there are three index guided waveguide modes (b) Electric field intensity distributions for the two in-plane x and y polarization for the eigenmodes at the band edge $k_x = \pi/a$ of the first gap guided waveguide mode (solid green line).

x-direction. Below the slab modes are three index guided waveguide modes, although only the first one is index guided for all k-vectors along the propagation direction. Inside the band gap are there three gap guided modes. The two modes that are the most interesting for applications are marked by green lines, whereas the third is only weakly confined to the waveguide. In the following we will focus on the gap guided mode with the lowest frequency (solid green line).

The propagation of a given state $(\boldsymbol{k}, \omega_k)$ is determined by the group velocity $v(\boldsymbol{k}) = \nabla_{\boldsymbol{k}}\omega(\boldsymbol{k})$ and the group velocity along the waveguide is therefore $v(\boldsymbol{k}) = \partial_{k_x}\omega(k_x)$. The group velocity vanishes at the edge of the Brillouin zone and

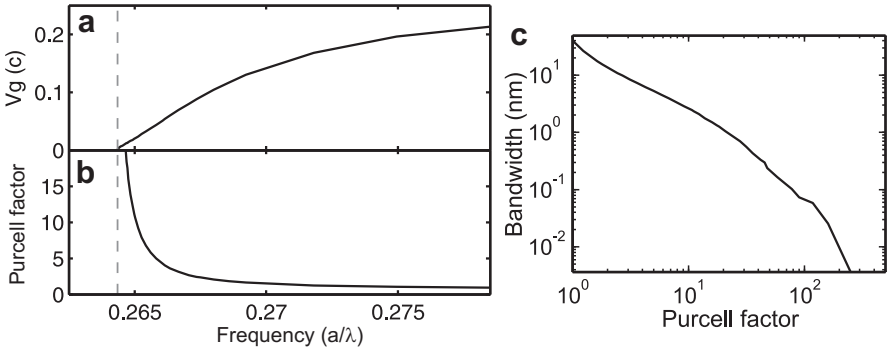

Figure 2.3: (a) Group velocity of the first gap guide mode of a PhC waveguide. (see text for parameters) (b) Purcell factor for a emitter located at field antinode for the same mode. (c) Wavelength bandwidth for a given minimum Purcell factor.

there the modes are standing waves. Especially, the first gap guided mode show a very flat band. This flat region we denote the slow light regime. Since no propagating states exist for lower frequencies we will often refer to this cut-off as the band edge of the waveguide mode. The group velocity in the interval from the light line to the band edge is plotted in Fig. 2.3a where the dashed line marks the band edge. The group velocity decreases monotonously from $0.2c$ near the light line down to zero at the band edge.

From the solution of the eigenvalue problem we also get the electromagnetic field distribution for the eigenmodes. In Fig. 2.2b we have plotted the electric field intensity for two unit cells along the waveguide for the two possible polarizations of the electric field $|\boldsymbol{f}_{\boldsymbol{k}_\omega}(\boldsymbol{r}) \cdot \boldsymbol{e}_y|^2$ and $|\boldsymbol{f}_{\boldsymbol{k}_\omega}(\boldsymbol{r}) \cdot \boldsymbol{e}_x|^2$ for $k_x = \pi/a$, where we have renamed the electric field eigensolutions as $\boldsymbol{f}_{\boldsymbol{k}_\omega}(\boldsymbol{r})$. Traditionally one plots the $\boldsymbol{H}_z(\boldsymbol{r})$-field for the even modes as only one component is needed to show the field profile. To assess the coupling to embedded emitters it is more natural to plot the $\boldsymbol{E}$-field intensity. We see that the mode is indeed strongly localized to the waveguide only extending out to the second row of holes and is divided into regions that are strongly polarized in either the x- or y-direction.

2.1.2 Light Emitter Coupling in Photonic Crystal Waveguides

If an emitter is embedded into the an inhomogeneous medium the spontaneous emission rate of the emitter will be modified due to the change in the number of states the emitted photon can decay into. It can be described by the projected local density of states

$$\rho(\omega, \boldsymbol{r}_e) = \sum_{\mu} |\boldsymbol{f}_\mu(\boldsymbol{r}_e) \cdot \boldsymbol{d}|^2 \delta(\omega - \omega_\mu), \tag{2.4}$$

It a given as a sum of delta functions over the properly normalized plane waves evaluated at the emitter position $\boldsymbol{f}_\mu(\boldsymbol{r}_e)$ and projected onto the normalized dipole moment of the emitter $\boldsymbol{d}$. Given a LDOS the spontaneous emission rate or the radiative rate of an excited emitter can be calculated as (Eq. (3.34))

$$\Gamma = \frac{\pi \omega d^2}{\varepsilon_0 \hbar} \rho(\omega, \boldsymbol{r}) \tag{2.5}$$

where d is the magnitude of the dipole moment. See Sec. 3.4.1 for a deviation. It is instructive to normalize the decay rate to the spontaneous emission rate in a homogenous medium to get the Purcell factor $F_p = \Gamma / \Gamma_{\text{hom}}$, where

$$\Gamma_{\text{hom}}(\omega) = \frac{n \omega^3 d^2}{3\pi^2 \varepsilon_0 \hbar c^3} \tag{2.6}$$

and n is the refractive index. The Purcell factor is traditionally used to quantify the coupling of an emitter to a localized mode where large Purcell factors can be obtained in a narrow frequency bandwidth [25]. In contrast, inside the band gap of defect free PhCs the Purcell factor can be greatly suppressed [26].

We can calculate the density of states for a waveguide by using that waveguide modes fulfill the periodic boundary condition, $ka = 2\pi m$, where k is the wave number, a is the lattice constant and m is an integer. We can calculate the density of states as [8]

$$\rho_{\text{wg}}(\omega) = 2\frac{\partial m}{\partial \nu} = 2\frac{\partial m}{\partial k}\frac{\partial k}{\partial \nu} = 2\frac{a}{2\pi v_g}, \tag{2.7}$$

where we have used that the group velocity is $v_g = \partial k / \partial \nu$ and $\nu = \omega / 2\pi$ is the frequency. The factor of 2 accounts for the forward and backward propagation

in the waveguide. Since we are only considering a single bound waveguide mode we can approximate the LDOS by multiplying $\rho_{wg}(\omega)$ with $|\boldsymbol{f}_{k_\omega}(\boldsymbol{r})\cdot\boldsymbol{d}|^2$

$$\rho_{\mathrm{wg}}(\omega,\boldsymbol{r}) = \frac{a}{v_g\pi}|\boldsymbol{f}_{k_\omega}(\boldsymbol{r})\cdot\boldsymbol{d}|^2 \tag{2.8}$$

and we obtain the Purcell factor for the emission into the waveguide mode

$$F_p(\boldsymbol{r}) = \Gamma_{\mathrm{wg}}/\Gamma_{\mathrm{hom}} = \frac{3\pi c^3 a}{n\omega^2 v_g}|\boldsymbol{f}_{k_\omega}(\boldsymbol{r})\cdot\boldsymbol{d}|^2. \tag{2.9}$$

This expression is identical to the one derived using a Dyadic Greens function approach in Ref. [10] and with a similar result obtained in Ref. [9]. Note that the group velocity is in the denominator, which shows that the highest Purcell factor is obtained in the slow light regime of the waveguide mode. As v_g approaches zero right at the band edge, the Purcell factor diverges. The Purcell factor also depends on the field intensity $|\boldsymbol{d}\cdot\boldsymbol{f}_{k_\omega}(\boldsymbol{r})|^2$ plotted for two perpendicular dipole polarizations in Fig. 2.2b at the band edge. We see that both the x and y polarized dipoles couple to the waveguide mode but at different spatial positions. Following Ref. [10] we can evaluate the maximum Purcell factor

$$F_{p,\max} = \frac{3\pi c^3 a}{n^3\omega^2 v_g V_{\mathrm{eff}}}, \quad V_{\mathrm{eff}} = \frac{1}{\max_{\boldsymbol{r}}\{n(\boldsymbol{r})^2|\boldsymbol{f}_{k_\omega}(\boldsymbol{r})|^2\}} \tag{2.10}$$

by introducing an effective volume pr. lattice constant V_{eff}. For the mode shown in Fig. 2.2b the mode volume is calculated to $V_{\mathrm{eff}} = 0.384a^3$. In Fig. 2.3b the Purcell factor is plotted for an emitter maximally coupled to the waveguide described earlier Sec. 2.1.1. We see a divergence at the band edge. Another characteristics of PhC waveguides, compared to cavities, is the large frequency bandwidth in which a large Purcell factor can be obtained. In the Fig. 2.3c we see that a minimum Purcell factor of 1 can be achieved over a 30 nm bandwidth and a Purcell factor larger then 10 can be obtained over several nanometers.

We have sketched the LDOS for a PhC with the accurate position of the band gap and the LDOS for a PhC waveguide in Fig. 2.4, for the same parameters used in the previous plots. For frequencies far away from the band gap the LDOS for a homogenous medium (Eq. (2.6)) with the refractive index of the membrane has been used, which is a good description for wavelengths that are either much larger of smaller than the lattice constant. It is very challenging to calculate the LDOS in a PhC membrane since it depends strongly on the

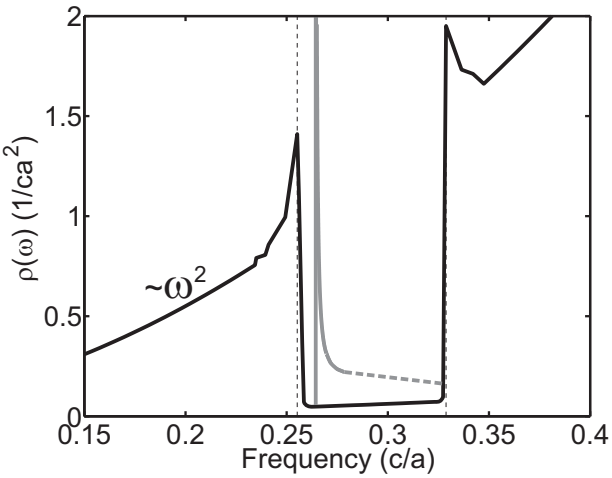

Figure 2.4: Sketch of the density of states for a PhC showing the band gap (black line) and the density of states for the waveguide (gray line).

position and polarization of the emitter. The calculation also needs to take into account the scattering from all the membrane holes and the coupling to radiation modes. A few attempts have been made to perform this calculation but for this sketch we have taken a simple approach and use a homogenous LDOS divided by 20, which is a good approximation [27]. Following Ref. [27] we also plot an enhancement near the band edges. The waveguide is shown with the LDOS from Eq. (2.8) in the interval from the band edge to the light line. The dashed line is an extrapolation of the waveguide contribution into the light line.

Coupling Efficiency

In addition to the Purcell factor, the so-called β-factor is another important parameter to quantify the coupling of a quantum dot to the PhC waveguide. The β-factor is defined as

$$\beta = \frac{\Gamma_{\mathrm{wg}}}{\Gamma_{\mathrm{wg}} + \Gamma_{\mathrm{rad}} + \Gamma_{\mathrm{nrad}}}. \tag{2.11}$$

It quantifies the relative contribution to the decay rate due to the waveguide mode Γ_{wg} compared to all other decay channels for the emitter and it gives

an estimate of the coupling efficiency of emitted photons into the waveguide mode. Γ_{rad} includes all radiative rates into all other modes and Γ_{nrad} contains any non-radiative contributions. From Eq. (2.11) we see that to increase β we can either increase the decay rate into the waveguide through the Purcell effect as described above or decrease either of the two rates in the denominator. For PhC waveguides the decay rate to radiation modes is already suppressed in the band gap of the PhC as shown in Fig. 2.4. We can therefore achieve a very large β-factor into the propagating waveguide mode with a modest Purcell factor. As an example we use realistic parameters of $\Gamma_{\mathrm{rad}} = 0.05\ \mathrm{ns}^{-1}$ inside the band gap and a quantum efficiency of 0.9 for a semiconductor quantum dot in a homogenous medium $\Gamma_{\mathrm{nrad}} = 0.1\ \mathrm{ns}^{-1}$ [28]. To achieve a β-factor of 95% we need a Purcell factor of $F_p = 2.9$. This can be obtained in a bandwidth of around 10 nm for the parameters used in Fig. 2.2 and an emitter located at the antinode of the field. PhC waveguides thus take advantage of both an enhanced Purcell factor and the suppression of the radiative modes to enhance the β-factor.

Alternative waveguide structures that have been used to collect photons into propagating modes mostly relies on one of the two effects, either suppression of radiative modes or enhancement of the Purcell factor. In plasmon waveguides the coupling to radiation modes is similar to their bulk values and the coupling to ohmic losses in the metallic nano-wires increases Γ_{nrad} [29]. So a much larger Purcell factor is needed to obtain the same coupling efficiency. Recently thin dielectric nano-wires have been used to obtain high β-factors, which mainly rely on the effect of decreasing the coupling to radiation modes but with less emphasis on the Purcell factor [30].

2.2 Experimental Verification with Embedded Quantum Dots

We now study the variations in the density of states for PhC waveguide experimentally and compare these to our predictions. We furthermore estimate the collection efficiency of the spontaneous emission from quantum dots into the waveguide modes. We are especially interested in the slow region where the coupling efficiency is predicted to diverge.

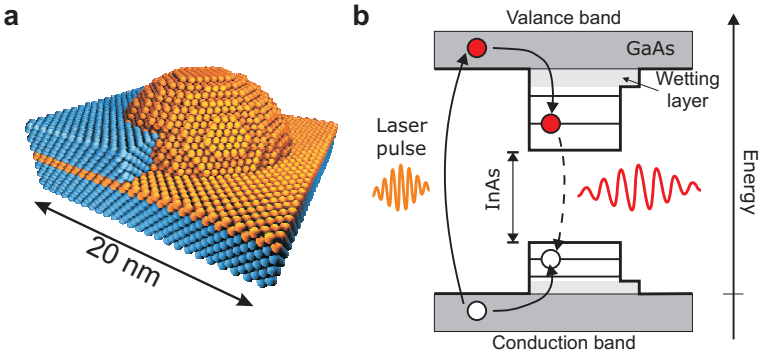

Figure 2.5: (a) Sketch of the physical composition of a quantum dot, constructed from a low band gap semiconductor island (yellow) embedded in a semiconductor with larger band gap (blue). The layer underneath the quantum dots is the wetting layer. (b) Semiconductor band edge level diagram for the valance and conduction band for a cut through a InAs quantum dot embedded in GaAs. The strong confinement inside the quantum dot creates discrete energy levels. The arrows show the standard non-resonant excitation scheme with a laser pulse followed by subsequently relaxation of the exciton pair into the quantum dot and finally single photon spontaneous emission from the excited quantum dot.

2.2.1 Semiconductor Quantum Dots

As emitters, we use self-assembled semiconductor quantum dots which consist of InAs nano-scale islands embedded in a GaAs host material as sketch in Fig. 2.5a. They provide a set of discrete levels and in many way behave like artificial atoms and have excellent optical properties with high emission quantum efficiency. This type of quantum dots is grown using a molecular beam epitaxy (MBE) process where single mono-layers of InAs are deposited one layer at a time on a GaAs substrate. The two semiconductors have different lattice constant and above a critical thickness of the InAs layer the induced lattice strain releases by forming small islands on top of a few atom thick wetting layer of $In_xGa_{1-x}As$. The formation is a statistical process, which leads to distribution of the dot sizes with a mean around $10-20$ nm in diameter and $3-5$ nm in hight. The different dot sizes result in an inhomogeneous broadened emission spectrum. Finally the sample is capped with GaAs to close all the dangling

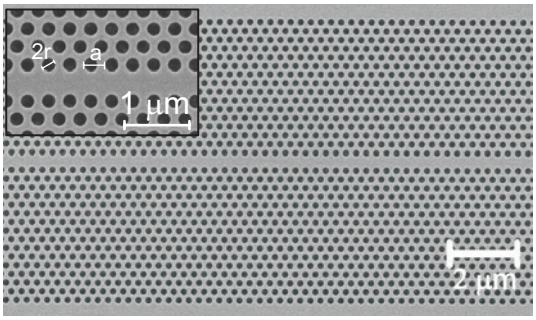

Figure 2.6: Two scanning electron microscope images of a PhC waveguide sample: A large area image and a close up of the area around the waveguide where the lattice constant a and the diameter $2r$ is marked.

bonds, which improves the optical properties. Since, InAs has a smaller band gap than GaAs and the dots provide a three dimensional potential well that confines the excitons stronger than the Coulomb interaction energy. This creates a discrete set of states for both the electrons and the holes as sketched in Fig. 2.5b. Despite the simple sketch, the quantum dot presents a complicated multi-particle spin fine-structure [31] that has profound implications for coherent experiments on quantum dots [32] and allow schemes to use quantum dots as spin-qubits for quantum computation. The first excited single-exciton state has four spin states: two optically active bright states with total angular moment of ± 1 and two optical dark states with total angular momentum ± 2, which lead to two decay components in the decay curve. The quantum dots can be optically excited by a non-resonant laser pumping above the GaAs band gap energy or into the continuum of wetting layer states. The electron-hole pair subsequently relaxes through a series of scattering processes into the first excited state of the quantum dot, from which it can spontaneously decay emitting a single photon. Quantum dots are thus promising candidates for single photons sources.

2.2.2 Active Photonic Crystal Waveguide Samples

The studied sample consists of a Gallium Arsenide (GaAs) PhC membrane with a triangular lattice of air holes, where one row has been left out to form the waveguide structure. The sample is fabricated on a GaAs wafer. An epi-

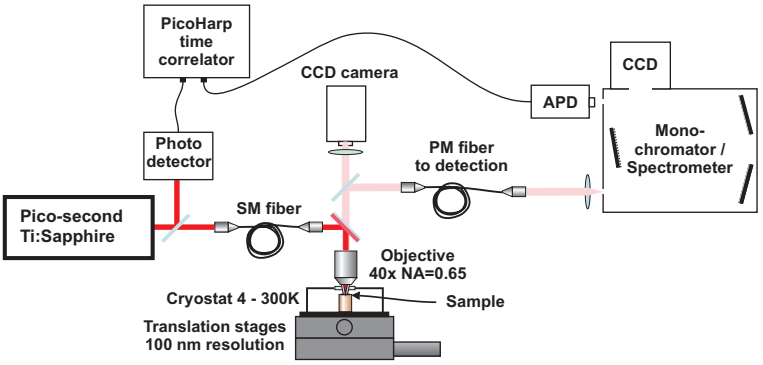

Figure 2.7: Sketch of the experimental setup, showing the important equipment. See text for a description of the individual components.

taxial structure is grown on top of the wafer that is composed of a 1 μm thick sacrificial layer of AlGaAs followed by a 150 nm thick GaAs layer. In the center of the top GaAs layer a single layer of self-assembled InAs quantum dots is grown. The dots have a density of 250 μm^{-2} and a center emission wavelength of 960 nm and an inhomogeneous broadening of 60 nm. The PhCs are fabricated by first patterning an electron sensitive mask with a E-beam followed dry etching to form the holes. The free standing membranes are created by selective wet etching the sacrificial AlGaAs layer with Hydroflouric acid through the holes. An example of the fabricated structures is seen in the SEM images in Fig. 2.6. The triangular PhC structure and waveguide is clearly visible. In the close up image, we see that the holes slightly deviate from perfect circles. And from SEM images of the cleaved membranes we know that these have a slight unintended roughness due to the wet etch. This roughness will lead to additional out-of-plane scattering losses and result in a small increase in the membrane thickness. In the simulations we have used a membrane thickness of 155 nm. For the measurements described in the following we used samples with a lattice constant of $a = 256$ and a hole radius of $r = 0.30a = 77$ nm. The samples are 7 μm wide and $L = 100$ μm long.

2.2.3 Experimental Setup

The experiential setup is sketched in Fig. 2.7. It consists of a confocal micro-photoluminescence setup where the sample is located in the a Helium flow cryostat and sits on a cold finger. Controlling both a heater beneath the sample and the Helium flow through the cryostat the temperature can be stabilized at any temperatures between 4.2 K and 300 K using a PID control. The sample is excited with a Coherent Mira tunable Ti:Sapphire laser operating in mode-locked pico-second mode with a repetition rate of 76 MHz and a pulse width of 2 ps. The laser is tunable in the range between 700 nm and 950 nm. For the present experiments the laser is tuned to 850 nm, which excites the quantum dots non-resonantly though the wetting layer states but below the band gap of GaAs. The sample is excited through a Nikon LWD 40xC objective with a NA=0.65 located outside the cryostat. The objective is corrected to focus correctly though the 1.5 mm thick cryostat window forming a excitation spot of 1.4 μm FWHM (Full Width at Half Maximum) on the sample. The photoluminescence from the quantum dots is collected from the top though the same objective and filtered though two long pass filters with cut off at 850 nm and 875 nm to filter out the laser light. The signal is then focused into a single mode polarization maintaining (PM) fiber that acts as a collection pin-hole, that image a 1.4 μm spot on the sample surface. A polarizing beam splitter before the fiber oriented perpendicular to the laser polarization rejects the remaining laser light. The collected light from the fiber is focused into to a 0.67 m spectrometer and directed to either a CCD camera or through a narrow slit to a avalanche photo detector (APD) for single photon counting. The setup is equipped with two different APDs: a PekinElmer with a time resolution of 280 ps and a MPD APD with a time resolution of 40 ps but with an approximately 6 times lower quantum efficiency. Using a 600 lines/mm grating we obtain a spectral resolution on the CCD of 0.1 nm. The spectral resolution on the slit depends on the slit width, but for the 50 μm used in the following experiments we obtain a resolution of 0.15 nm. By scanning the grating and continuously recording the arrival of photons on the APD we can build up a spectrum and in this way calibrate the grating angle to the wavelength at the exit slit. For time correlated photoluminescence experiments a quantum dot is repeatedly excited by the pulsed laser and the arrival times of the emitted photons from the quantum dot are correlated to the laser pulse using a Pi-

coHarp time correlator with an internal timing resolution of 4 ps. The real timing resolution are limited by the timing uncertainties of the APDs given by their instrument response function (IRF). A histogram of the arrival time differences between the emitted photons and the laser pulse is constructed to form a decay curve.

Since we are interested in measuring on quantum dots coupled to the propagating mode of the PhC waveguide we expect that a large fraction of the emitted photons are directed into the waveguide mode away from the detection optics. Only photons scattered out of plane is detected. It would be more suitable to directly measure at the end of the waveguide, which was not implemented at the time of the experiments. However, since the decay curves measure the total decay of the quantum dots into all modes it is still possible to obtain reliable indirect information on the coupling to the waveguide from the decay detected from the out-of-plane emitted photons

2.2.4 Broad Band Mapping of the Density of States

By measuring the radiative decay rates of a large set of single quantum dots we can map out the spectral variation in the LDOS of the waveguide as reported in Ref. [33]. In Fig. 2.8 we have plotted the measured decay rates for 26 single quantum dots located in the vicinity of the PhC waveguide structure over a large bandwidth of 40 nm. The solid line shows the calculated decay rate from the Purcell factor into the waveguide mode Eq. (2.10) using a homogenous decay rate of 1.1 ns^{-1}. A large fraction of the quantum dots show a decay rate of less than 0.2 ns^{-1}, which corresponds to quantum dots that are not coupled to the waveguide mode and whose decay are inhibited by the band gap of the PhC. The slowest decay rate observed is 0.05 ns^{-1}. The detection spot of 1.4 μm, much larger than the waveguide mode of a few hundred nanometer, means that some of the measured quantum dots are positioned outside the waveguide. However, a few quantum dots show decay rates larger than 0.5 ns^{-1} with the largest of 1.3 ns^{-1} near a frequency of $0.261a/\lambda$. The spectral position match with the enhanced density of states near the slow light regime. A few quantum dots at around $\nu = 0.265a/\lambda$ also show enhanced decay rates and follow general trend of the simulated waveguide dispersion. Quantum dots emitting at lower frequencies have also been measured and are all found to have low decay rates, less than 0.5 ns^{-1}, until we reach the frequencies for the

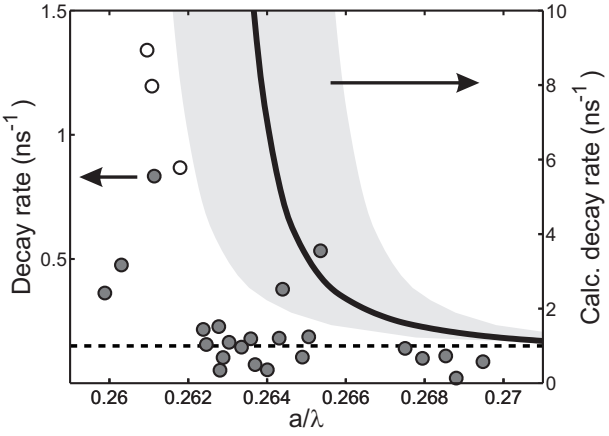

Figure 2.8: Left axis: Measured decay for different quantum dots in a PhC waveguide with lattice constant $a = 256$ nm as a function of normalized frequency. The filled dots have been fitted with a single exponential decay and the empty dots with a double exponential decay. The dashed line at 0.15 ns^{-1} is the mean decay rate of quantum dots not coupled to the waveguide. Right axis: The solid line show the calculated Purcell factor with the gray ares as the uncertainty within $a \pm 2$ nm.

lower band edge of the PhC. This indicates that the large decay rates are related to the Purcell enhancement into the waveguide mode. The fluctuations in the decay rates between the different quantum dots are related to variations in the spatial and polarization overlap between the mode field and the quantum dot dipole moments. The measured quantum dots will thus spread out in an interval below the maximum simulated value. This method therefore provide us with an statistical probe of the broadband variation in the LDOS.

2.2.5 Detailed Mapping of the Waveguide Band Edge

To obtain a more detailed description of the interesting region in the slow light regime we have temperature tuned a set of single quantum dots across the band edge and recorded decay rates as a function of detuning relative to the cut-off wavelength. From these measurements we extract a minimum estimate of the coupling efficiency, or β-factor, for a single quantum dot into the waveguide mode of 85% directly at the band edge [34]. In the following section is provided

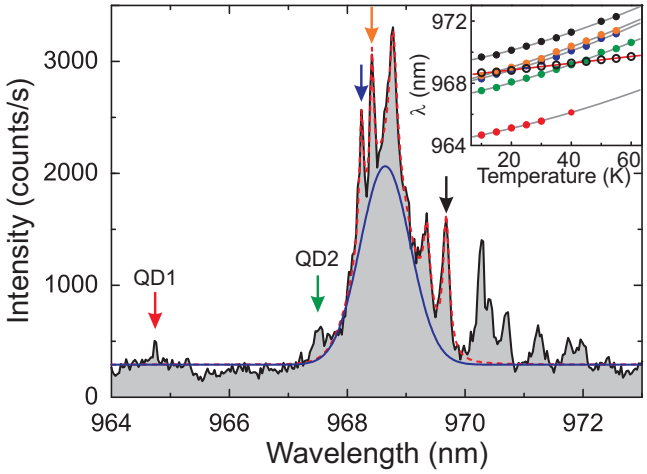

Figure 2.9: Photoluminescence spectrum (black line) of InAs quantum dots embedded in a PhC waveguide measured at 10K with a pump power around saturation. The dashed red line shows a multi-Lorentzian fit of the sharp quantum dot lines and a Gaussian function to fit the broad peak (blue line), which is a signature of the PhC crystal waveguide band edge. Inset: Temperature dependence of the quantum dot emission wavelength of 5 selected quantum dots, marked with arrows in the main panel (filled circles), and of the PhC waveguide band edge (open circles). The lines are second order polynomial fits to the data.

a detailed description of this experiment.

An example of a photoluminescence spectrum recorded at an intensity of 65 W/cm^2, near the saturation power of the exciton lines, is shown in Fig. 2.9. The spectrum was recorded at a temperature of 10 K. Several narrow peaks whose linewidths are limited by the spectral resolution that can be attributed to the emission of single quantum dots and are visible on top of a broader peak. This broad peak is the spectral signature of the band edge of the PhC waveguide. Five of these narrow quantum dot peaks have been selected for further analysis. The peaks are marked by arrows and named QD1–5. The two first quantum dots (QD1–2) have a low intensity of $100 - 200$ c/s on the APD which exemplify the disadvantage of the measurement scheme where we probe from the top. The spectrum has been fitted (red dashed line) with

a Gaussian function for the peak (blue line) and a sum of Lorentzians for the quantum dots in the vicinity of the peak. From this fit we extract the position and the width σ of the broad peak. The spectral position of the broad peak is at $\lambda_m = 968.7$ nm, in very good agreement with the band edge position 968.4nm obtained by a 3D band structure calculation as described in Sec. 2.1.1. A refractive index of 3.44 for GaAs was used. Converting the Gaussian width to a full width at half maximum (FWHM) gives an equivalent Q-factor of $Q = \lambda_m/\Delta\lambda = \lambda_m/2\sqrt{2}\sigma = 800$. Fitting the spectra in the same way but with a Lorentzian for the broad peak results in a narrower linewidth with $Q = 1440$. The presented band edge peak has not been studied under high continues wave (CW) excitation power. However, similar peaks observed in the waveguide saturate at a intensity that is 2–3 time the intensity of the nearby quantum dots. Compared to standard PhC cavities that normally saturate far above the quantum dot background, even for comparable Q-factors [35], this is a quite different behavior. From spectral scans perpendicular to the waveguide it is clear the this feature is localized to the waveguide structure. The same feature has been observed at different position on the waveguide. However, we have not performed any systematic scans along this waveguide to assess whether this feature is common along the whole waveguide or a localized phenomena. So far, we can conclude that the peak is related to the edge of the PhC waveguide. We will further discuss this in connection with the decay rate measurements later in the chapter and in more detail in the rest of the thesis with regards to the formation of Anderson localized modes.

By changing the temperature of the sample, both the quantum dots and the photonic mode shift towards longer wavelengths. Inherent to the different physical mechanics causing the spectral change, the two moves at different rates and this is thus an efficient mechanism to tune the quantum dots relative to the photonic modes. The extracted spectral position for the quantum dots and the band edge mode are shown in the insert of Fig. 2.9. In Fig. 2.10 are plotted low excitation spectra at temperatures in 5 K steps from 10 K to 60 K. The colored lines follow four of the selected quantum lines in Fig. 2.9 across the temperature series. For increasing temperatures we see that the quantum dots both broaden and diminish in intensity due to increased dephasing and the drop in quantum efficiency [36]. We use a maximum temperature of 60 K as a compromise between the maximum tuning range of around ~ 4 nm and the

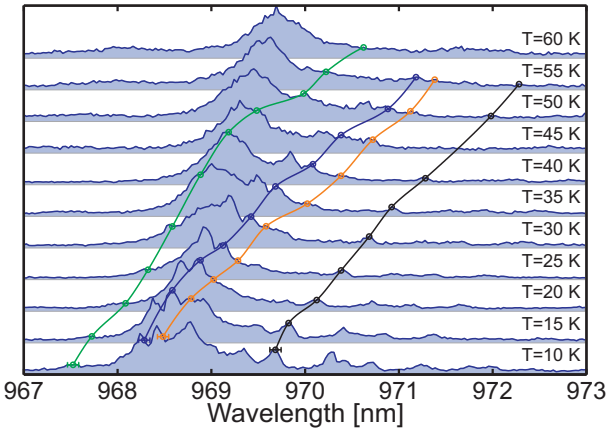

Figure 2.10: Spectra for temperatures between 10 K and 55 K. A broadening and a diminishing of the quantum lines are visible for increasing temperatures. The colored lines show the traces of the quantum dot QD2-5 identified in the different spectra. The error bars in the 10 K spectrum is the spectral resolution.

ability to distinguish the quantum dots from the background. For higher temperatures, non-radiative depopulation of the quantum dots by optical phonons start to contribute [36].

For all the five quantum dots we have performed time correlated photoluminescence experiments. Examples of decay curves for QD3 are shown in Fig. 2.11a as a function of the emission wavelength, recorded at temperatures between 10 K and 60 K. The initial slope of the decay curves changes significantly with temperature and is steepest at 20 K and slowest at 55 K. Two decay curves at 20 K and 60 K are plotted in Fig. 2.11b together with fits to a bi-exponential model convoluted with the APD IRF and the measured dark count (DC) as background leaving a total of 4 fitting parameters,

$$I(t) = \int_0^\infty d\tau \, \mathrm{IRF}(t-\tau) \left(A_{\mathrm{fast}} \mathrm{e}^{-\Gamma_{\mathrm{fast}} t} + A_{\mathrm{slow}} \mathrm{e}^{-\Gamma_{\mathrm{slow}} t} \right) + \mathrm{DC}. \qquad (2.12)$$

In addition, the relative timing offset between the decay curve and the IRF is unknown. When changing the temperature of the sample the sample holder expand, changing this offset. We determine the offset separately for each decay curve. We optimize by minimizing the goodness of fit parameter χ^2 for fits that start at the steep slope before the point of maximum intensity to include the

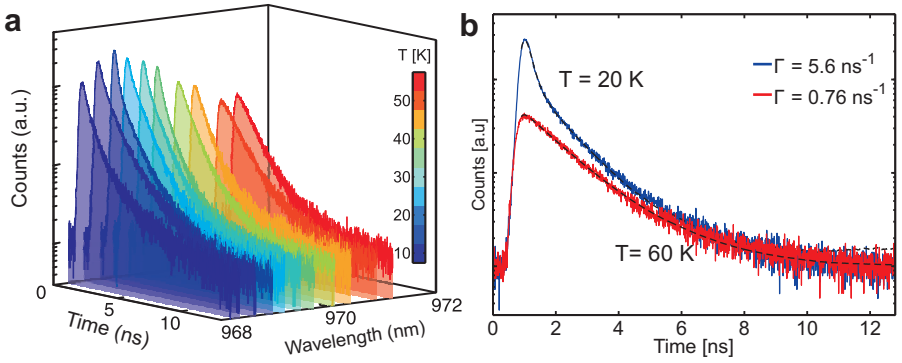

Figure 2.11: (a) Decay curves of a single quantum dot (QD3) measured with 5 K steps in a temperature range between 10 K and 60 K and plotted as a function of the emission wavelength. (b) Double exponential decay fits convoluted with the IRF for the decay curves at 20 and at 60 K.

timing of the excitation pulse in the fit. In this way small relative offsets result in large changes in χ^2. The offset has been corrected in Fig. 2.11b. In the shown fits the fitting interval start 200 ps before the maximum intensity, which allows us to capture the fastest components of the decay curves. This is especially important for decay rates close to that of the IRF, which is the case for the decay curve at 20 K. In this regime the extracted parameters become more sensitive to the exact fitting conditions so the real uncertainty is difficult to assess but much larger than the 0.02 ns^{-1} extracted from the fitting procedure. If we fit the decay curve at 20 K without the IRF we obtain a fast decay rate of $\sim$ 4.5 ns^{-1}, around 1 ns^{-1} slower than with the IRF. The decay rate for the decay curve at 60 K gives identical values of around 0.76 ns^{-1} whether we include the convolution with the IRF or not. This curve can effectively be fitted by a single-exponential with a free background, since the slow and fast components are very similar.

The fastest of the two exponents corresponds to the total measured decay rate: $\Gamma_{\text{tot}} = \Gamma_{\text{wg}} + \Gamma_{\text{rad}} + \Gamma_{\text{non-rad}}$ that contains the radiative decay rate into the waveguide mode Γ_{wg}, out-of-plane radiation Γ_{rad}, and the non-radiative decay rate $\Gamma_{\text{non-rad}}$. The slow exponent contains contributions from fine structure effects including the non-radiative decay from dark states and the spin-flip time between dark and bright states [37]. Furthermore, the slow component

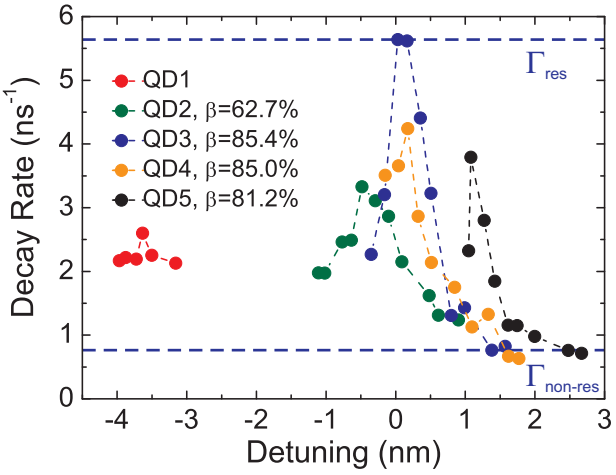

Figure 2.12: Decay rates of the five quantum dots marked with arrows in the spectrum in Fig. 1 plotted as a function of the emission wavelength. The extracted β-factors for four quantum dots are shown in the legend. The two dashed lines labeled with Γ_{res} and $\Gamma_{\text{non-res}}$ mark the fastest decay rate on resonance with the PhC waveguide band edge and the slowest decay rate when the quantum dot emission lies in the PhC band gap for quantum dot 3 (QD3), respectively.

contains minor contributions from other quantum dots whose emission lines overlap with the quantum dot under study within the spectral resolution of the setup. This last contribution is the main source of the variations in the slow component. Since we are interested in the radiative coupling to the waveguide mode, in the following, we only focus on the fast component.

All the extracted decay rates for the 5 quantum dots are plotted in Fig. 2.12 as a function of detuning $\Delta\lambda = \lambda_{\text{QD}} - \lambda_{\text{mode}}$, where λ_{mode} is extracted from the gaussian fit above. Quantum dot 1 (QD1) is approximately detuned -4 nm away from the band edge peak and shows a constant decay rate of $> 2\ \text{ns}^{-1}$ over a the full tuning range of ~ 1.5 nm. The flat dispersion is consistent with the quantum dot being coupled to the PhC waveguide mode. The rest of the quantum dots QD2–5 are all located near the band edge peak, at zero detuning, and follow the same trend with a peak in the decay rates followed by a monotonically decrease down to around $0.7\ \text{ns}^{-1}$ for positive detunings. The

maximum rates for these quantum dots are all higher than that of QD1, due to a stronger coupling to the waveguide mode near the band edge, which indicates that we have an enhanced coupling over the 4 nm range from QD1 to the peak. However, the shape of the decay rate variation is not consistent across the quantum dots. For instance the maximum for QD2 is shifted -0.5 nm relative to the zero detuning and QD5 shows a sharp drop at 1 nm. The cause of these inconsistencies is unclear but we attribute some of it to the uncertainty in the fitting and to the difficulty in following the individual quantum dots throughout the temperature series. The fact that we see a consistent decrease in the decay rate for all the quantum dots at the long wavelength edge of the band edge strongly indicate that we capture the correct shape of the band edge tail. For higher temperatures we expect the decay rates to increase whereas we observe the opposite effect and the variation is therefore caused by changes in the radiative rates. Interestingly enough, they all level off at approximately the same value indicating that they are limited by the non-radiative decay rate at 60 K rather then the radiative rate in the band gap.

We will now focus on QD3 since it exhibits the largest decay rate and thus the strongest coupling to the waveguide mode. Starting from negative detuning and moving towards zero, the measured decay rate increases reaching a maximum value of $\Gamma_{\text{res}} = 5.6\,\text{ns}^{-1}$ on resonance. This corresponds to a Purcell factor $F_p = \Gamma_{\text{res}}/\Gamma_{\text{hom}}$ of 5.2, where $\Gamma_{\text{hom}} = 1.1\,\text{ns}^{-1}$ is the decay rate measured for quantum dots in a homogenous medium. This Purcell factor is 4 times larger than observed in Sec. 2.2.4. For positive detunings away from resonance the measured decay rates decrease monotonically reaching a minimum value of $\Gamma_{\text{non-res}} = 0.76\,\text{ns}^{-1}$. From these data we can extract the coupling efficiency of the emission from a single quantum dot into the waveguide mode, described by the β-factor:

$$\beta = \frac{\Gamma_{\text{wg}}}{\Gamma_{\text{tot}}} \approx \frac{\Gamma_{\text{res}} - \Gamma_{\text{non-res}}}{\Gamma_{\text{res}}}. \tag{2.13}$$

where Γ_{wg} is the decay rate into the waveguide mode only. We are interested in a best estimate on resonance, for both the evaluation of Γ_{wg} and Γ_{tot}. The decay rate Γ_{wg} on resonance can be evaluated as $\Gamma_{\text{res}} - \Gamma_{\text{non-res}}$ when we assume that $\Gamma_{\text{rad}} + \Gamma_{\text{non-rad}}$ is constant in the considered wavelength range. Due to the small tuning range this is considered a good approximation. For a single quantum dot the variations in $\Gamma_{\text{non-rad}}$ is mainly caused by the evaluated tem-

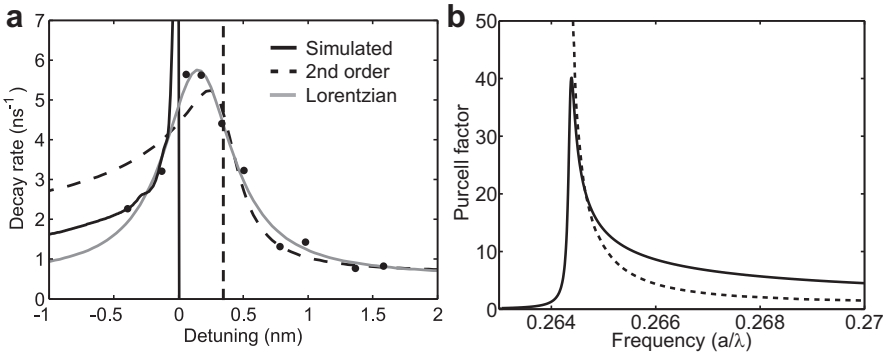

Figure 2.13: Decay rates of QD3 extracted from the data shown in panel (a) as a function of detuning relative to the waveguide band edge. The lines represent different fits to the decay rates. All the fitting models have a free amplitude since several uncontrolled variables determined the amplitude of the signal – e.g. the spatial mismatch between the quantum dot position and the polarization relative to the waveguide electric field and a free background. The solid black line represents the simulated decay rate for a lossless PhC waveguide. The dashed line is a second order expansion around the band edge which includes a finite loss. The solid gray line is a lorentzian fit.

peratures that increases $\Gamma_{\text{non-rad}}$ and therefore reduces the estimated β-factor. The change in Γ_{rad} is expected to be small due to the small tuning range. The fact that the optical environment changes radically, crossing the band edge, might lead to non-trivial changes in the coupling to leaky radiation modes. With the above measurements we retrieve $\beta = 85\%$. Tuning the quantum dot further away from the band edge would move it deeper into the band gap, which would reduce $\Gamma_{\text{non-res}}$. In section Sec. 2.2.4 we reported variations in $\Gamma_{\text{non-res}}$ between $0.05 - 0.43$ ns^{-1} and in defect free PhCs we have observed inhibitions factors (inverse of the Purcell factor) of up to 30. This would result in β-factors between $92\% - 99\%$. A larger tuning range could be obtained by implementing alternative tuning schemes like electrical tuning [38] or gas tuning [39], both schemes are in the pipeline of further experiments.

2.2.6 The Density of States at the Band Edge

From the measured decay rates we can map out the spectral dependence of the LDOS and compare to various models for the expected LDOS near the band edge. In Fig. 2.13a the decay rate for QD3, again, has been plotted, combined with 3 different models for the density of states: The solid black line represents the ideal LDOS for a lossless PhC

$$F_{p,\max} = \frac{3\pi c^3 a}{n^3 \omega^2 v_g V_{\text{eff}}} \tag{2.14}$$

To fit the 3 first data points we have added $\Gamma_{\text{non-res}}$ to account for coupling to radiation modes and scaled the ideal Purcell factor by 0.04. This accounts for the spatial and polarization mismatch between the quantum dot dipole moment and the local electric field. It is clear that the data does not exhibit a divergence and this curve only reproduces the first initial data points and not the following reduction in the decay rate.

In real structures, where the losses are dominated by material absorbtion, weak back scattering or out-of-plane scattering, the LDOS broadens near the band edge. Lossy states are created inside the band gap that limit the maximum achievable group velocity and thus resolve the divergence. To model this behavior we use a variant of the procedure in Ref. [40]. The losses in the slow light regime is a complicated combination of out-of-plane losses that scale with $1/v_g$ and back scattering losses that scale with $1/v_g^2$ and is thus strongly dispersive [41]. Here we assume that losses can be described by a single constant parameter that is included as an imaginary part of the dielectric constant $\varepsilon = \varepsilon' + i\varepsilon''$. We first Taylor expand the band structure to second order around the $K = (a/\pi, 0, 0)$ point at the band edge

$$\omega(k) = \omega_0 + \alpha(k - K)^2 \tag{2.15}$$

where α is the curvature of the band and ω_0 is the band edge frequency. The dispersion at the band edge is flat and the first order term drops out. We have extracted α by fitting the band structure with a second order polynomial and succeedingly increased the number of k_x-values included in the fit until the χ^2-value start to decrease. Using first order perturbation theory in ε'' we acquire a small imaginary shift in $\omega_0 = \omega_0 + \Delta\omega = \omega_0 - \frac{1}{2} i f \omega_0 \varepsilon''/\varepsilon'$ in the band edge frequency where f is the fraction of the electric energy in the absorbing media.

Since the waveguide mode is confined inside the waveguide we let $f \approx 1$. Just proceeding by calculating the group velocity, $\partial\omega/\partial k$, from Eq. (2.15) leads to unphysical results as the physical frequency ω can not be complex, so we invert Eq. (2.15) and obtain a complex expression for $k(\omega)$

$$k(\omega) = K + \sqrt{\frac{\omega - \omega_0(1 - \frac{1}{2}if\omega\varepsilon''/\varepsilon')}{\alpha}} \tag{2.16}$$

Inserting this in the expression of the group velocity with a complex k, $v_g = \mathrm{Re}[\frac{\partial\omega}{\partial k}] = \left(\mathrm{Re}[\frac{\partial\omega}{\partial k}]\right)^{-1}$ we obtain an approximate expression for the group velocity

$$v_g \approx \frac{2\beta\sqrt{\alpha}}{\sqrt{\beta + 2(\omega - \omega_0)}}, \qquad \beta^2 = 4(\omega - \omega)^2 + (\omega f\varepsilon''/\varepsilon')^2. \tag{2.17}$$

that is valid near the band edge and takes a small amount of loss into account. For $\omega = \omega_0$ we obtain a minimum group velocity of

$$v_g = 2\sqrt{\alpha f\omega_0 \frac{\varepsilon''}{\varepsilon'}} \tag{2.18}$$

and even for frequencies below the band edge $\omega < \omega_0$, do we obtain finite values. By inserting Eq. (2.17) in the expression for the Purcell factor Eq. (2.14) we get an approximate expression for the Purcell factor. The dashed line in Fig. 2.13a is a fit to the Purcell factor with loss where the fitted parameters are $\tilde{\varepsilon}'' = 0.0049$, an amplitude $\tilde{A} = 0.10$, the background ($\tilde{\Gamma}_{\text{non-res}} = 0.63\ \text{ns}^{-1}$) and a frequency offset for the band edge indicated by the dashed vertical line in the figure. The fitted ε'' corresponds to a loss length

$$l = \left(\frac{2\pi}{\lambda}\sqrt{\frac{\sqrt{\varepsilon'^2 + \varepsilon''^2} - \varepsilon'}{2}}\right)^{-1} \tag{2.19}$$

of $l = 214\ \mu\text{m}$. Fitting QD2–5 gives similar values for ε''. For positive detunings the fit correctly follows the decrease down to the measured $\Gamma_{\text{non-res}}$. However, for negative detunings where the approximate solution is expected to converge to the simulated values it crosses the simulated line within less than 0.1 nm from the band gap, and gives consistently higher valuer for larger negative detunings. This is also seen in the broader bandwidth in Fig. 2.13 for $\varepsilon'' = 0.0049$ and unit amplitude. Even in the limit of vanishing loss the 2nd order expansion deviate

from the simulated values within -1 nm from the band edge. One limitation of the model is the neglected dispersion in the losses. From the Purcell factor obtained in the loss free simulation we see a strong dispersion in the slope within the first 0.5 nm from the band edge. This questions the validity of the model even for positive detunings where we have no exact simulation to verify against. However, exactly at the band edge the model is correct, and using the highest measured Purcell factor of 5.2 and solving for ε'' we get a lower limit for the loss length of $l = 71$ μm, which is shorter than the sample length.

The last curve (gray line) is a Lorentzian fit to the data points and among the three models is the one that gives the best fit. The Lorentzian line shape represent a localized mode and from the fit we can extract a Q-factor of 1480. This is almost identical to the Lorentzian fit of the spectra, which gave $Q = 1440$. Although the Q-factor can not be accurately be obtained at low pumping power, this support the idea that we are actually observing the coupling to localized mode whose LDOS shape closely follow the spectral shape of the mode. As will be discussed in more detail in the following chapter, so-called Anderson localized modes indeed form near the band edge of the waveguide. The low intensity band edge peaks at high power suggest that this not the case. However, from the presented data we can not positively conclude whether we are observing the coupling to a lossy propagating slow light mode or to a localized mode.

2.3 Conclusion

In this chapter it has been shown that the spontaneous emission from single quantum dots can be efficiently coupled to a PhC waveguide in the slow light regime. The measured decay rates of single quantum dots closely follow the broadband behavior of the waveguide density of states and an enhancement of 7 has been observed between the fastest quantum dot coupled to the waveguide compared to the average of uncoupled quantum dots. This proves that we can couple the emission from single quantum dots to the propagating mode of a PhC waveguide. At low pumping powers a spectral peak near the band edge has been observed. By temperature tuning a set of quantum dots near the band edge the variations in the density of state has been mapped out and a β-factor of 85% has been extracted for single quantum dot into the waveguide mode.

Finally, the shape of the band edge density of states has been compared to three models. A lossy propagating mode or a localized mode both are possible candidates for the mode we have observed in our experiments and we have so far been unable to distinguish between the two scenarios.

Chapter 3

Single Photon Emission in the 1D Anderson Localized Regime

3.1 Introduction

In the previous chapter the coupling of a single quantum dot to a propagating mode of a PhC waveguide was studied. The slow-down of the group velocity near the band edge of the waveguide led to an enhanced coupling strength caused by the Purcell effect. Losses were treated as a perturbation resulting from out-of-plane scattering or a mean back scattering probability resulting in a loss rate proportional to n_g^2. This treatment neglects multiple backward and forward in-plane scattering and any interference effects between scattered light waves in the waveguide. Historically, PhC waveguides were thought as useful tools to propagate light on chips over long distances. However, the in-plane multiple scattering has a very pronounced effect on the propagation of light in 1D waveguides, especially in the slow light regime. If the mean free path between scattering events is shorter than the length of the waveguide, multiple forward and backward scattering on the same disorder site occurs, which forms closed loops of light propagation that effectively localizes the light. Instead of just causing increased losses, imperfections now transform the propagation

into a different regime, where light is no longer propagating but is trapped in randomly confined modes. These localized modes are examples of Anderson localized modes of light in a one 1D disordered system.

It was proposed by John [42] that a small amount disorder in a PhCs would be efficient to localize light near the band edges. Any random disruption of the lattice structure creates bound states inside the otherwise forbidden band gap. The low group velocities near the band edge increases the interaction time with the disorder and thus increases the probability of multiple scattering. As the group velocity converges towards zero near the band edge it is expected that PhC waveguides are efficient at localizing light into small random cavities. The fact that these Anderson cavities are spontaneously created from the scattering on the distributed disorder makes their existence inherently robust towards imperfections. This makes them promising alternatives to traditional PhC cavities for cavity QED, where highly engineered point defects create bound states in the band gap. Here unavoidable imperfections from the fabrication is detrimental to obtain ultra high Q-factor needed for cavity QED. Recently Anderson-localization has been observed in spectral regions near the band edge of PhC waveguides [43, 44], achieving quality factors of light confinement as high as 600.000 [45] and has been used to enhance the light-matter interaction [46] in the weak coupling regime. The last results will be further discussed in Chapter 4.

These studies are mainly focused on characterizing the effect of single realizations of disorder, which can show interesting effects, but does not probe the full phase space of the imperfections. Therefore, configuration averaging over many realization of the same type and strength of disorder is needed to characterize the light propagation. The length scale over which the light is localized, on average, is determined by the localized length ξ, which is given by an exponential decay length away from a light source and is defined through

$$\langle \ln[I(z)] \rangle = -z/2\xi \tag{3.1}$$

where $I(z)$ is the light intensity along the propagation direction and $\langle . \rangle$ denotes the configuration averaging. Due to the limited phase space of 1D systems, consisting of only forward and backward propagating modes, light always localizes in infinitely long 1D samples. In this case part of the backward reflected light will eventually return to the light source with unit probability. For finite size samples, the transition to the localized regime occurs for $\xi < L$. For $L > \xi$,

the light, on average, escapes the sample before being scattered twice and the system is in the ballistic regime. The localization length is in general dependent on the details of the type and strength of the disorder and can only be obtained for a given system by solving Maxwell equations and ensemble averaging the intensity distribution from a point source. One of the large breakthroughs in the study of propagation in disordered media is the introduction of the scaling theory of localization. It states that for uniformly disordered systems with time reversal symmetry and no losses the ensemble average light propagation is fully determined by the universal conductance/tranmission g of the system. Here g is only a function of ξ/L [47, 12]. Therefore, the Q-factor distributions of Anderson localized modes are fully determined by this ratio and any equivalent system with the same ξ/L as the PhC waveguides would show the same distributions. The out-of-plane scattering, leakage to modes above the light line and intrinsic material losses in the PhC waveguides give rise to losses that reduces the Q-factors arising from the purely 1D scattering. It has been shown that a universal loss parameter ξ/l, where l is the loss length, is sufficient to uniquely describe the light propagation and thus the Q-factor distributions [48]. In disordered periodic structures yet another universal parameter is needed to describe the states inside the former band gap [49], which we disregards here.

In this chapter we present a theoretical study of the light-matter interaction between a single quantum emitter and a photon confined in an Anderson-localized mode in disordered PhC waveguides. Using a 1D model to extract the distributions of the Q-factors and the light-emitter coupling strength for the localized modes, we analyze the probability of achieving the strong coupling regime for realistic values of the localization length and out of plane loss.

3.2 Modes of Disordered Photonic Crystal Waveguides

To study the localized modes in more detail we have performed full coherent 2D finite difference time domain (FDTD) simulations of disordered PhC waveguides. From these simulations we can obtain the intensity profiles and spectral position of the modes for individual realizations of disorder. All the results presented here originate from a single realization, although similar results have been obtained from different realizations.

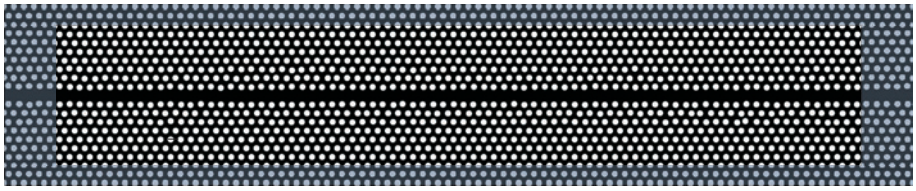

Figure 3.1: Image of the disordered PhC waveguide used in the FDTD simulations. Black is the high index material (see Sec. 3.2 for parameters). The blue area mark the PML layer.

The simulated structure is similar to the PhC waveguides in Chapter 2 and is shown in Fig. 3.1. It consist of air holes in 2D PhC arranged in a hexagonal lattice with lattice constant a and hole radius $0.29a$, where one row has been removed in the center to form the waveguide. The total length of the simulation domain is $81a$ with 8 row of holes on each side of the waveguide. The holes in three rows on both side of the waveguide have been randomly displaced according to a gaussian random number generator with a standard deviation of $0.03a$. We only disturb a few rows on both side of the waveguide to encapsulate the quasi-1D waveguide in a full band gap of a pure PhC. The refractive index of the structure is $n = 2.76$ which corresponds to the effective refractive index for the propagating mode in a PhC membrane waveguide with a membrane thickness of 150 nm [50]. This value was found by manually matching the band edge frequency of the waveguide in the 2D simulation with the $\nu = 0.2658a/\lambda$ for the membrane. This assumes that the transverse mode profile for the localized modes are similar to the propagating modes of the waveguide. Perfecting matching layers (PML) acting as absorbing boundary conditions covers 5 lattice constants at either end of the waveguide and ensures that light propagating to the ends of the domain is absorbed. This mimics a finite size waveguide where light that reaches the ends is lost. In Fig. 3.1 the size of the PML layer is shown as the blue overlay. The non-uniform structure of the PhC reduces the effect of the PML and numerical reflections from the ends appear even for thick layers covering 10-20 lattice constants. As we are interested in localized modes the effect on the results are limited and the chosen size of 5 is a compromise between calculation time and reflectivity.

3.2.1 Finite Difference Time Domain simulations

The simulations have been performed with the comprehensive MEEP FDTD package [51], which allows to easily construct and simulate complex structures. The FDTD method directly solves for the time evolution of the Maxwell equations for arbitrary current sources by time stepping the electric displacement field $\boldsymbol{D}(\boldsymbol{r},t)$ and magnetic field $\boldsymbol{B}(\boldsymbol{r},t)$ in an equidistantly grid over the structure, where $\boldsymbol{D}(\boldsymbol{r},t) = \varepsilon(\boldsymbol{r})\boldsymbol{E}(\boldsymbol{r},t)$ and $\varepsilon(\boldsymbol{r})$ is the frequency independent dielectric constant. The fixed grid size used in FDTD directly determines the resolution of the smallest structures. MEEP implements a sub-pixel averaging procedure that improves the accuracy of the solution for features smaller than the grid size [52]. This is essential for simulating small disorder variations in the dielectric constant. For these simulations a spatial grid size of $\Delta x = \Delta y = a/20$ and a time discretization of $\Delta t = 40a/c$ were used, where c is the speed of light. Internally, normalized unit is used where $c = 1$ and all length scales are in units of a.

The FDTD method is a well-established method for calculating the localized quasi-modes of cavities. The structure is excited by a short electric dipole pulse $p(t)$, whose Fourier transform $\boldsymbol{p}(\omega) = \boldsymbol{p}_0 \exp[-(\omega-\omega_0)^2/\Delta\omega]$ covers the relevant spectral region. The solution satisfies:

$$\left[\nabla \times \frac{1}{\mu}\nabla \times -\frac{\omega^2}{c^2}\varepsilon(\boldsymbol{r})\right]\boldsymbol{E}(\boldsymbol{r},\omega) = \frac{\omega^2}{c^2}\boldsymbol{p}(\omega)\delta(\boldsymbol{r}-\boldsymbol{r}_s), \tag{3.2}$$

where $\varepsilon(\boldsymbol{r})$ and μ is the permittivity and permeability respectively. The different frequency components of the source excite all the modes of the structure within the spectral range. In the time domain, after the source has died the remaining field constitutes a super position of the naturally oscillating but decaying modes of the structure, which takes the form of a sum of oscillating quasi-modes

$$\boldsymbol{E}(\boldsymbol{r},t) = \sum_i \boldsymbol{E}_{i0}(\boldsymbol{r})\mathrm{e}^{-i(\omega_i t-\phi_i)-\kappa_i t} \tag{3.3}$$

where E_{i0} is the quasi-mode field amplitude, ω_i is the resonance frequency, ϕ_i is the phase and $\kappa_i = \omega/2Q_i$ is the mode decay rate and Q-factor. The intensity spectrum $I(\omega) = |\mathcal{FFT}(\boldsymbol{E}(\boldsymbol{r},t))|^2$ of Eq. (3.3) is a set of lorentzians peaks whose FWHM linewidth is $\kappa/2$. Due to the finite simulation time T, the spectral resolution is limited by $1/T$. For large Q-factors the decay time is much longer than the practical simulation time resulting in aliasing effects

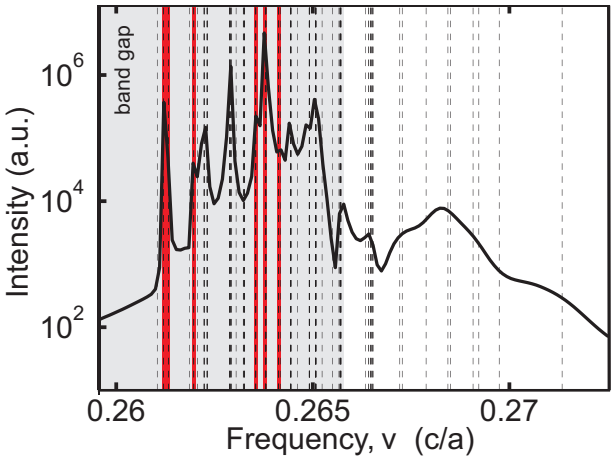

Figure 3.2: Broadband intensity spectrum summed over 9 different equally distributed position along a disordered PhC waveguide showing the different localized modes near the band edge. The gray area are frequencies below the band edge of the ordered waveguide. The dashed black lines represent all the identified resonances from the 9 positions. Modes covering several detection position are represented by multiple nearby lines. Red lines are a subset of the all the modes that have been positively identified from narrow band excitation.

from the high frequency components at the cut-off time. A method, denoted harmonic inversion (also included in the MEEP package) has been used to circumvent these limitations [53]. In contrast to a general Fourier transform, in this method $\boldsymbol{E}(\boldsymbol{r}, t)$ is assumed to have the form Eq. (3.3) and the parameters are directly extracted for the highest amplitude peaks which allow to resolve closely spaced resonances and extract their Q-factors with high accuracy.

To excite all the modes of the disordered waveguide we excite with 9 y-polarized point sources distributed along the whole waveguide. The positions of the sources have been randomly perturbed from the center of the waveguide to not selectively excite nearly symmetric modes. The intensity spectrum from a broadband source $\Delta\nu = 0.02a/\lambda$ is plotted in In Fig. 3.2, covering the region near the band edge of the waveguide. The spectra from the same 9 positions are summed to extract all the modes. The simulation time covers 2000 optical periods after the source pulses have died and the fields at none of the 9 points

have fully decayed at this time. Several sharp resonances are visible in the band gap of the PhC indicating that localized states are indeed formed. Broader features at higher frequencies in the spectral region of the waveguide mode are observed, which represent low Q-modes. The dashed lines are the extracted resonances from the harmonic inversion algorithm, combining all the resonances for the 9 positions. Therefore one resonance can be represented by several lines if the given mode extends over several detection points. If the modes have low amplitudes at the detection points the resonance extraction is less accurate resulting in a spread of the lines. However, from a more detailed study of individual modes discussed later, it is clear that many of the lines represent distinct and strongly confined modes and the spectrum below the band gap is densely packed with modes.

The mode profiles of the individual modes can be obtained after exciting with a narrow band source around each individual mode. A total of 18 narrow band simulations have been carried out with excitation bandwidths between $\Delta\nu = 0.00012 - 0.00074a/\lambda$ according to the distance to nearby lines, with a 20 to 50 hour computation time on 8 CPU for each mode. Decreasing the bandwidth decreases the likelihood of exciting the nearby modes but increases the execution time. Only 5 modes have been positively identified as single modes and they are shown as red lines in Fig. 3.2. The corresponding intensity profiles are shown in Fig. 3.3 ordered with increasing frequency. The rest of the narrow band simulations either showed up as superpositions of multiple modes or propagating Fabry-Pérot like modes within the waveguide with the dominant reflections from either the PML layer or defects far apart. It would be interesting to study the latter modes in more detail as they cover extended modes whose mode profile is not fully converged yet within the simulation time. The extracted modes are therefore most likely biased towards small high-Q modes.

The extracted Q-factors are in the range of 50.000 to 500.000. Since we are performing 2D simulation they only account for the in-plane losses. This explains the clear correlation seen in the figure between mode extend and Q-factor. For 3D membrane waveguides the coupling to states above the light line will on average result in enhanced out-of-plane losses for strongly confined modes and the observed correlation will be less pronounced. The low Q-factor of the modes above the band gap region are therefore a signature of more extended

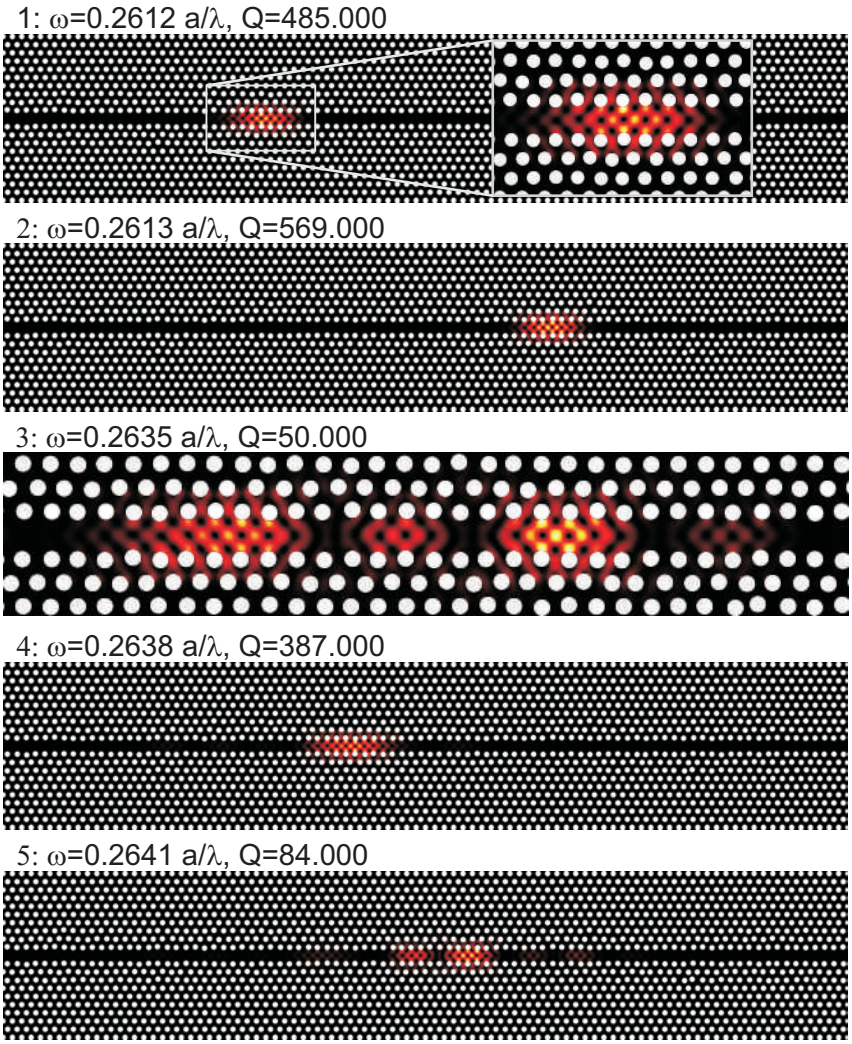

Figure 3.3: Electromagnetic intensity (black-yellow) for 5 different random modes in a disordered PhC waveguide with 3% disorder in the hole positions for the three rows on both side of the waveguide. The black region show the high refractive index region of the structure. See Sec. 3.2 for parameter details. Mode 1,2,4,5 show the hole simulation domain while mode 3 shows a zoom in around the mode.

modes rather than of the their actual Q-factors. However, the intensity profiles should resemble their 3D counterparts. All 5 modes is plotted in Fig. 3.3 approximately maintain the Bloch periodicity related to the underlying lattice but with a modulated envelope. They are mostly mirror symmetric around the waveguide plane and are strongly confined to the waveguide structure, only extending 1-2 rows into the PhC even though 3 rows have been disrupted. This resembles the lateral mode profile of the ideal waveguide mode. We can intrepid it in this way that the disorder easily creates states in the band gap for $\boldsymbol{k}$-vectors along the waveguide and for frequencies below band edge and that the waveguide already supply the physical space needed for the modes to occupy. For $\boldsymbol{k}$-vectors perpendicular to the waveguide the light sees the PhC band gap and propagation is inhibited. Disorder induced states will be created near the band edge of the 2D band gap, which is far away in frequency. Only if the disorder is very pronounced, disrupting the band structure deep into the band gap, are the modes allowed to expand perpendicular to the waveguide. The band gap has been show to be very robust towards disorder maintaining 90% of its bandwidth for 30% disorder, 10 times higher than used here [54]. Along the direction parallel to the waveguide the modes can be characterized into modes with only one or with several speckles. The smallest modes (1,2,4) cover only a few lattice sites (see the zoom in for mode 1) and are very similar to mode profiles for engineered cavities optimized for high-Q and low mode volume for QED experiments [3]. The two larger modes (3,5) extend over several speckles with different intensity, each covering a number of Bloch periods. It is not clear from these few samples how representative these examples are and more statistics is needed to obtain quantitative results. However, it is evident that even a small amount of disorder in PhC waveguides are enough to strongly localize light to within a few lattice constants resulting in very low mode volumes.

3.2.2 Towards Ensemble Averaged Simulations

One of the tasks in the direct line of the current simulations is to extract the localization length, study its dependence on the amount and type of disorder and, study any dispersive trends in mode profile and localization length. To answer these questions, a configuration average over different sample needs to be performed. For each sample, simulations to extract mode profiles are needed

as discussed above. The close spectral packing and large variation in Q-factors make this a tedious task that is hard to automate using the employed FDTD method. To extract the real Q-factors full 3D simulations are needed, which is beyond the scope of this method due to the large difference in length scale between the features sizes of the structure and the scattering sites. Disorder breaks the symmetry/periodicity which prevent the use of Bloch's theorem to reduce the domain. The simulated structures therefore need to span the full size of the sample or at least be larger then the mean scattering length. For the used FDTD method the computation times scales at least as N^d where N is the number of grid in one dimension and, d is the dimension. For large samples this scaling makes it unfeasible to perform ensemble averages.

Several alternative methods have been used to circumvent this problem. As already mentioned in Chapter 2 treating disorder as a perturbation using a Green's function approach has been successfully employed to calculate the back scattering and out-of-plane losses in PhC waveguide in the weak scattering regime [41]. Here the configuration average is performed prior to the electromagnetic calculation and the PhC is on average considered to be periodic, which disregards any interference effects. The method therefore only gives correct results in the ballistic regime for low group velocities. This theory predicts a back scattering loss that scales with n_g^2 and a radiation loss that scales with n_g. For moderate group indices n_g the back scattering loss dominates and for high $n_g > 30 - 100$ the theory breaks down [55]. Recently, different methods have been devised to simulate the electromagnetic properties of 3D disorder PhC waveguides [56, 57, 58] including coherent multiple scattering events. Both simulations and recent experiments show that multiple scattering dominates above a given threshold in group index, resulting in the formation of narrow spectral resonances for single disorder realizations. In near field measurements the mode profile is seen to be strongly disrupted in this regime [55]. Similar mode profiles to the ones seen in Fig. 3.3 are observed in simulation for PhC waveguides longer then 1000 lattice constants and with $0.002a$ disorder using a Bloch mode expansion method [58]. So far only Ref. [57] have presented an extensive analysis for ensemble averaged values using a Bloch scattering matrix method. Here the localization length is predicted to approach a single lattice constant at the band edge and the onset of localization, defined as $\xi \leq L$, is seen to occur for successively lower n_g as the amount of disorder is

increased. These predictions are verified in Ref. [58] where localization length at the length scale of the lattice constant is obtained inside the band gap. Experimentally localization length down to 27 μm have been measured in PhC waveguides obtained from the ensemble average transmission [44].

In this section we have shown that a small amount of disorder in a PhC waveguide can create localized modes at frequencies near the band edge. It is thus possible to control the spectral location of the modes through band engineering of the PhC waveguide. The simulated mode profiles are strongly confined, some to only a few lattice constants. With the employed FDTD method it is not feasible to perform the ensemble averages needed to calculate the localization length and the statistical properties of the modes. Instead, we utilize the quasi-1D nature of the PhC modes and universality of the ratio ξ/L and ξ/l to study the distribution of Q-factors and the emitter coupling strengths in a equivalent 1D model. To actually calculate ξ for a disordered PhC waveguide full 3D simulations are needed, but all statistical observables for the same ratios of ξ/L and ξ/l are identical.

3.3 Anderson Localization in a 1D Optical Model for a Disorder Waveguide

In order to obtain statistics for the Anderson localized modes and to assess the coupling strength to emitters we employ a 1D model. A detailed description of this model and the optical properties including transmission statistics and intensity distributions are reported in Ref. [59]. The disordered model consists of a stack of thin layers with a thickness of $L_p = 10$ nm of varying refractive index taken from a uniform distribution with a mean of $\langle n \rangle = 3.5$ and width Δn and a total sample length of $L = 100$ μm. The sample is embedded in a surrounding material with refractive index 3.5 and hence represent an open system, displaying finite Q-factors. The thickness of the layers is much smaller than the wavelength of light to be in the weak scattering limit. This model is an implementation of the well studied random matrix theory [60]. The detail of the disorder is not important but the layer thickness and Δn uniquely determines the universal ratio ξ/L. Compared to the PhC waveguide that we are describing this model does not take the super imposed periodicity from the PhC into account, which would leads to the strong dispersion near the band

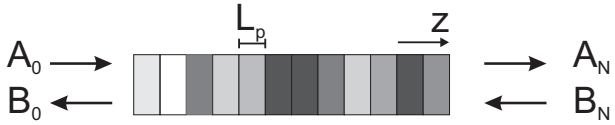

Figure 3.4: (a) Sketch of 1D disordered waveguide composed of a stack of layers with thickness L_p and with different refracting indices (gray colors). The As and Bs denote the amplitudes of the forward and backward propagating fields. From Ref. [59].

edge. A more realistic model would be to add small amount of disorder to a periodic structure with the same periodicity as the PhC.

A sketch of the structure is plotted in Fig. 3.4 where each layer is number from 0 to $N-1$. The field propagation in such a 1D layered structure consists of successive reflections from each interface and the final field arises from the total interference effect from all the layers. The propagating field is given by forward a backward propagating modes. Assuming only one polarization direction perpendicular to the waveguide we have a scalar field of the form

$$E(z) = A(z)\mathrm{e}^{i\,\beta(z)z} + B(z)\mathrm{e}^{-i\,\beta(z)z}, \tag{3.4}$$

where $\beta(z) = k_0\, n(z)$ is the propagation constant with $k_0 = 2\pi/\lambda$ as the wave number and $n(z)$ is the position depended refractive index. The propagation in the layered medium can be calculated analytically by using the transfer matrix theory [50]. Here the amplitudes $\boldsymbol{E}(z) = [A(z), B(z)]^T$ are transferred through M layers from point z_0 to z by a matrix $\boldsymbol{M}(z, z_0)$, $\boldsymbol{E}(z) = \boldsymbol{M}(z, z_0)\boldsymbol{E}(z_0)$, where $\boldsymbol{E}(z)^T$ denotes the transposed vector of $\boldsymbol{E}(z)$. $\boldsymbol{M}(z, z_0)$ consists of a product of matrices where each matrix either describes the free propagation of distance d_j inside a single layer with refractive index n_j, $\boldsymbol{M}_p(d_j, n_j)$, or the reflection and transmission at the interface between two layers $\boldsymbol{M}_I(n_j, n_{j+1})$ with,

$$\boldsymbol{M}_p(d_j, n_j) = \begin{bmatrix} e^{-i\,k_0 n_j\, d_j} & 0 \\ 0 & e^{i\,k_0 n_j\, d_j} \end{bmatrix}, \quad \boldsymbol{M}_I(n_j, n_{j+1}) = \frac{1}{t}\begin{bmatrix} 1 & r \\ r & 1 \end{bmatrix}, \tag{3.5}$$

and

$$t = \frac{2\,n_j}{n_{j+1} + n_j}, \quad r = \frac{n_j - n_{j+1}}{n_{j+1} + n_j}. \tag{3.6}$$

Assuming that we know the field at z_j in the center of layer j and want to propagate it to the end of the sample where the surrounding medium has the refractive index n_N the propagation matrix becomes

$$\boldsymbol{M}(z_N, z_j) = \boldsymbol{M}_I(n_{N-1}, n_N)\boldsymbol{M}_p(L_p, n_{N-1}) \dots \boldsymbol{M}_I(n_{j+1}, n_j)\boldsymbol{M}_p(L_p/2, n_j). \tag{3.7}$$

To model the interaction between light and an embedded point dipole in the 1D disordered medium we calculate the Greens function in 1D that fulfill [61, 62]

$$-\nabla^2 G(z, z', \omega) - k_0^2 \varepsilon(z) G(z, z', \omega) = \delta(z - z'). \tag{3.8}$$

It describes the electromagnetic response at position z from a point source at z'. The electric field can in general be found as a superposition of point source

$$E(z, \omega) = \int_{-\infty}^{\infty} G(z, z', \omega) \frac{k_0^2}{\varepsilon_0} P(z', \omega)\, dz', \tag{3.9}$$

where $P(z)$ is the polarization of the medium. For a point dipole with dipole moment $d(\omega)$ the polarization is $P(z) = d(\omega)\delta(z - z')$ and we obtain the following expression for the electric field

$$E(z, \omega) = G(z, z', \omega) \frac{k_0^2}{\varepsilon_0} d(\omega). \tag{3.10}$$

The imaginary part of the Green's function determines the one-dimensional projected LDOS, $\rho(z_0, \omega)$, at position z_0

$$\rho(z_0, \omega) = \frac{k_0}{\pi c} \mathrm{Im}(G(z_0, z_0, \omega)) \tag{3.11}$$

which determines the spontaneous emission properties of an emitter inside the medium. It describes the optical response from the environment back to the emitter position, which modify the decay rate of the emitter.

The Greens function $G(z_0, z_0, \omega)$ can be solved analytically by separating the structure into three parts. We assume that the emitter is at position z_0 in a host layer. All the disordered layers to the right effectively form a mirror with an effective reflection coefficient r_R and likewise, the disordered layers form a effective mirror to the left with reflection coefficient r_L, whose values can be found using the transfer matrix method described above. This leaves the emitter in a cavity and the Greens function can be solved self consistently at any position in the host layer. See Ref. [59] for full details. In the limit of

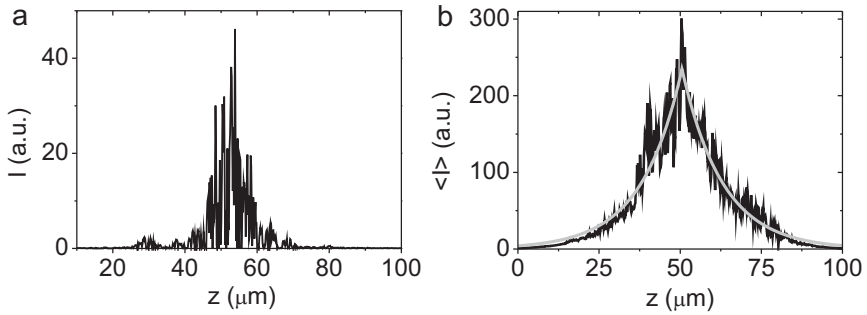

Figure 3.5: (a), Calculated intensity profile in a one-dimensional lossless medium with $\xi = 15$ μm. The thickness of the layers is $L_P = 10$ nm, the length of the structure is 100 μm, the refractive index varies within $n = 3.5 \pm 0.32$, and the monochromatic light source with $\lambda = 980$ nm is placed at $z_0 = 50$ μm. (b), Ensemble-averaged spatial intensity profile. The gray curve is a fit to the data with $I(z) = \exp(-|z - z_0|/2\xi)$.

small layer thickness compared to the wavelength the following expression can be derived [63]

$$G(z_0, z_0, \omega) = \frac{i\,c}{2\,\omega\,n(z_0)} \times \frac{1 + r_L + r_R + r_L\,r_R}{1 - r_L\,r_R}. \tag{3.12}$$

In Fig. 3.5a we show the calculated intensity $I(z) = 1/2\,n^2\,c\,|E(z)|^2$ from a point source in the center of a single realization of the disordered medium with $\Delta n = 0.32$. The intensity is clearly localized and approximately centered around the emitter. But it also shows large fluctuations with a large number of almost perfect cancelations where the intensity drops to zero. These speckle features are signatures of multiple scattering and intensity fluctuations taken over an ensemble of disorder realizations can be used as a robust method to identify Anderson localization [47]. After averaging over 10,000 different realizations of disorder all with the emitter in the center we retrieve the plot in Fig. 3.5b. The random fluctuations have been washed out as they are characteristics of the speckles for the individual realizations. The intensity profile now resembles an exponential decay away from the source. The solid line is a fit to $I(z) = \exp(-|z - z_0|/2\xi)$, from which we extract a localization length of $\xi = 15$ μm. By performing the same type of simulations for different Δn and

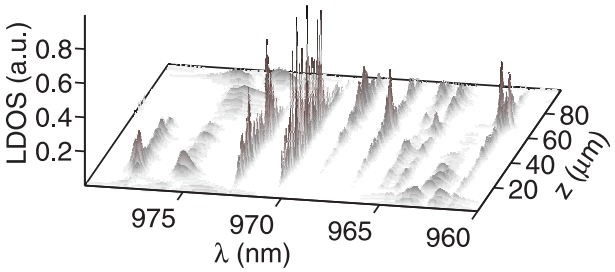

Figure 3.6: Normalized local density of states (LDOS) map calculated for a single realization along the whole 100 μm of the sample in the spectral range $960 - 980$ nm. The variation in the refractive index is $\Delta = 0.54$ corresponding to a localization length of 20 μm

keeping the layer thickness constant $L_p = 10$ nm we can extract an approximate relation between ξ/L and Δn for the given sample length, which shows a power law behavior $\Delta n = 0.22(\xi/L)^{0.548}$. This allows us to later initiate simulations with a desired localization length.

In Fig. 3.6 we have calculated the LDOS (Eq. (3.11))for positions along the whole waveguide and at the same time varied the frequency of the emitter in a spectral range between $960 - 980$ nm. In the frequency domain we see a set of separated resonances that have a well-defined and constant linewidth along the waveguide. These we identify as quasi-modes of the open disordered structure. Along the waveguide each mode shows strong speckle fluctuations similar to the intensity in Fig. 3.5. The linewidths of the modes are in general broader near the boundaries of the sample, which is expected as the loss rate out of the sample ends here is increased. The random but well-resolved spectral resonances is according to the Thouless criterium a signature of Anderson localization. Formally it stats that $\delta/\Delta < 1$ is fulfilled in the localized regime where δ is the average linewidth and Δ is the average mode spacing. It is worth noting that the intensity in Fig. 3.5 shows the field from a single emitter whereas the data in Fig. 3.6 shows the coupling strength to emitters at all positions along the waveguide. We later derive in Sec. 3.4.4 that the LDOS can be interpreted as the source–free quasi-mode intensity and they show the correct intensity for the quasi-eigenmodes of the system.

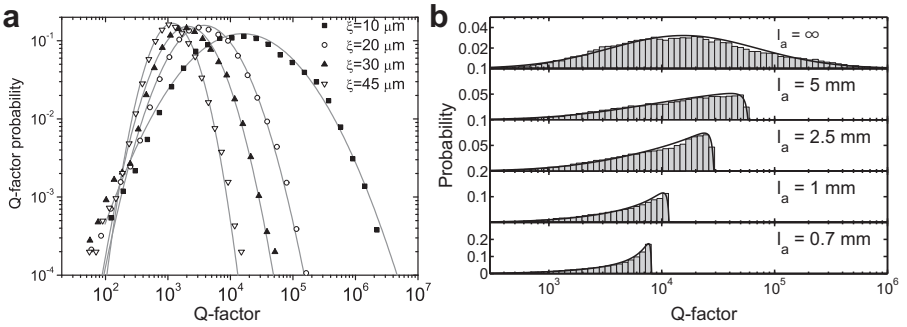

Figure 3.7: (a) Normalized Q-factor probability distributions for different localization lengths (symbols) with fits to log-normal distributions (solid lines). (b) Histograms of the Q-factor probability distributions for different values of loss length. The solid lines are fits to log-normal distributions modified to include a loss Q_{loss}-factor (see text).

3.3.1 Q-Factor Distributions

We now consider the LDOS profile for an emitter positioned in the center of the sample $\boldsymbol{r}_0 = (0, 0, L/2)$, which corresponds to drawing a line in the center of Fig. 3.6. The LDOS profile in the spectral range of $965 - 975$ nm is fitted with a sum of Lorentzian functions:

$$\rho(\boldsymbol{r}_0, \omega) = \sum_i \rho_{0,i}(\boldsymbol{r}_0) \frac{1}{\pi} \frac{\kappa_i/2}{(\omega - \omega_i)^2 + (\kappa_i/2)^2}, \tag{3.13}$$

each describing a single mode with resonance frequency ω_i, photon decay rate $\kappa_i = \omega_i/Q_i$ and amplitude $\rho_{0,i}(\boldsymbol{r}_0)$ where Q_i is the mode quality factor. We consider 8000 samples with different realizations of disorder and fits a total of 30.000-40.000 modes for each localization length. From these we get the mode Q-factor and LDOS-distributions. In this fitting process the peaks in the spectrum are first identified to determine the number of modes to fit. Modes with Q-factors below 200 are disregarded since they extend over the total fit range and likewise Q-factor above 10^7 are not captured or are fitted to a lower value due to the finite spectral resolution.

Figure 3.7a plots the extracted Q-factor probability distributions for different localization lengths, all smaller than the sample length to ensure that we are in the localized regime. Even for $\xi > L$, we still observe localized modes

but the number are reduced for a fixed number of realizations. Occasionally, single realizations localize the light even though on average the light propagation is in the ballistic regime. From the results in Fig. 3.7a it is very clear that the distributions strongly depend on the localization length with a 1-2 order increase in the most likely Q-factor in the range $\xi = 10 - 45$ μm. This is also seen from Fig. 3.8b (circles) where the ensembles average of $\langle \log(Q) \rangle$ is plotted as a function of ξ. Here, for smaller localization lengths we observe a super exponential increase in the mean Q-factors followed by an increase in the standard deviation. Especially from around 15 μm and below we see a change in the slope of the average values. Since the emitter is located in the center of the sample, this facilitate the coupling to modes located near the center and the probability of coupling to extended modes with the highest amplitude close to the edges diminishes. If we would detect the modes throughout the whole sample, and not only in the center, the average Q-factor for the same ξ would be reduced. The smallest localization length simulated is $\xi = 7$ μm as the strong increase in both mean and standard deviation drastically reduce the spectral resolution needed to resolve the spectral resonances.

It has been shown that the distribution of normalized photon decay rates $\tilde{\kappa} = \omega/Q\Delta$ is universal, meaning that the distribution of $\tilde{\kappa}$ and derived quantities only depends on the universal parameter ξ/L, where Δ is the mean spectral splitting between the modes [64]. In the localized regime, in the limit of narrow resonances ($\kappa < \exp(-2\xi/L)$), $\tilde{\kappa}$ is log-normal distributed [65, 64]. This relies on the assumption that there are no long range correlation and the modes are exponential localized with a gaussian distributed decay length. It would be interesting to test if the distribution was log-normal even in disordered periodic structures as the periodicity introduces correlation in the disorder. The solid lines in Fig. 3.7a are fits to a log-normal distribution

$$P(Q_0) = \frac{1}{\sqrt{2\pi} Q_0 \sigma} \mathrm{e}^{-\frac{(\mu - \log(Q_0))^2}{2\sigma^2}} \tag{3.14}$$

where Q_0 is the in-plane Q-factor and μ and σ are distribution parameters that depend on ξ/L and has been extracted using a most likelihood estimate for the individual values of ξ. The fits show nice correspondence with the simulated data over a span of two orders of magnitude, which is a clear indication that the statistical model accurately describes the data. Although, at low Q-factors there is a small discrepancy with slightly larger probabilities. In the limit

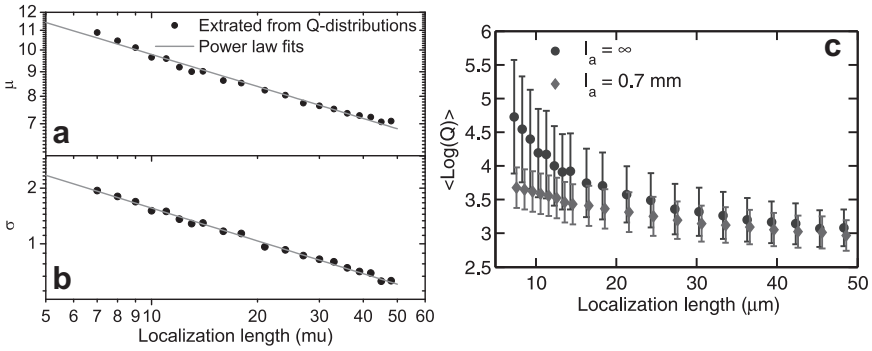

Figure 3.8: (a) Fitted distribution parameters μ and σ for the log-normal distributions as a function of localization length. The dashed lines are power law fits to the data. (b) Mean value of $\log Q$ as a function of localization length for two different values of the losses length l.

low Q-factors the distribution has been shown to follow a power law, which might account for this discrepancy. Since we are limited in the lowest Q-factors we extract we do have not enough statistics to verify this. The super exponential trend is found again in the extracted log-normal parameters $\mu(\xi)$ and $\sigma(\xi)$ shown in Fig. 3.8. For a exponential increase we would observe a linear dependence for $\mu(\xi)$. The standard deviation increases only slowly until $\sim$ 15 μm where the standard deviation for the logarithm of the Q-factors increases a factor of 2 which is again related central position of the emitter. From the solid line it is found that the two parameters approximately follow a power law with $\mu(\xi/L) = 5.9(\xi/L)^{-0.223}$ and $\sigma(\xi/L) = 0.40(\xi/L)^{-0.59}$, although $\mu(\xi)$ seems to increase slightly faster than predicted by the power law. The limited data below $\xi = 7$ μm make it difficult to assess the validity of this model to very low localization lengths. A more direct way would be to extract the mean mode splitting Δ from the simulations to test the universality of $\tilde{\kappa}$ and in this way eliminate the fitting procedure.

Q-Factor Distribution with Losses

Until now we have only considered the in-plane Q-factors in the 1D model, that account for forward and backward scattering. We can include out-of-plane scattering and other loss terms with a finite value of the imaginary part

n'' of the refractive index $n = n' + in''$. This result in a constant loss length $l = \lambda/2\pi n''$ where the field decays exponential $\boldsymbol{E}(z) \propto \exp(-z/l)$, which leads to a effective mean intensity decay length of $1/l_e = 1/2\xi + 2/l$. Both loss and localization result in a exponential decay of the intensity and this have makes it difficult to rigorously prove Anderson localization in transmission measurements in weakly absorbing media [15]. The losses reduce the maximum storage time of photons in the medium, which can be associated with a loss Q-factor $Q_l = \omega\tau_l = n'/n'' = n'\pi l/\lambda$, with λ being the wavelength of light [21]. It results in an effective Q-factor $Q^{-1} = Q_0^{-1} + Q_l^{-1}$. The loss Q-factor Q_l sets the limit of the highest value of the Q-factor that can be reached in the system as $Q \to Q_l$ for $Q_0 \to \infty$. The Q-factor distributions calculated for different loss lengths, all longer than the sample length, are shown in Fig. 3.7b for $\xi = 20$ μm, compared to the case for no absorbtion, $Q_l = l = \infty$. Most notably is the sharp cut-off that directly corresponds to Q_l. It is clear that even a small amount of loss is detrimental to achieving the highest Q-factors for a given sample length. At $\xi = 7$ μm, a loss length of $l = 0.7$ mm, which is much longer than the sample length, reduces the Q-factors with 1-2 orders of magnitude. The reason for this is the long storage times in the high Q_0 modes, effectively giving a longer propagation distance. Another important observation is the very different ways the in-plane localization and losses affect the distribution. This makes it possible to differentiate the two effects in experimental Q-factor distributions, as explained below. One thing to note is that the probability for obtaining the highest Q-factors for a given sample is higher with higher losses, which is caused by the unique reshaping of the distributions where the highest Q-factors are reduced to the limit of Q_l.

To get an analytical expression for the loss distribution, we can transform the random variable Q in the log-normal distribution by the relation $Q^{-1} = Q_0^{-1} + Q_l^{-1}$ where Q_l account for losses. Using $P_0(Q_0)$ as the log-normal distribution the modified Q-factor distribution can now be written as

$$P(Q) = \theta[Q_l - Q] \int_0^\infty dQ_0 P_0(Q_0)\, \delta\Big[Q - \big(Q_0^{-1} + Q_l^{-1}\big)^{-1}\Big] \tag{3.15}$$

where we have explicit included a Heaviside function $\theta[x]$ to ensure that $Q < Q_l$. The argument to the delta function is a nontrivial function of the integration variable Q_0 and it is therefore not possible to evaluate the integral directly.

Using the general expression for the delta function

$$\delta[g(x)] = \sum_{i=1}^{N} \frac{\delta(x - x_{0i})}{|g'(x_0 i)|}, \tag{3.16}$$

that is valid if $g(x)$ has a finite number of unique zeros, x_{0i}, we can rewrite the delta function as

$$\delta[Q - \left(Q_0^{-1} + Q_l^{-1}\right)^{-1}] = \frac{Q_l^2}{(Q - Q_l)^2}\, \delta\left[Q_0 - \frac{QQ_l}{Q_l - Q}\right]. \tag{3.17}$$

The transformed Q-factor distribution is therefore

$$P(Q) = \frac{\theta[Q_l - Q]Q_l^2}{(Q - Q_l)^2} \int_0^\infty dQ_0 P_0(Q_0)\, \delta\left[Q_0 - \frac{QQ_l}{Q_l - Q}\right] \tag{3.18}$$

$$= \frac{\theta[Q_l - Q]Q_l^2}{(Q - Q_l)^2}\, P_0\left(\frac{QQ_l}{Q_l - Q}\right) \tag{3.19}$$

and after inserting $P_0(Q_0)$ (Fig. 3.14) we get

$$P(Q) = \frac{1}{\sqrt{2\pi}\sigma(\xi)} \exp\left[-\frac{\left(\mu(\xi) - \ln\left[\frac{QQ_l}{Q_l - Q}\right]\right)^2}{2\sigma(\xi)^2}\right] \frac{Q_l \theta[Q_l - Q]}{Q(Q_l - Q)}. \tag{3.20}$$

This result is exact in the limit of uniform weak looses. The solid lines in Fig. 3.7 display the original log-normal distribution transformed according to the relations above with no free parameters. Only the log-normal parameters for the case with no losses has been fitted as described earlier. Very good correspondence between the simulated data and the analytical distributions is observed.

In this section we have extracted the Q-factor distributions for the Anderson localized modes by fitting the spectral profile of the LDOS for an ensemble of disordered waveguides. A analytical expression for the Q-factor distributions has been obtained and an approximate scaling between the distributions parameters μ and σ and ξ/L has been found. It shows a super exponential increase in the average Q-factor with smaller localization lengths. The aim of the following sections is to use the distributions of both the Q-factors and the LDOS amplitudes $\rho_0(z)$ to calculate the distributions of coupling strengths between an emitter and the ensemble of localized modes.

3.4 Cavity QED in the Local Density of States Picture

In the 1D model we can determine the LDOS at any position from the Greens function, which is sufficient to calculate the decay rate in the weak coupling regime using Fermi's golden rule. For sufficiently high Q/V_m ratios we enter the strong coupling regime where the decay becomes reversible and coherent oscillation between the emitter and photon excitation takes place.

Traditionally, the coupling between a two-level emitter and a localized quasi-mode is calculated within the Jaynes–Cummings model. In this model the coupling parameter g_{JC} depends on the mode volume V_m of the quasi-mode that is evaluated as an integral over the source–free eigenmodes of the field. The frequency dependent Greens function $G(\omega, \boldsymbol{r}_s, \boldsymbol{r})$ describes the response from the monochrome point source, which prevents us from obtaining the source–free field. In this section we write the Jaynes–Cummings model in the LDOS picture to also include the strong coupling regime. This allows us to evaluate the coupling strength directly from the Green's function without refereing to the mode volume. We later show that the mode volume can be extracted directly from the LDOS.

3.4.1 Theory of Spontaneous Emission in an Inhomogeneous Envirement

In this section we review the general equation of motion for a two-level emitter located in an inhomogeneous environment described by the LDOS. We partially follow the procedure of Ref. [66] and [62]. The two-level emitter is described by the two eigenstates $|g\rangle$ and $|e\rangle$ for the ground state and the excited state with a relative frequency ω_e. The respective raising and lowering operators are given by $\sigma_+ = |e\rangle\langle g|$ and $\sigma_- = |g\rangle\langle e|$. The quantized electromagnetic field is expanded in a continuum of plane waves

$$\hat{\boldsymbol{E}}(\boldsymbol{r}) = i \sum_{\mu} \xi_\mu \boldsymbol{e}_\mu \left[f_\mu(\boldsymbol{r}) \hat{a}_\mu \mathrm{e}^{-i\omega_\mu t} - f_\mu^*(\boldsymbol{r}) \hat{a}_\mu^\dagger \mathrm{e}^{i\omega_\mu t} \right] \tag{3.21}$$

with photon annihilation (creation) operators a_μ ($a_\mu^\dagger$) for the individual modes labeled with $\mu = \{\boldsymbol{k}_\mu, \omega_\mu\}$, $\boldsymbol{k}$-vector and frequency, ω_μ. The $\boldsymbol{e}_\mu$ is the polarization unit vector and the mode fields $\boldsymbol{f}_\mu(\boldsymbol{r}) = \boldsymbol{e}_\mu f_\mu(\boldsymbol{r})$ are normalized

as $\int \varepsilon(\boldsymbol{r}) \boldsymbol{f}_{\mu'}(\boldsymbol{r}) \boldsymbol{f}_{\mu}^{*}(\boldsymbol{r})\, d\boldsymbol{r} = \delta_{\mu',\mu}$ with $\varepsilon(\boldsymbol{r})$ being the dielectric constant and $\xi_\mu = \sqrt{\frac{\hbar\omega_\mu}{2\varepsilon_0}}$ are normalization constants that ensures that the energy in each mode is $\hbar\omega_\mu$.

The quantum mechanical interaction between the two level emitter and electromagnetic field is described by the interaction picture Hamilton

$$H = -i\hbar \sum_{\mu} \left(g_\mu \hat{\sigma}_+ \hat{a}_\mu \mathrm{e}^{-i\Delta_\mu t} - g_\mu^* \hat{\sigma}_- \hat{a}_\mu^\dagger \mathrm{e}^{i\Delta_\mu t} \right), \quad \Delta_\mu = \omega_\mu - \omega_e \tag{3.22}$$

where we have applied the dipole approximation in which we assume that field varies little over the size of the emitter and the rotating wave approximation. The coupling constants for an emitter positioned at $\boldsymbol{r}_e$ are denoted as $g_\mu = \sqrt{\omega_\mu/2\epsilon_0\hbar}\, \boldsymbol{d} \cdot \boldsymbol{f}_\mu(\boldsymbol{r}_e)$ and $\Delta_\mu = \omega_\mu - \omega_e$ are the detunings relative to the emitter frequency ω_e and $\boldsymbol{d} = |d|\hat{\boldsymbol{d}}$ is the transition dipole moment of the emitter with amplitude $|d|$ and unit vector $\hat{\boldsymbol{d}}$.

Since we are interested in the process of spontaneous emission where the excited state of the emitter decays into a continuum of (vacuum) modes and coherent reabsorption of the emitted photon, the solution is expanded in the one-excitation states $|e, \{0\}\rangle$ and $|g, \{\mu\}\rangle$. These describe the emitter being in the excited state and the electromagnetic field in the vacuum state or the emitter being in the ground state with a photon in any of the states μ

$$|\Phi^I(t)\rangle = c_e^I(t)\, |e, \{0\}\rangle + \sum_{\mu} c_\mu^I(t)\, |g, \{\mu\}\rangle \tag{3.23}$$

where $|c_e^I(t)|^2 + \sum_\mu |c_\mu^I(t)|^2 = 1$ and the superscript I denotes that we are working in the interaction picture, corotating with the emitter frequency. Inserting Eq. (3.23) into the equation of motion $i\hbar \frac{\partial}{\partial t} |\Phi^I(t)\rangle = H\, |\Phi^I(t)\rangle$ and using the orthogonality of the states we obtain an infinity set of coupled equations

$$\dot{c}_e^I(t) = -\sum_{\mu} g_\mu c_\mu^I(t) \mathrm{e}^{-i\Delta_\mu t} \tag{3.24}$$

$$\dot{c}_\mu^I(t) = g_\mu^* c_e^I(t) \mathrm{e}^{i\Delta_\mu t} \tag{3.25}$$

describing the evolution of the amplitudes of the excited states and the continuum of photon states. Since we are only interested in the evolution of the emitter the last set of equations are formally integrated

$$c_\mu^I(t) = \int_0^t g_\mu^* c_e^I(t') \mathrm{e}^{i\Delta_\mu t}\, dt' \tag{3.26}$$

and inserted back into Eq. (3.24) and we now get

$$\dot{c}_e^I(t) = -\sum_\mu |g_\mu|^2 \int_0^t c_e^I(t') \mathrm{e}^{-i\Delta_\mu(t-t')}\, dt' \tag{3.27}$$

$$= -\frac{d^2}{2\varepsilon_0\hbar} \sum_\mu \omega_\mu |f_\mu(\boldsymbol{r}_e)|^2 |\boldsymbol{e}_d \cdot \boldsymbol{e}_\mu|^2 \int_0^t g_\mu^* c_e^I(t') \mathrm{e}^{-i\Delta_\mu(t-t')}\, dt'. \tag{3.28}$$

This expression is completely general for the equation of motion for the excited state of the two level system within the dipole and rotating wave approximation. The optical properties of the environment can be described by the so-called projected local density of states (LDOS). We first make a frequency integral over $\delta(\omega - \omega_\mu)$, which leave the equations unchanged,

$$\dot{c}_e^I(t) = -\frac{d^2}{2\varepsilon_0\hbar} \sum_\mu \int_0^\infty \int_0^t \omega \delta(\omega - \omega_\mu) |f_\mu(\boldsymbol{r}_e)|^2 |\boldsymbol{e}_d \cdot \boldsymbol{e}_\mu|^2 \times c_e^I(t') \mathrm{e}^{-i(\omega-\omega_e)(t-t')}\, dt' d\omega \tag{3.29}$$

and then define the projected LDOS as

$$\rho(\omega, \boldsymbol{r}_e) = \sum_\mu |f_\mu(\boldsymbol{r}_e)|^2 |\boldsymbol{e}_d \cdot \boldsymbol{e}_\mu|^2 \delta(\omega - \omega_\mu). \tag{3.30}$$

The projected LDOS consist of a trace over all the different plane wave modes weighted by the field intensity at each position projected onto a given polarization. It contains the response the local optical environment at the emitter position $\boldsymbol{r}_e$. The equation of motion can thus be described by

$$\dot{c}_e^I(t) = -\frac{d^2}{2\varepsilon_0\hbar} \int_0^\infty \int_0^t c_e^I(t') \omega \mathrm{e}^{-i(\omega-\omega_e)(t-t')} \rho(\omega, \boldsymbol{r}_e)\, dt' d\omega$$

$$= -\int_0^t F(t-t') c_e^I(t')\, dt', \tag{3.31}$$

where $F(\tau)$ acts as a memory kernel which describes the mean effect on the emitter amplitude from the optical environment from all earlier times. We have therefore lost track of the amplitudes of the individual plane wave modes but kept the weighted coupling strength to modes with different frequencies. For a delta response in time corresponding to a flat frequency response we recover the exponential decay associated with pure spontaneous emission in a homogenous medium. Including the response from $t' < t$ allows for non-Markovian evolution

of the emitter. The explicit form of $F(\tau)$ is

$$F(\tau) = \frac{d^2}{2\varepsilon_0\hbar}\int_0^\infty \omega \mathrm{e}^{-i(\omega-\omega_e)\tau}\rho(\omega,\boldsymbol{r}_e)\,d\omega. \tag{3.32}$$

We now have a description for a two-level emitter coupled to a electromagnetic vacuum field in an in-homogenous medium, where the effect of the optical environment is fully determined through the LDOS, $\rho(\omega,\boldsymbol{r}_e)$. In many cases the Wigner-Weisskopf approximation can be applied were it is assumed that the LDOS only changes slowly near the emitter frequency and both ω_e and $\rho(\omega,\boldsymbol{r}_e)$ can be taken out of the integral. After extending the integral to $-\infty$, Eq. (3.32) simplifies to

$$F(\tau) = \frac{d^2\omega}{2\varepsilon_0\hbar}\rho(\omega,\boldsymbol{r}_e)\int_{-\infty}^\infty \mathrm{e}^{-i(\omega-\omega_e)\tau}d\omega = \frac{d^2\omega}{2\varepsilon_0\hbar}\rho(\omega,\boldsymbol{r}_e)2\pi\delta(\tau) \tag{3.33}$$

and inserting back into Eq. (3.31) we get the standard result $\dot{c}_e^I(t) = -\frac{\Gamma}{2}c_e^I(t)$ for in exponential decay with decay rate

$$\Gamma = \frac{\pi\omega}{\varepsilon_0\hbar}d^2\rho(\omega,\boldsymbol{r}_e). \tag{3.34}$$

In the time integral in Eq. (3.31) we have divided by a factor 2 as we are only integrate over half the delta function $\delta(\tau)$[1]. Apart from very simple structures it is difficult to calculate the full 3D LDOS. However, by assuming a simple form for the LDOS it is possible to solve the equation of motion.

3.4.2 Coupling to a Cavity Density of States

To describe the coupling to a standard optical cavity with a finite photon life time located deep in the PhC band gap we insert a normalized Lorentzian as a model LDOS, with the same form as in Eq. (3.13), albeit here in a 3D version,

$$\rho(\omega,\boldsymbol{r}_e) = \rho_0(\boldsymbol{r}_e)\frac{1}{\pi}\frac{\kappa/2}{(\omega-\omega_c)^2+(\kappa/2)^2}. \tag{3.35}$$

Here κ is the cavity linewidth and the Q-factor is given by $Q = \omega_c/\kappa$. $\rho_0(\boldsymbol{r}_e)$ is a position dependent amplitude that account for the exact field strength of the cavity field at the emitter position. This LDOS separates the position and frequency dependence and makes it possible to solve the dynamics of the

[1] This is a common way to deal with this integral but not formally correct.

emitter analytically. For large Q-factors the LDOS changes rapidly near the emitter frequency and the Wigner-Weisskopf approximation is not valid. We first perform the frequency integral in $F(\tau)$ (Eq. (3.32)),

$$F(\tau) = \frac{d^2\rho_0(\boldsymbol{r}_e)\kappa}{4\varepsilon_0\hbar\pi}\mathrm{e}^{i\omega_e\tau}I(\tau) \tag{3.36}$$

$$I(\tau) = \int_0^\infty \frac{\omega\mathrm{e}^{-i\omega\tau}}{(\omega-\omega_c)^2+(\kappa/2)^2}\,d\omega. \tag{3.37}$$

The denominator in Eq. (3.37) can be rewritten as $(\omega-\omega_c)^2+(\kappa/2)^2 = (\omega-\tilde{\omega}_c)(\omega-\tilde{\omega}_c^*)$ where $\tilde{\omega}_c = \omega_c^R - i\kappa/2$ is a complex cavity frequency. Notice the minus sign in the definition. The integral can be evaluated as a contour integral over the lower complex half plane Ω^- after extending the lower limit of the integrand to $-\infty$. This is a good approximation as frequencies below zero are far away from the cavity resonance that is sharply peaked around ω_c. For $t-t'>0$ the absolute value of the integrand converges to zero for $\omega\to -i\infty$ and only the integral over the real axis survives. The complex conjugate of ω_c is located in the upper half plane and we can evaluate the integral by only taking the residues at $\omega=\omega_c$.

$$I(\tau) = \int_{\Omega^-} \frac{2\omega\mathrm{e}^{-i\omega\tau}}{2i\kappa}\left(\frac{1}{\omega-\tilde{\omega}_c}-\frac{1}{\omega-\omega_c^*}\right)d\omega \tag{3.38}$$

$$= 2\pi i \operatorname*{Res}_{\omega=\tilde{\omega}_c}\left(\frac{\omega\mathrm{e}^{-i\omega\tau}}{i\kappa}\frac{1}{\omega-\tilde{\omega}_c}\right) = \frac{2\pi\tilde{\omega}_c\mathrm{e}^{-i\tilde{\omega}_c\tau}}{\kappa}. \tag{3.39}$$

Inserting back we get the simple form of $F(\tau)$

$$F(\tau) = \frac{d^2\rho_0(\boldsymbol{r}_e)\tilde{\omega}}{2\varepsilon_0\hbar}\,\mathrm{e}^{-i\Delta\tilde{\omega}_c\tau} = \tilde{\beta}\mathrm{e}^{-i\Delta\tilde{\omega}\tau} \tag{3.40}$$

where the following constants have been introduced:

$$\Delta\tilde{\omega} = \tilde{\omega}_c - \omega_e = \Delta\omega - i\kappa/2,$$

$$\tilde{\beta} = \frac{d^2\rho_0(\boldsymbol{r}_e)\tilde{\omega}_c}{2\varepsilon_0\hbar} = \beta^2 - i\beta^2\alpha, \quad \beta^2 = \frac{d^2\rho_0(\boldsymbol{r}_e)\omega_c}{2\varepsilon_0\hbar}, \quad \alpha = \frac{\kappa}{2\omega_c} = \frac{1}{2Q}. \tag{3.41}$$

The definition of $\tilde{\beta}$, that act as a the coupling strength, contains the complex cavity frequency $\tilde{\omega}_c$ and for convenience we have introduced a normalized imaginary part. The implications of this will be studied later.

We now solve Eq. (3.31) with a Laplace transformation. The equation of motion in the Laplace domain with the initial condition $c_e^I(0)=1$, initiating

the emitter in the excited state, now reads

$$\begin{aligned} sC_e^I(s) - 1 &= -F(s)C_e^I(s) \\ C_e^I(s) &= \frac{1}{s + F(s)} \end{aligned} \tag{3.42}$$

where the Laplace transformation of $F(\tau)$ is

$$F(s) = \beta \int_0^\infty \mathrm{e}^{-i\Delta\tilde{\omega}\tau}\, \mathrm{e}^{-s\tau}\, d\tau = \tilde{\beta}\frac{1}{s + i\Delta\tilde{\omega}}. \tag{3.43}$$

The emitter spectrum in the Laplace domain is thus given by

$$C_e^I(s) = \left(s + \tilde{\beta}\frac{1}{s + i\Delta\tilde{\omega}}\right)^{-1} = \frac{s + i\Delta\tilde{\omega}}{s(s + i\Delta\tilde{\omega}) + \tilde{\beta}}. \tag{3.44}$$

The resonances of the spectrum in Eq. (3.44) can be obtained from the zeros of the denominator

$$s_{+/-} = \frac{1}{2}\left(-i\Delta\tilde{\omega} \pm \sqrt{(i\Delta\tilde{\omega})^2 - 4\tilde{\beta}}\right) = -\frac{1}{2}i\left(\Delta\tilde{\omega} \mp \sqrt{\Delta\tilde{\omega}^2 + 4\tilde{\beta}}\right) \tag{3.45}$$

and after substituting back $\Delta\tilde{\omega} = \Delta\omega - i\kappa/2$ and $\tilde{\beta} = \beta^2 - i\beta^2\kappa/(2\omega_c)$ and transforming to the frequency domain and back to the Schrödinger picture $\omega_{+/-} = i\, s_{+/-} - \omega_e$ we obtain the final form for the two resonance of the emitter spectrum,

$$\omega_{+/-} = \frac{1}{2}(\omega_c + \omega_e) - \frac{i\kappa}{4} \pm \sqrt{\frac{1}{4}\Delta\omega\,(\Delta\omega - i\kappa) + \beta^2 - \left(\frac{\kappa}{4}\right)^2 - \frac{i\beta^2\kappa}{2\omega_c}} \tag{3.46}$$

For zero detuning $\Delta\omega = 0$ resulting in $\omega_c = \omega_e = \omega$ and in the limiting case of high Q we can Taylor expand the expression around $\alpha = 1/2Q = 0$ to the lowest order and we end up with

$$\omega_{+/-} = \omega - \frac{i\kappa}{4} \pm \sqrt{\beta^2 - \left(\frac{\kappa}{4}\right)^2} \tag{3.47}$$

plus additionally higher order terms in α that we discard. This expression is completely equivalent to the expression obtained in ref. [67] with $\beta \equiv g$ for the standard Jaynes–Cummings model for a two level model coupled to a single cavity quasi-mode. We have proved that in the limit of high Q-factor that the two models are equivalent. Instead of using the mode volume as a

figure of merit the coupling parameter β contains the LDOS amplitude at the emitter position $\rho_0(\boldsymbol{r}_e)$. From Eq. (3.47) we can retrieve the strong coupling criterium with occurs when the spectrum splits up into two distinct frequency resonances for a real valued square root. This happens for $\beta > \kappa/4$ where the eigenfrequencies splits up into two polariton branches. Reinserting β and κ we arrive at

$$\frac{\rho_0(\boldsymbol{r}_e)Q^2}{\omega_c} > \frac{\varepsilon_0\hbar}{8d^2}. \tag{3.48}$$

Similarly we retrieve the decay rate in the weak coupling limit $\beta \ll \kappa$

$$\Gamma_c = -2\mathrm{Im}[\omega] \approx \frac{4\beta^2}{\kappa} \tag{3.49}$$

Together with the decay rate in a homogenous medium

$$\Gamma_{\mathrm{hom}} = \frac{\omega^3 d^2}{3\pi\varepsilon_0\hbar c^3} \tag{3.50}$$

we obtain the expression for the Purcell factor into a cavity

$$F_p = \frac{\Gamma_c}{\Gamma_{\mathrm{hom}}} = \frac{4\beta^2}{\kappa\Gamma_{\mathrm{hom}}} = \frac{3\lambda^3 Q\rho_0(\boldsymbol{r}_e)}{4\pi^2 n}, \tag{3.51}$$

which we see is proportional to both the Q-factor and the LDOS amplitude and has a similar from as the one in Ref. [67]. Compared to same expression there we have absorbed a factor of $\varepsilon = n^2$ into $\rho_0(\boldsymbol{r}_e)$ due to differences in the normalization. The right hand size of Eq. (3.48) only contains physical constants and the dipole moment of the emitter. For a fixed emitter size, the dipole matrix element is constant and the strong coupling criterium only depends on the optical properties on the left hand side. For the Anderson localized modes it depends on the mutual distribution of $\rho_0(\boldsymbol{r}_e)$ and Q^2. The Q^2 dependence implies that the values of the cavity confinement have a large influence on the probability of achieving strong coupling.

3.4.3 Cavity Assisted Lamb Shift

As a curiosity we look at the effect of the small imaginary term in the square root of Eq. (3.47). It results in an additional frequency shift and a modification of the decay rate. These shifts arise from the different coupling strength $g(\omega)$ to the different frequency components of the cavity. For example, the coupling

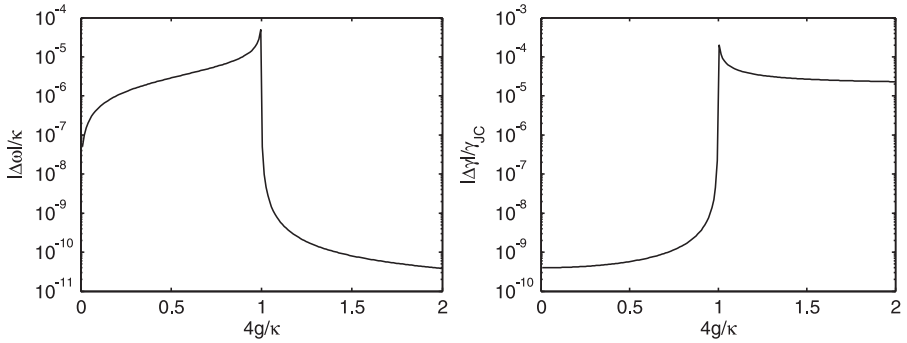

Figure 3.9: (a) Absolute value of the frequency shift for one of the polariton branches relative to the frequency obtained in the Jaynes–Cummings model $|\mathrm{Re}[\omega_\alpha - \omega_{\alpha=0}]|/\mathrm{Re}[\omega_{\alpha=0}]$ as a function of the coupling parameter β. All the frequencies are normalized by the cavity linewidth κ. (b) Similarly the relative change in emitter decay rate $|\mathrm{Im}[\omega_\alpha - \omega_{\alpha=0}]|/\mathrm{Im}[\omega_{\alpha=0}]$. The position $4\beta/\kappa = 1$ marks the transition to the strong coupling regime.

to higher frequencies requires more energy and the reverse is true of the lower frequency modes. This asymmetry creates the additional shift in the frequency of the two eigenfrequencies of the system. This can be interpreted as a cavity assisted Lamb shift in addition to the Lamb shift from the coupling to the continuum of vacuum modes in the surrounding medium. The same interpretation was presented in Ref. [7], derived from a Dyadic Greens function formalism. In figure Fig. 3.9 the absolute values of the relative shifts is plotted for both the frequency and decay rate. Even in the weak coupling regime is there a small splitting between the eigenmodes. Although, the absolute scale is very small between $10^{-6} - 10^{-4}$ relative to the linewidth of the cavity and this would be extremely difficult to measure.

3.4.4 Mode Volumes from the Local Density of States

Although we do not need the mode volume in calculating the coupling strength (Eq. (3.48) and (3.51)) we would like to obtain estimates of the mode volume as a figure of merit. We here show that we can estimate the mode volume from the LDOS amplitude. In the Jaynes–Cummings mode for the coupling of a two-level emitter to a single optical mode, the coupling parameter g_{JC} is given

by

$$g_{JC} = \sqrt{\frac{\omega_c}{2\varepsilon_0 \hbar}}\, d \cdot |\boldsymbol{e}_d \cdot \boldsymbol{\mathcal{E}}_c(\boldsymbol{r}_e)| \tag{3.52}$$

where $\mathcal{E}_c(\boldsymbol{r}_e)$ is the single quasi-mode field that is normalized in the same way as the individual plan wave modes in eq. Eq. (3.21). The quasi-mode field does not have a single well-defined polarization so the polarization is included in $\boldsymbol{\mathcal{E}}_c(\boldsymbol{r}_e)$. The mode volume V_m is introduced as a normalization parameter by defining a new field

$$\boldsymbol{\mathcal{E}}_c(\boldsymbol{r}) = \frac{1}{\sqrt{\varepsilon_{\max} V_m}} \boldsymbol{f}_c(\boldsymbol{r}) \tag{3.53}$$

where $\boldsymbol{f}_c(\boldsymbol{r})$ is normalized such that $\max\{|\boldsymbol{f}_c(\boldsymbol{r})|\} = 1$. From the normalization of $\boldsymbol{\mathcal{E}}_c(\boldsymbol{r})$ we get the following expression for V_m

$$V_m = \frac{1}{\varepsilon_{\max}} \int \varepsilon(r) |\boldsymbol{f}_c(\boldsymbol{r})|^2 d\boldsymbol{r}. \tag{3.54}$$

From previous comparison we identify that $g_{JC} = \beta$ and then find that

$$\rho_0(\boldsymbol{r}) = |\boldsymbol{e}_d \cdot \boldsymbol{\mathcal{E}}_c(\boldsymbol{r})|. \tag{3.55}$$

Combining the last three equations and assuming that the polarization of the cavity field is almost constant and parallel to the dipole moment of the emitter such that $|\boldsymbol{e}_d \cdot \boldsymbol{\mathcal{E}}_c(\boldsymbol{r})| \approx \mathcal{E}_c(\boldsymbol{r})$ we get a mode volume in terms of $\rho_0(\boldsymbol{r})$

$$V_m = \frac{\int \varepsilon(\boldsymbol{r}) \rho_0(\boldsymbol{r}) d\boldsymbol{r}}{\max_{\boldsymbol{r}}[\varepsilon(\boldsymbol{r}) \rho_0(\boldsymbol{r})]}. \tag{3.56}$$

Effective 1D Model Density of States

The model described above is inherently 3D so to use the LDOS calculated for the 1D model in Sec. 3.3 we need to make assumption about the spatial profile perpendicular to the 1D model. We make the Ansatz that the plane waves and the refractive index modulation in Eq. (3.21) can be separated into a components along the waveguide $f_\mu(z)$ and a single mode profile perpendicular to it, $f_\perp(x, y)$ [50]

$$f_\mu(\boldsymbol{r}) = \boldsymbol{e}_\mu f_\perp(x, y) f_\mu(x, y) \tag{3.57}$$

where $f_\perp(x, y)$ is normalized such that $\int \tilde{\varepsilon}(x, y) f_\perp(x, y) f_\perp^*(x, y)\, dxdy = 1$ and $\tilde{\varepsilon}(x, y)$ is the normalized $\varepsilon(x, y)$. Similar to the mode volume, we introduce an effective area of the perpendicular mode profile as $f_\perp(x, y) = 1/(\sqrt{A_{\text{eff}}}) \tilde{f}_\perp(x, y)$

where $\tilde{f}_\perp(0,0) = 1$, assuming that the profile has a maximum in $(x,y) = (0,0)$. Inserting Eq. (3.57) into the expression for the LDOS in Eq. (3.30)

$$\rho(\omega, \boldsymbol{r}_e) = \sum_\mu |f_\perp(x,y) f_\mu(z)|^2 |\boldsymbol{e}_d \cdot \boldsymbol{e}_\mu|^2 \delta(\omega - \omega_\mu) \tag{3.58}$$

and using only one transverse mode

$$= |f_\perp(x,y)|^2 \sum_\mu |f_\mu(z)|^2 |\boldsymbol{e}_d \cdot \boldsymbol{e}_\mu|^2 \delta(\omega - \omega_\mu) \tag{3.59}$$

$$= |f_\perp(x,y)|^2 \rho^{1D}(\omega, z) \tag{3.60}$$

where $\rho^{1D}(\omega, z)$ is the 1D LDOS from Eq. (3.13). Since we assume the emitter to be centered on the waveguide $\boldsymbol{r} = (0,0,z)$ we get

$$\rho(\omega, z) = \frac{1}{A_{\text{eff}}} \tilde{f}_\perp(0,0) \rho^{1D}(\omega, z) = \frac{1}{A_{\text{eff}}} \rho^{1D}(\omega, z). \tag{3.61}$$

The mode volume can be calculated by inserting in Eq. (3.56) and again using the separability between the transverse and parallel directions

$$V_m = A_{\text{eff}} \frac{\int \varepsilon(z) \rho_0^{1D}(z) dz}{\max_z [\varepsilon(z) \rho_0(\boldsymbol{r})]} \tag{3.62}$$

and

$$A_{\text{eff}} = \int \tilde{\varepsilon}(x,y) |\tilde{f}_\perp(x,y)|^2 \, dxdy. \tag{3.63}$$

3.4.5 Mode Volume Distributions

As discussed in the beginning of the chapter we can model the disordered PhC waveguides with our 1D model, which rely on that all statistical observables are determined by the universality of the parameters ξ/L and ξ/l. To calculate the mode volume from Eq. (3.62) we need to integrate over the position depended LDOS amplitude for one of the modes shown earlier in the Fig. 3.6 on page 47. The integral in Eq. (3.62) is evaluated over the total 1D waveguide length, but we neglect the field leaking from the ends.

In order to calculate A_{eff} we consider realistic parameters of a PhC waveguide similar to the ones used in Sec. 3.2 with lattice constant $a = 260$ nm, hole radius $r = 0.30a$ and membrane thickness of 150 nm and refractive index of 3.44. We still use a sample length of 100 μm. The field distribution for the zero

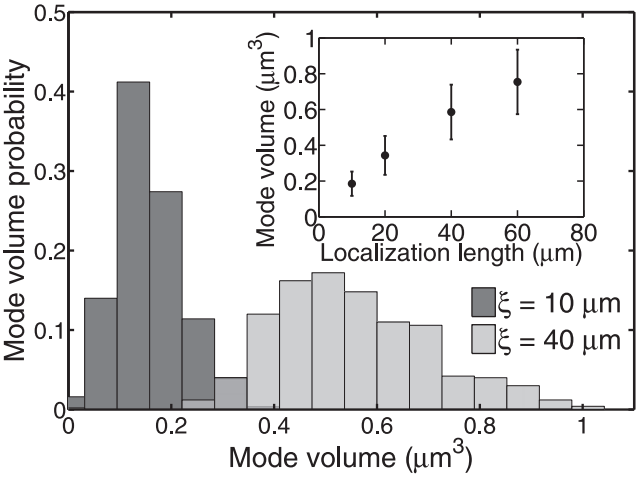

Figure 3.10: Histograms of the normalized mode volume probability calculated for 500 realization of disorder, for two values of localization length ξ. The transverse effective area is calculated with the specific parameters of a test PhC waveguide (see text). Inset: Mean values and standard deviations of the calculated mode volumes, plotted as a function of localization length.

order waveguide mode at the band edge for an ordered waveguide is calculated with the MPB software and, averaging over one unit cell along the waveguide, we obtain a value of $A_{\text{eff}} \equiv \langle A_{\text{eff}} \rangle = 0.0356\ \mu\text{m}^2$.

Averaging over 500 realization we obtain the mode volume distributions shown in Fig. 3.10 for two different values of the localization length. The small number of data points relative to the Q-factors is due to the much higher computational demand. The LDOS have to be calculated across the whole sample instead of only at one point for each realization. As expected, due to the stronger mean field confinement of the exponentially decaying modes, the distributions shift towards lower values and narrow with decreasing localization length. This trend is shown in the inset of Fig. 3.10 for the mean value and the standard deviation of the mode volumes, plotted as a function of the localization length. The smallest mode volume obtained in our simulations for $\xi = 10\ \mu\text{m}$ is $V_m \simeq 0.07\ \mu\text{m}^3 \approx 3(\lambda/n)^3$ comparable to mode volumes commonly obtained for PhC nano-cavities [68], where values of $V_m \lesssim (\lambda/n)^3$ can be achieved. The calculated mode volumes for $\xi < 40\ \mu\text{m}$ are below $1\ \mu\text{m}^3$, which

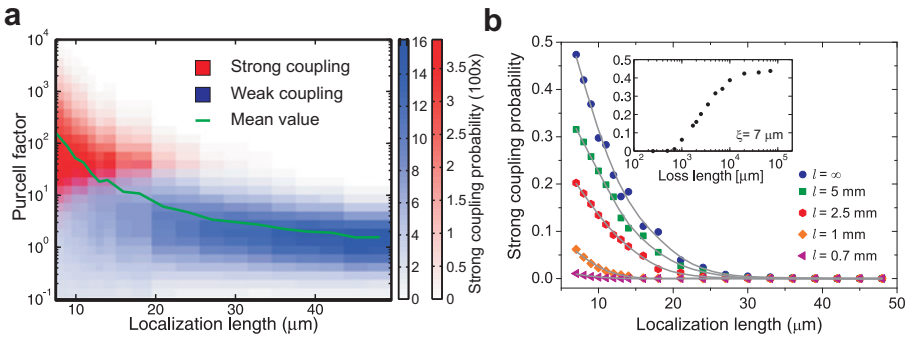

Figure 3.11: (a) Probability of obtaining a Purcell factor $F_p = 4\alpha/k\Gamma_{\text{hom}}$ for an InAs quantum dot, positioned in the center of a 100 μm-long one-dimensional disordered system and coupled to an Anderson localized mode, plotted as a function of the light localization length. The color scale represents the probability of finding a realization in the weak (blue) and strong (red) coupling regime, respectively. The green line represents the mean value of F_p. (b) Probability to achieve the light-matter strong coupling regime plotted as a function of localization length for different loss lengths. The solid lines are guides to the eye. Inset: Probability of achieving the strong coupling regime for a system with light localization length of 7 μm, plotted as a function of loss lengths.

is consistent with results extracted from decay rate measurements in Ref. [46]. In combination with the results for the Q-factor distributions this shows that it is possible to simultaneous enhance the mean Q-factors and reduce the mode volumes by reducing the localization length.

3.4.6 Distribution of Coupling Parameters and Strong Coupling Probability

Inserting the Q-factor and $\rho_0(\boldsymbol{r}_0)$ values obtained from the fitted modes in the 1D waveguide model in Sec. 3.3 into Eq. (3.48) and Eq. (3.51) and using the dipole moments measured for InAs quantum dots $d = 0.64$ e nm [28], we obtain the results presented in Fig. 3.11a. Here the Purcell factor probability is plotted as a function of localization length and color coded accordingly to whether the individual bin represents the system in the weak (blue) or strong (red) coupling regime. The Purcell factor is here used as a figure of merit in

both the weak and strong coupling regime although it is only a directly measurable quantity in the former. As expected from the Q-factor distributions (see, inset of Fig. 3.8c), the ensemble averaged F_p (green line) increases super exponentially when decreasing ξ: the probability of achieving the strong coupling regime therefore increases drastically when reducing the localization length as show in Fig. 3.11b, blue circles. For $\xi > 25$ µm the fraction of strongly coupled systems is found to be smaller then 1%, while for the shortest localization length simulated $\xi = 7$ µm we obtain a strong coupling probability of almost 50%. The main reason for these high probabilities is the probability of the very high in-plane Q-factors, up to 10^6, far above the state of the art in real PhC cavities with emitters. For the mode volumes, only the lower tails of the distributions touches the experimentally realizable mode volumes. We emphasize that in the simulations the emitter has not been optimally positioned with respect to the antinode of the LDOS, although still located in the center far from the edges. This depicts the common experimental situation where the emitter position cannot be accurately determined. It might be interesting to study the statistics for completely random emitters and emitters optimally positioned, which has experimentally been realized [3].

The presence of losses result in a strong modification of the Q-factor distributions (see Fig. 3.8b) which translate into a reduced coupling strength for smaller loss lengths. Figure 3.11b presents a detailed analysis of the probability to observe strong coupling as a function of localization length for different loss lengths, which is seen to decreases with the loss lengths as expected. In particular, the inset of Fig. 3.11b shows that losses can dominate the probability of finding an emitter strongly coupled to a cavity mode, i.e. for $\xi = 7$ µm the probability drops from $\sim 50\%$ in the lossless case to 1% for an absorption length shorter than 1 mm, which is still 10 times the sample length. In between there is a order of magnitude where the probability slowly rises until a threshold in reached around 10 mm. We can make an estimate for the probability of observing strong coupling from the results of Ref. [69]. From here we can extract a rough estimate for the out-of-plane losses for a PhC structure with $a = 260$ nm and $r = 0.3a$ with random perturbations in the hole diameter of 1 nm and considering the onset of localization occurring for group velocities $n_g = 50 - 100$ [69]. We obtain $l \sim 2.5 - 20$ mm and for $l \sim 2.5$ mm we calculate a probability of strong coupling from 10 to 20% for localization lengths ranging

from 15 to 7 μm (Fig. 3.11(b), red symbols).

3.5 Conclusion

In this chapter FDTD simulations of 2D disordered PhC waveguides have been performed. A dense spectrum of resonances is observed near and below the band edge of the PhC waveguide, representing localized modes distributed throughout the waveguide structure. A variety of different mode sizes has been observed with the smallest one only spanning a few lattice constants along the waveguide, and all the modes are confined to the waveguide structure. A 1D waveguide model has been used to study the statistical properties of the Anderson localized modes of the PhC. From an ensemble of waveguides the distributions of mode Q-factors and local density of state amplitudes for an emitter in the center of the waveguide has been extracted. The ensemble averaged Q-factors are shown to increase super exponentially with decreasing localization length, owing to the exponential confinement of the modes. The effect of a single loss parameter on the distributions is evaluated, which truncate the log-normal distribution in a characteristic manner that makes it possible to distinguish in-plane confinement and losses for the Q-factor distributions. A theory of the emitter–cavity coupling in the density of states picture has been solved analytically. This model is used to calculate the distributions for the emitter–cavity coupling strength and from these the strong coupling probability. For lower localization length the coupling strength is seen to drastically increase with a simultaneous decrease in the mode volume. Thus, the strong coupling probability increases for smaller localization lengths, up to 50% for $\xi = 7$ μm. For a realistic amount of losses a strong coupling probability of 10-20% is estimated for a disordered PhC waveguide.

Chapter 4

Experiments on Disordered Photonic Crystal Waveguides

4.1 Introduction

In the previous chapter we showed that strongly localized modes form near the band edge of the PhC waveguide band edge. The spectral position of the modes can therefore be controlled through band engineering of the waveguide mode. From the statistical model very large Q-factors have been observed. The Anderson localized modes can therefore by used as a elegant way of constructing high-Q localized modes for cavity QED at a designed wavelength without relying on nano-size fine tuning of cavity structures. We now test these predictions experimentally and measure the distributions of Q-factors in disordered PhC and from an comparison with the waveguide model in Sec. 3.3 extract the localization length and loss length as a function of disorder. Finally, we measure the QED effects and for the QED experiments we need to embed emitters in the PhC waveguide.

The traditional method to determine the light propagation in disordered media is through transmission experiments in passive structures. The ensemble averaged light intensity is measured as a function of the sample length,

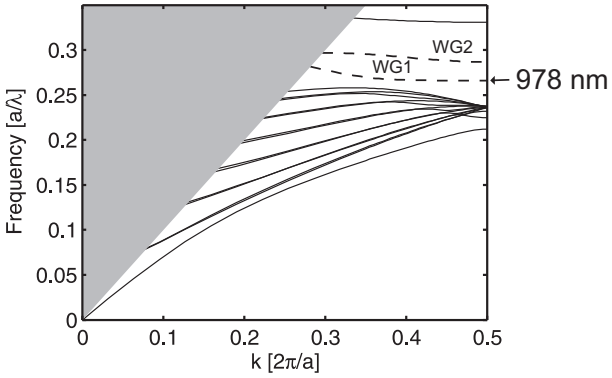

Figure 4.1: Band structure diagram for a PhC membrane waveguide with membrane thickness 150 nm, lattice constant $a = 260$ nm and, hole radius $r = 78$ nm. The dashed lines mark the first two gap guided waveguide modes. (see Chapter 2 for a detailed description of the band structure.)

which gives a exponential decay related to the localization length. However, this method is ambiguous in the presence of losses, as these also lead to an exponential decay and only the extinction mean free length can be extracted. Intensity fluctuations has been shown to accurately describe the transition to localization but the localization length is not reliably extracted [15]. In Sec. 3.3.1 we saw that the distribution of Q-factor shows very distinct features making it possible to distinguish between in-plane Anderson localization and losses. Transmission measurements preferable excite modes near the light source, but with the embedded emitters we are able to efficiently excite all modes along the waveguide to obtain more statistics of the Q-factors.

4.2 Disordered Photonic Crystal Waveguide Samples

To study the effect of disorder in 1D systems we have fabricated a set of PhC waveguide samples with varying amounts of disorder. The design of the ideal PhC waveguide is similar to the one used in Chapter 2 but fabricated from a different batch of wafers. They consist of an under-etched 150 nm think GaAs membrane in which a set of holes have been etched in a hexagonal lattice to

form the PhC with a single row left out to form the waveguide. A single layer of InAs quantum dots with a density of 80 μm^{-2} is embedded in the membrane. The inhomogeneous broadened quantum dot spectrum has wavelengths in the interval 960 ± 30 nm. Compared to the PhC waveguides used in Chapter 2, these samples have a better optical quality and a smoother bottom side of the membrane leading to much lower out-of-plane losses. A scanning electron microscope (SEM) image showing a cleaved sample is shown in Fig. 4.2a. The measurements have been performed on $L = 100$ μm long samples with lattice constant $a = 260$ nm and hole radius $r = 78$ nm. The band structure is presented in Fig. 4.1 with a simulated cut-off wavelength for the waveguide mode at 978 nm. A lithographically controllable amount of disorder is introduced: the holes in the three rows on either side of waveguide have been moved from their ideal positions with a Gaussian random distribution. This encapsulates the disordered waveguide system in a 2D PhC, which preserves the preferential 1D nature of the system. The amount of induced disorder is determined by the standard deviation of the Gaussian distribution δ and range from $\delta = 0.00a - 0.06a$ in $0.01a$ steps. The samples will be referred to as 0% to 6% disorder. An example showing a SEM image of a sample with 6% disorder is seen in Fig. 4.2b, where the red circles represent the ideal positions of the holes without disorder. All the samples including the reference sample with $\delta = 0\%$ suffer from an intrinsic fabrication disorder of $1 - 2$ nm in the hole roughness and radius, which sets a lower limit on the amount of disorder we can study to approximately $\delta = 1\%$.

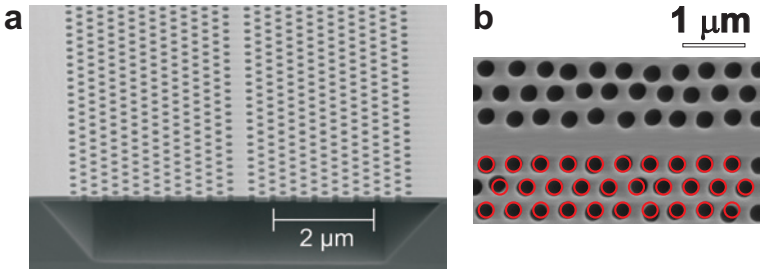

Figure 4.2: (a) Scanning electron microscope (SEM) image of a PhC waveguide membrane where the sample has been cleaved to show the edge of the membrane. The waveguide is formed by leaving out a rows of hole in the PhC. (b) SEM image the disordered PhC waveguide where the holes in 3 rows of holes on both sides of the waveguide have been randomly moved with a standard deviation of 6% of the lattice constant. The red circles are positioned on the location of the holes in an ideal PhC on one side of the waveguide.

4.3 Statistics of Anderson Localized Modes in Disordered Waveguides

In this experiment we are interested in the statistics of the confined Anderson modes in the disordered PhC waveguides. Especially, we focus on the Q-factors and the spatial extend of the modes to extract information on the ensemble averaged quantities like localization and loss length. The embedded quantum dots are used as internal light sources to efficiently excite the modes and are therefore pumped at a high pump power of 2 kW/cm^2. This fully saturate the quantum dots and effectively forms a broadband light source. A confocal micro-PL setup identical to the one used in Chapter 2 is used, although with a higher resolution spectrometer. The sample is located in a Helium flow cryostat at 10 K. A Ti:sapphire laser emitting at 800 nm, in CW mode, is focused through a N=0.65 microscope objective to an excitation spot of 1.4 µm FWHM on the sample. The emitted photoluminescence signal is collected using the same objective, spatially filtered to the same spot-size with the core of a single mode fiber, sent through a $f = 50$ cm spectrometer and detected with a CCD array. The resolution of the spectrometer is 0.05 nm given as the FWHM of the IRF measured with the lines of a Xe lamp. This allow us to extract the spatial

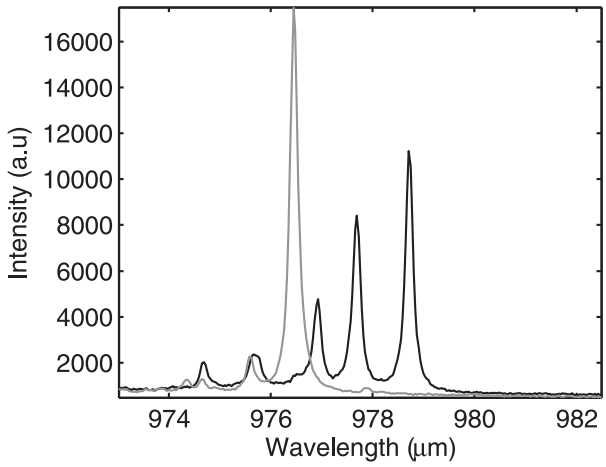

Figure 4.3: Example of photoluminescence spectra obtained under high pump power (2 kW/cm^2) at two different positions along a waveguide with only intrinsic fabrication disorder $\delta = 0\%$. The 3 largest peaks for position 1 have $Q = \{5430, 6400, 7260\}$ and the largest peak for position 2 has $Q = 1562$.

dependence and to resolve cavities with Q-factors up to 20.000.

4.3.1 Spectral Signature of Anderson Localized Modes

Photoluminescence spectra obtained at two different positions along a single PhC waveguide with 0% disorder are plotted in Fig. 4.3. Several random and well-resolved resonances are visible in the slow light region of the waveguide mode, which is a signature of Anderson localization. The above-mentioned modes exhibit Q-factors between 1500 and 7600. These values are extracted by first numerically deconvoluting the spectra with the measured IRF, and then fitting the main peaks with a multi-Lorentzian function from which the amplitude, center wavelength λ_c, and FWHM, Γ, are extracted. The Q-factors are extracted as $Q = \lambda_c/\Gamma$. Before the fitting procedure a linear background is subtracted from the spectra that are identified from the full 40 nm range of the spectrum (not shown).

By scanning along the waveguides and recording such spectra for every 300 nm, we acquire spectral scans as plotted in Fig. 4.4 for 1%-6% disorder and in Fig. 4.5 for 0%. In all the scans we observe similar peaks to the ones in

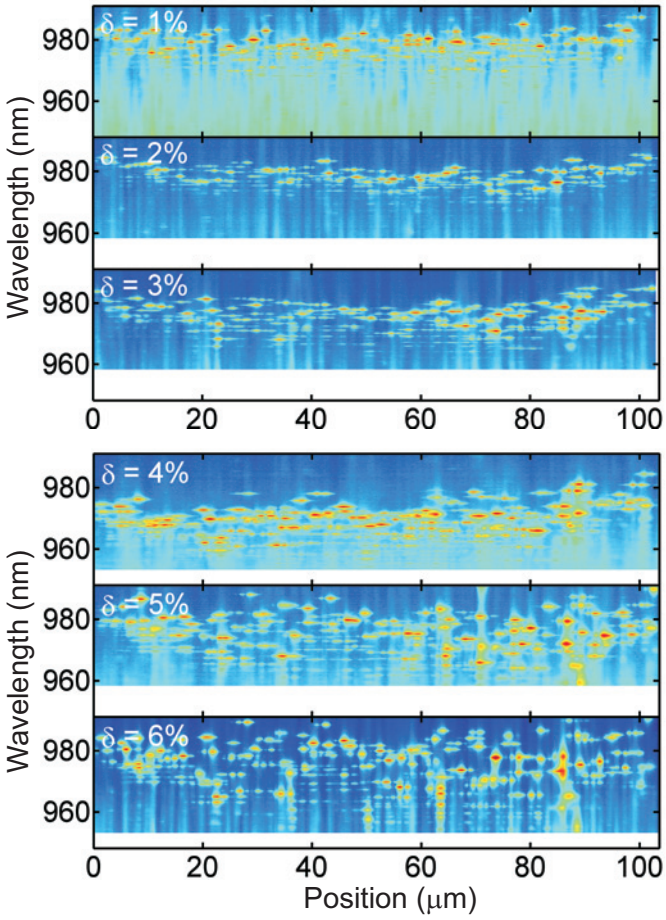

Figure 4.4: Position dependent photoluminescence spectra obtained along the full length of 6 disordered PhC waveguides with different amount of external disorder with a deviation in the hole position with a standard deviation between $1\% - 6\%$. All the axis limits have been set equal to be able to compare the spectral and spatial extend of the modes. The intensity axes are in arbitrary log scales from blue (low) to red (high) and are not comparable between the different plots

Fig. 4.2, that are randomly distributed throughout the whole waveguide and confined to a small spectral region around the band edge of the PhC waveguide. Similar measurements have been performed on samples with 9% and 12% disorder but only very broad features in the spectra have been observed suggesting that the localization length here is larger than the sample length. From scans perpendicular to the waveguide we can verify that the modes are indeed confined to the waveguide within the spatial resolution of the setup, which confirms the 1D nature of the system. Similar random resonances are identified in both the 2D model of disordered PhC waveguide in Sec. 3.2, in the 1D model (Sec. 3.3), and have previously been observed and characterized in transmission measurements [70, 69] and in full 3D simulations [58]. The measured intensity is a nontrivial combination of the far field of the mode profile, the Purcell factors at the emitter positions and, the out-of-plane scattering. Hence, the real speckle pattern is only obtainable with a near field probe. Since the excitation and collection occur at the same position, these scans do not contain information on the propagation of light that is often used to extract the localization length. Instead, we have an efficient method to excite the modes to probe their statistical properties, as shown in Fig. 4.4 and 4.5. The spectral range of the peaks display a finite size effect, especially for 0%, 2% and 3%, where the peaks shift towards longer wavelengths approximately $10 - 20$ μm from either end of the waveguide. We interpret this as the length scale at which the tails of the modes start to feel the sample edges, an indication of the scale of the localization length.

The spectral scans in Fig. 4.4 have been analyzed in order to extract the individual Anderson modes. An example of the identified modes is plotted with different colored circles in Fig. 4.5, where an automatic algorithm was used for consistency. The fitting procedure for the individual spectra is as explained previously. Peaks for the same speckle appear in nearby spectra because the step size, 0.3 μm, is smaller than the collection spot. From these, only the spectrum showing the highest intensity for the speckle is used for the statistics. Furthermore, the individual modes can consist of more than one speckle and the remaining peaks have been classified into different modes with the same wavelength and Q-factor within their uncertainties. The remaining analysis will be performed on the resulting sets of modes characterized by their Q-factors and wavelengths as a function of disorder.

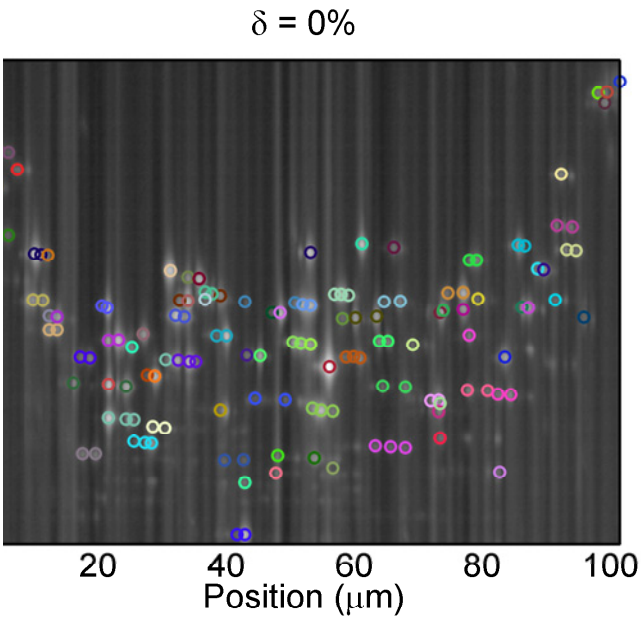

Figure 4.5: Photoluminescence scan along a 100 μm PhC waveguide sample with only fabrication induced disorder. Resonance peaks are still visible near the band edge of the PhC waveguide. The colored circles mark the identified peaks and circles with the same color are peaks that are assigned to the same Anderson localized modes identified as nearby speckles with the same Q-factors within the Q-factor uncertainty.

4.3.2 Mode Statistics as a Function of Disorder

In Fig. 4.6a we plot histograms of Q-factors for the different amounts of disorder, showing the number of modes in each bin. To see the details with enough significance we have used 12 bins regardless of the spread in the Q-factors. A common feature for all the histograms is a peak near the central region with tails extending out towards higher and lower values. As we decrease the amount of disorder we see an approximate linear trend in both the position of the peak maxima and the maximum Q-factors towards higher values and that the histograms spread out. The maximum Q-factor increases from around 4.000 for 6% disorder up to over 11.000 for 0%, with no induced disorder. The lowest Q-factors observed varies little across the different samples from around 500 -

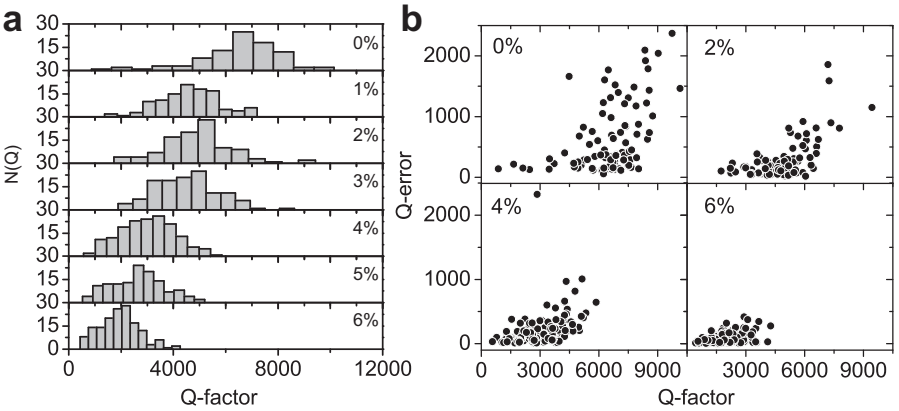

Figure 4.6: (a) Histograms of Q-factors for extracted from samples with 0% to 6% disorder (b) Q-factors and Q-factor uncertainties extracted from the fits for $\{0\%, 2\%, 4\%, 6\%\}$ disorder. The scale for the four panels is equal.

1500, with both 0% and 6% showing modes with Q-factors below 1000. This means that the histograms mainly stretch out towards higher values for lower amount of disorder. If we follow the trend for the peaks across the samples we see that the 1% sample show smaller Q-factors than even the 2% sample. To make sure this is accurate we have remeasured the spectral scans for different, but nearby, r/a values, which all display the same deviation from the linear trend. At this point, it is not clear if this is a real effect for 1% disorder or an artifact from the fabrication.

Examples showing all the fitted Q-factors along with their uncertainties are plotted in Fig. 4.6b for four of the samples. The relative uncertainties in the Q-factors from the fitting procedure cover an almost constant range between 0% and 25% for all the different amount of disorder. There is a slight increase towards higher uncertainties for larger Q-factors. This is expected as the highest Q-factors approach the spectral resolution of the spectrometer of 20.000. These high relative uncertainties are important to take into account for fitting the Q-factors to the 1D disorder model later in Sec. 4.4, as they relax the constraints on the model parameters.

Histograms of the observed wavelengths for the modes are plotted in Fig. 4.7, showing the spectral extend of the modes. Most notably is a clear increase in the wavelength range over which the modes occur for larger amounts of disor-

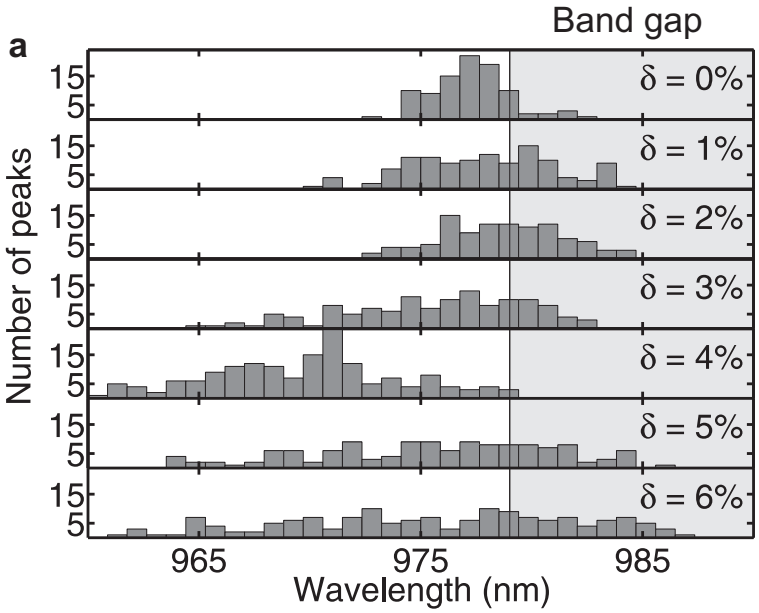

Figure 4.7: Histograms of the wavelengths of the Anderson localized modes in disordered PhC waveguides with different amounts of external disorder. The modes are mostly centered around the calculated band edge of 977 nm but are distributed over a larger range for increasing amount of disorder.

der. The distributions are all centered near the band edge position of 977 nm. The small differences from this value are due to variation in the hole size and effective lattice constant between the samples. It is therefore difficult to precisely extract the spectral position of the band edge of the ideal waveguide, which could be used to estimate how deep into the band gap that the Anderson localized modes extend.

The ensemble averaged statistics of the above results are plotted in Fig. 4.8 for the Q-factors and the spectral extend of the modes, defined as the difference between the maximum and minimum of the mode wavelengths. The average Q-factor and standard deviation are plotted as black dots and the spectral extend and the total number of modes with gray dots for each amount of disorder. Interestingly enough, all 4 parameters display an approximately linear dependence on disorder, where for 0% we observe both the largest average Q-factor

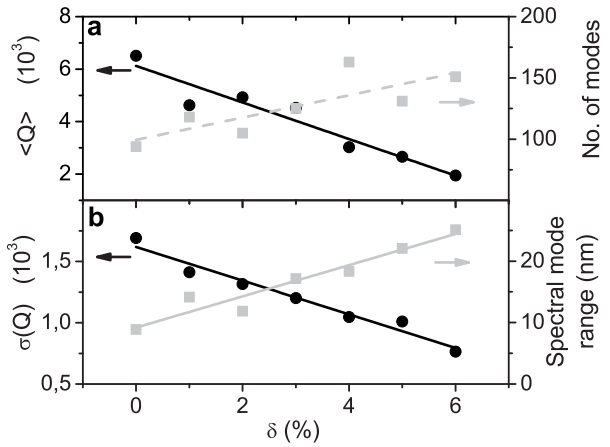

Figure 4.8: Statistics of the extracted Anderson localized modes as a function of induced disorder. With increasing disorder the average Q-factor goes down as well as the standard deviation, which is a signature of decreased localization length and increased losses. (a) The ensemble mean Q-factor $\langle Q \rangle$ and number of identified modes, with linear fits to both. (b) Standard deviation of the Q-factor ensemble and the spectral extend given by the difference between the maximum and minimum wavelength of the modes, also with linear fits.

and the largest standard deviation. We can compare the trends for the ensemble averaged Q-factors to the knowledge acquired from the simulation of the 1D model in Sec. 3.3 to obtain insight into the effect of disorder on PhC waveguides. Both the average and standard deviation of the Q-factors increases for smaller amount of disorder. This combination is a signature of either decreasing losses and/or smaller localization lengths. Smaller localization lengths increase the average Q-factor significantly whereas lower losses truncate the Q-factors at successively higher values. Without fitting the data it is not possible to separate the two causes. The fact that the spectral extend of the modes broadens with disorder shows that the transition to the Anderson localized regime occurs at successively lower group indices. The extra spectral range subsequently leaves room for an increased number of modes as also shown. The bandwidth of the region where the localized modes appear can therefore be used as an indirect method to determine the minimum group velocity at which the transition to the localized regime occurs. We do not observe any significant correlation

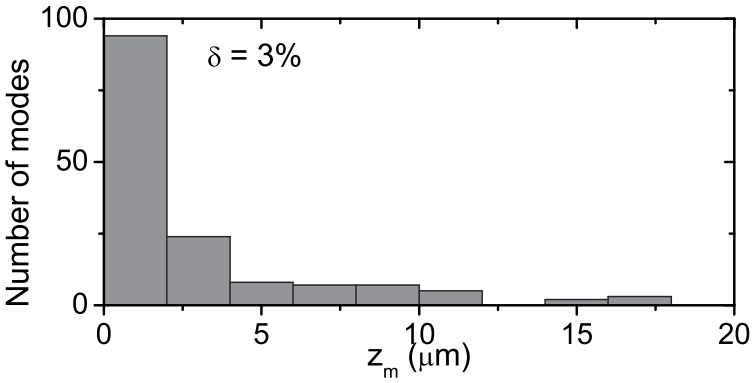

Figure 4.9: Histogram of the spatial extend of the modes for 3% induced disorder, calculated as the maximum distance between two speckles assigned to the same mode. All modes with only one speckle are in the first bin.

between the Q-factors and the mode wavelengths and therefore no dispersion in the Q-factors. This is consistent with the slow dispersion seen in the Anderson localized regime for passive waveguides in Ref. [44], but more statistics will be need to study the dispersive behavior in detail.

Analysis of Mode Sizes

To get a first estimate of the length scale over which the modes localize we extract the mode sizes as the distance between the two speckles farthest apart for each mode, shown as a histogram for 3% in Fig. 4.9. The first bin mostly covers modes with only a single speckle. We see that the majority of the modes only extend over less than 2 μm and the number of modes falls off exponentially with the mode length. This can not directly be related to the localization length, but it indicates that the length is on the order of a few micro meter. We note that the results are biased towards shorter lengths and the real mode size is therefore larger. The modes with the shortest lengths are correlated with higher peak intensity and the long modes are therefore more likely to have peaks below the minimum threshold that is used to identify peaks. However, compared to the 27 μm extinction length measurement in Ref. [44] on similar samples but without quantum dots this is rather surprising. Here the light was evanescently coupled into the disordered waveguide and the

light scattered out-of-plane was collected along the waveguide with an initial separation of 150 μm. The ensemble averaged intensity was then fitted to an exponential decay to extract the extinction length $1/l_e = 1/\xi + 1/l$, where the extinction length is a lower limit of ξ. The large initial separation might have preferentially selected modes with long extinction lengths or so-called necklace states where several localized modes couple to each other to form a chain [16].

4.4 Inference of Localization Length and Losses from Q-Factor Distributions

In the following we use Bayesian inference [71] (see Appendix A for short review) to extract the localization length ξ and information on the losses as a function of the amount of disorder by comparing the measured Q-factor distributions to the 1D disorder model described in Sec. 3.3. We use that the Q-factors without losses are described by log-normal distributions and that the log-normal parameters approximately show a power law dependence on the localization length (see Sec. 3.3.1). The losses are introduced through the redistributions of the Q-factors described in Sec. 3.3.1 by using a loss Q-factor. In this way we get a statistical model description that is completely analytical. This is a very simplified model of a disordered PhC waveguide and a real 3D coherent multiple scattering model would be needed to fully describe the system, thus any extracted values need to be treated with care. However, the model captures the main physical processes of 1D Anderson localized modes and provide an alternative method to the transmission measurement to extract information about the localization length and the losses of the system.

The analysis will be performed for three different variations of the model: Model 1 describes the ensemble averaged effect of the disorder by the localization length and includes a single loss Q-factor and can be evaluated analytically, Model 2 is identical to the first model but in addition, it takes into account the error bars on the individual Q-factors. Model 3 is a more realistic scenario that includes a distribution of losses but neglects the Q-factor errors to make it feasible to do the calculations. For reference, the extracted localization lengths and loss lengths for the three models are shown later in Fig. 4.12 on page 85.

The Bayesian theorem for the model with a single loss parameter is

$$P(\xi, Q_l|\{Q_i^m\}) = \frac{P(\xi, Q_l)P(\{Q_i^m\}|\xi, Q_l)}{P(\{Q_i^m\})} \tag{4.1}$$

where we want to infer the probability distribution of the localization length ξ and a single loss Q-factor Q_l, given a set of measured Q-factors, $\{Q_i^m\}$. The right side contains the prior probability of the two parameters ξ and Q_l, $P(\xi, Q_l)$, the total likelihood of all the measured Q-factors $\mathcal{L}\{Q_i^m\} = P(\{Q_i^m\}|\xi, Q_l)$ and finally the total probability of all the measured Q^m-factors $P(\{Q_i^m\})$, which just acts as a normalization and is not calculated. As both ξ and Q_l are independent scale parameters we use a Jaynes prior $P(\xi, Q_l) \propto 1/(\xi\, Q_l)$.

As the individual measurements are independent, the total likelihood is

$$P(\{Q_i^m\}|\xi, Q_l) = \prod_i^N P(Q_i^m|\xi, Q_l) \tag{4.2}$$

where the product runs over all the Q-factors and $P(Q_i^m|\xi, Q_l)$ is the likelihood for each Q-factor. Each measured Q-factor, Q_i^m, has associated an uncertainty. We can then write $Q_i^m = Q_i + e_i$ as a sum of the intrinsic but unknown Q-factor Q_i and the fit uncertainty e_i. Introducing Q_i and e_i as nuisance parameters and using the product rule for probabilities $P(A, B|C) = P(B|C)P(A|B, C)$ we get

$$\begin{aligned} P(Q_i^m|\xi, Q_l) &= \iint dQ_i de_i\, P(Q_i^m, Q_i, e_i|\xi, Q_l) \\ &= \iint dQ_i de_i\, P(Q_i|\xi, Q_l)P(e_i|\xi, Q_l)P(Q_i^m|Q_i, e_i, \xi, Q_l). \end{aligned} \tag{4.3}$$

The last term represents the probability of observing Q_i^m conditional on Q_i and e_i, which is defined through $Q_i^m = Q_i + e_i$, thus we have $P(Q_i^m|Q_i, e_i, \xi, Q_l) = \delta(Q_i^m - Q_i - e_i)$. Performing the integral over the delta function we get

$$P(Q_i^m|\xi, Q_l) = \int_0^\infty dQ_i P(Q_i|\xi, Q_l)P(Q_i^m - Q_i|\xi, Q_l), \tag{4.4}$$

which shows that $P(Q_i^m|\xi, Q_l)$ can be calculated as the convolution between the theoretical distribution Q_i given by Eq. (3.20)

$$P(Q_i|\xi, Q_l) = \frac{1}{\sqrt{2\pi}\sigma(\xi)} \exp\left[-\frac{\left(\mu(\xi) - \ln\left[\frac{QQ_l}{Q_l - Q}\right]\right)^2}{2\sigma(\xi)^2} \right] \frac{Q_l\theta(Q_l - Q)}{Q(Q_l - Q)} \tag{4.5}$$

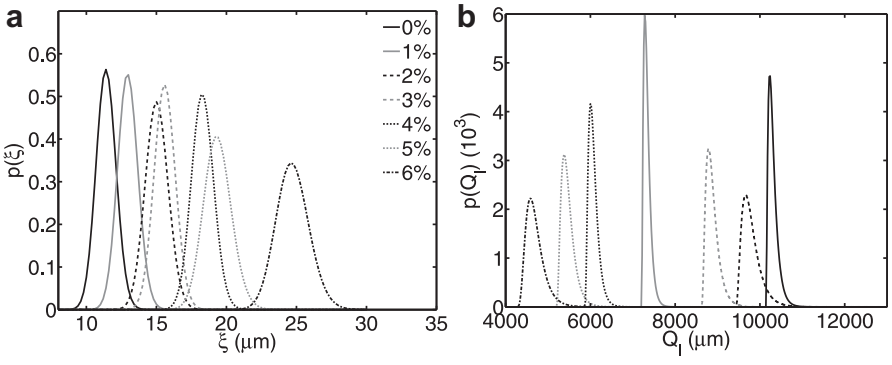

Figure 4.10: (a) Plot of $P(\xi|\{Q_i\})$ for different amount of disorder in a disordered PhC waveguide where the measured Q-factor distributions have been fitted to a model 1) with one loss parameter and extracted errors in the Q-factors have been neglected. (b) Plot of $P(Q_l|\{Q_i\})$ for the same model.

and the error probability distribution of the measured Q_i^m. For gaussian errors we have

$$P(Q_i^m - Q_i|\xi, Q_l) = \frac{1}{\sqrt{2\pi}\sigma(Q_i^m)} \mathrm{e}^{-\frac{(Q_i^m - Q_i)^2}{2\sigma(Q_i^m)}}. \tag{4.6}$$

The convolution between Eq. (4.5) and (4.6) has no analytical solution and has to be evaluated numerically. Inserting Eq. (4.4) back into Eq. (4.2) we see that the evaluation of $P(\xi, Q_l|\{Q_i^m\})$ thus contains the product of a numerical integral for each data point which is computationally intensive. We therefore first implement model 1, neglecting the measured errors in the Q-factors and let $P(Q_i^m - Q_i|\xi, Q_l) = \delta(Q_i^m - Q_i)$, which greatly simplifies the computations. Due to the products in Eq. (4.2) the values for the total probability are likely to become smaller than the minimum machine precision of 2.2251×10^{-308} for floating point operations so the model has been implement in Mathematica that allow for arbitrary-precision numbers. The analysis has been performed for the Q-factors acquired for the different amount of disorder shown in Sec. 4.3.2.

Results with One Loss Parameter

As an example for the results of Model 1 the posterior probability distribution for $P(\xi|\{Q_i^m\})$ and $P(Q_l|\{Q_i^m\})$ are shown in Fig. 4.10 for different amount of disorder. The localization lengths are to a good approximation normal dis-

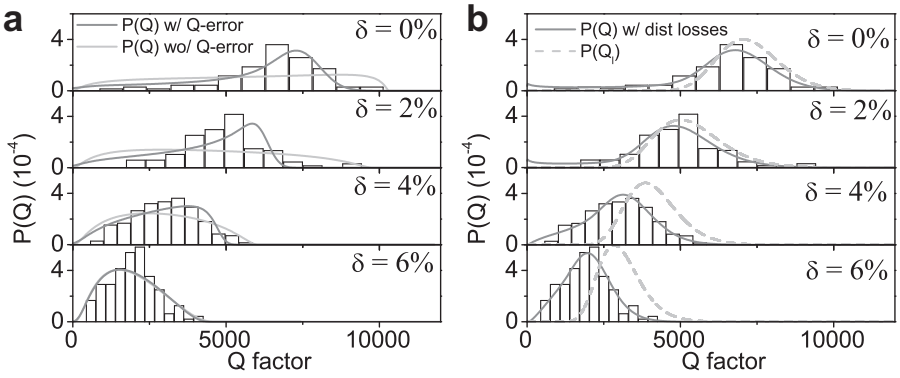

Figure 4.11: Q-factor histograms for Anderson modes in disordered PhC waveguides with external disorder induced by randomly moving the holes in the 6 rows nearest to the waveguide with a rms of $\delta = \{0, 0.02, 0.04, 0.06\}a$. (a) The solid lines represent the fitted single Q-factor probability distribution for the mean values of ξ and Q_l for a 1D disordered model with one loss parameter. The dark gray line include the errors in the Q-factor whereas the light gray line does not. (b) The solid line is fit to a 1D disordered model with a log-normal distribution for the loss Q-factor, Q_l, which show as the as the dashed line. The distribution are for the most likely values of ξ, μ_l and σ_l

tributed, which is a consequence of the central limit theorem. All localization lengths are between 10 μm and 25 μm, well below the sample length of 100 μm meaning that all the samples are in the localized regime, consistent with the fact that we do observe localized modes. The distributions for Q_l are all asymmetric with a sharp cut-off at the largest Q-factor in the measurements as a result of the heaviside function Eq. (4.5). This means that if a given Q-factor exists in the sample, the loss Q-factor can not be smaller than this value. The parameters in the model is therefore strongly restricted by the largest measured Q-factors. There is a clear trend for both shorter localization lengths and smaller amount of loss for less disorder, which will be discussed further in the final analysis of the three models.

In Fig. 4.11a (light gray line) we plot the best fit for the single Q-factor distributions where we use the average values of $\langle\xi\rangle$ and $\langle Q_l\rangle$ from Fig. 4.10 and insert in Eq. (4.4). We first observe that the fitted distributions exactly covers the full range of Q-factors, which means that the fitting procedure is

working correctly. However, the model describes the data poorly, especially for low amount of disorder, and predicts an almost flat distribution and does not correctly follow the variations in the histogram. This means the simple model is too restricted in that the single loss parameter Q_l is strictly limited to the highest Q-factor and the model is not able to adapt by varying the localization length to fit the data.

For Model 2, where the uncertainties in the Q-factors are included, agreement between the model and the data in Fig. 4.11a is greatly improved (dark gray). As show in Fig. 4.6 the highest Q-factors have the largest uncertainties, which allows the model to simultaneously decrease both Q_l and ξ as shown in Fig. 4.12 to better model the data. The lowest localization length has decreased to 7 μm at $\delta = 0\%$ but still increases monotonously to around 25 μm for $\delta = 6\%$.

4.4.1 Distribution of Losses in Photonic Crystal Waveguides

In a realistic model of a PhC waveguide, the individual localized modes scatter differently to the modes above the light line, and this leads to a distribution of losses $P(Q_l|\xi, \Theta_l)$ where Θ_l is a set of distribution parameters. There exists no theory for the explicit form of $P(Q_l|\xi, \Theta_l)$ in the case of PhC waveguides. By using any loss distribution that has enough freedom and predict positive Q-factors would suffice to show the effect of different losses disregarding the exact shape of the distribution. In a simple model, we can describe the radiation losses as an overlap between the exponential tails of the field profile leaking out of the membrane and a sum of all radiation modes [58]. If we assume a Gaussian distribution of the length of the exponential tails, we arrive at the same argument for choosing a log-normal distribution as for the in-plane Q-factors in Sec. 3.3 [64]. The radiation losses have been shown numerically to span approximately an order of magnitude and in Ref. [58] the losses appear to be normal distributed on a log scale, which suggest that a log-normal distribution is indeed a good approximation.

The distribution of losses can be included in the model in Sec. 4.4 by integrating over the loss Q-factor distribution for each Q-factor so Eq. (4.4) now

has the form

$$P(Q_i^m|\xi,\mu_l,\sigma_l) = \int_0^\infty \int_0^\infty dQ_i dQ_l\, P(Q_i|\xi,Q_l)P(Q_i^m - Q_i|\xi,Q_l)P(Q_l|\xi,\mu_l,\sigma_l) \tag{4.7}$$

where μ_l and σ_l are unknown loss distribution parameters for the log-normal distribution. Neglecting the uncertainties in the measured Q-factors and inserting a log-normal for the loss distribution we end up with

$$\begin{aligned} P(Q_i^m|\xi,\mu_l,\sigma_l) &= \int_0^\infty \int_0^\infty dQ_i dQ_l\, P(Q_i|\xi,Q_l)P(Q_l|\xi,\mu_l,\sigma_l)\delta(Q_i^m - Q_i) \\ &= \int_0^\infty dQ_l\, P(Q_i|\xi,Q_a)P(Q_l|\xi,\mu_l,\sigma_l) \end{aligned} \tag{4.8}$$

where

$$P(Q_l|\xi,\mu_l,\sigma_l) = \frac{1}{\sqrt{2\pi}Q_l\sigma_l}\exp\left[-\frac{(\mu_l - \ln Q_l)^2}{2\sigma_l^2}\right] \tag{4.9}$$

and $P(Q_i|\xi,Q_a)$ are given by Eq. (4.5).

Compared to the previous models, an extra degree of freedom is introduced as the log-normal have two free parameters, which allows for the model to better fit the data. Due to computational constrains in the calculation of $P(Q_i^m)$, a formal model comparison has not been performed to assess whether the extra free parameter is statistically justified. As argued above, the distribution of losses is more realistic and allows us to gain better insight into the interplay between the in- and out-of-plane scattering of the Anderson localized modes. The most likely distributions $P(Q_i^m|\hat{\xi},\hat{\mu}_l,\hat{\sigma}_l)$ are plotted in Fig. 4.11b together with the distributions of the losses $P(Q_l|\hat{\mu}_l,\hat{\sigma}_l)$. The extracted localization lengths for 0% to 4% are all around 3 μm, which is below the valid range of the model, as the power law for $\mu(\xi)$ has only been fitted for numerical simulations of the 1D model down to $\xi = 7$ μm. The real localization length would therefore be slightly larger.

This model fits the data very well compared to the two previously models for all the degrees of disorder, suggesting that the model is a better physical description. It is striking that the pure loss distributions span over such a large fraction of the whole Q-factor histogram. This means that the measured Q-factors mostly reflect the out-of-plane scattering. This view is supported by the short localization lengths extracted: the light is strongly confined in the PhC and the in-plane Q-factors are therefore very large (in the simulations

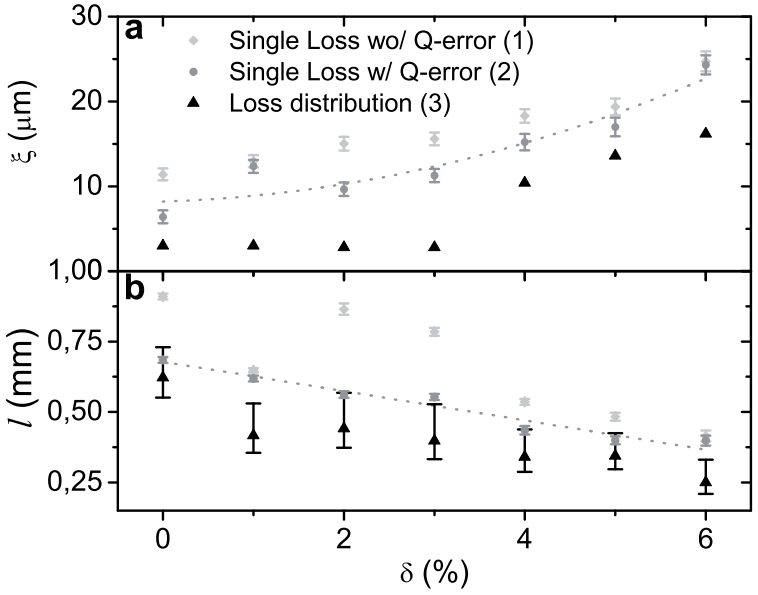

Figure 4.12: Summary of the results for the three models (1–3, see text) fitted to Q-factor distributions from disordered PhC waveguide with different amounts of disorder. The dotted lines are guides to the eye for model 2. (a) Mean localization length and standard deviation for model 1, 2 and most likely value for model 3. (b) Mean loss length and standard deviation for model 1 and 2. For model 3 the error bars cover the central 68.2% of the log-normal distribution and the triangles mark the most likely value.

larger than 10^7) and Q-factors are dominated by the out-of-plane scattering. The same mechanism dominates in designed PhC cavities, where the in-plane Q-factor scales exponentially with the size of the PhC and the effective Q-factor is limited by the $\boldsymbol{k}$-vectors components of the field distribution above the light line. In the measured Q-factor histograms, signatures of the localization length are therefore mainly present in the initial slopes.

4.4.2 Analysis of Extracted Localization Length and Losses as a Function of Disorder

All the results of the three models are summarized in Fig. 4.12, showing the extracted localization ξ and loss lengths, l. To be able to compare the localization length and losses directly we here use the loss length, l, instead of the loss Q-factor. We now discus the observed trends.

We first notice that all the extract values for the models fulfill the criterium $\xi \ll L \ll l$ for 1D Anderson localization in the presences of losses. In this regime the light undergoes several multiple scattering events inside the sample before being lost, and can form well-resolved resonances [72], which give the spectral signature of the localized modes that were observed in the experiment. This acts as a consistency check that the models predict the correct regime of light propagation.

For all the models shown here, the lowest localization length is achieved for the sample without disorder $\delta = 0\%$ and then increases for increasing amount of disorder. In model 2 the localization length increases from 7 μm at $\delta = 0\%$ to around 28 μm at $\delta = 6\%$ disorder. The increase of the localization length with disorder is at first sight counterintuitive, since in general increasing the amount of disorder leads to stronger multiple scattering and presumably better localization. However, in a moderately disordered PhC waveguide the localization length is inversely proportional to the ensemble-averaged density of states [73, 44]. The density of states at the band edge broadens with increasing amount of disorder and consequently the magnitude of the DOS is reduced. Since the transition to the localized regime occurs for $\xi < L$, this picture is consistent with the observation that the spectral range of Anderson-localized modes increases with disorder.

It is intriguing that the localization lengths for Model 3 present a constant value of a few micrometer for $\delta = 0\% - 3\%$. This indicates that we can confine the light on average to the same length scale as for designed L3 cavities, which is consistent with the very short extend we measure for the modes, as shown in Sec. 4.9, where a large number of the modes only cover a single speckle. The reason for the constant localization length is unclear. The most likely reason is that the loss distribution is so dominating that the model just predicts a very short ξ but does not have enough statistics to extract the correct value. One possible explanation is that the transition to localization occurs at the same

group index and the increased disorder just produces localized states deeper into the band gap of the PhC as the spectral range of the modes is broadening.

It is still an open question what the minimum localization lengths are in PhC waveguide and if a lower limit exist. In Ref. [58] a localization length on the order of the lattice constant was observed in simulations with 0.1% disorder and it has even been suggested that no fundamental lower boundary exists [14]. In periodic 3D structures the localization length is predicted to shown a parabolic dependence with a minimum localization length for a small amount of disorder [74]. In the 1D PhC waveguides a similar behavior is expected as in the limit of no disorder the mean free path and localization length is infinity. Adding a small amount of disorder quickly reduces the localization length and later increases it for larger amounts of disorder. However, this minimum has not yet been verified in simulations or experimentally and it appears that lower amounts of disorder than the best fabricated sample are needed to observe this minimum.

The loss length decreases as a function of disorder from around $l = 750$ μm down to $l = 300$ μm. As the hole wall inclination is assumed to not increase with disorder in the lattice constant, the increased losses are therefore directly related to enhanced in-plane scattering into more lossy modes. The upper error bar of model 3 almost coincide with the values for model 2 indicating that this model correctly captures the lowest amount of losses from the Q-factors but misses the correct distribution. In the literature the loss rate/coeffecient has been shown to increase quadratically with the amount of disorder in the ballistic regime due to Rayleigh scattering [75, 58]. In Ref. [58] this relation is seen to transfer to the mode of the loss distribution, but this can not be directly confirmed with enough statistically significance with the available data.

We can now compare the extracted localization lengths and loss lengths to the data in Chapter 3.4.6 to estimate the probability of observing a strongly coupled system between a quantum dot and an Anderson localized mode. As already mentioned the best candidate is for the sample with 0% disorder with a estimated localization length of $3 - 7$ μm and a most likely loss length 600 μm. The closest simulated values is for $\xi = 7$ μm and $l = 700$ μm, which gives a strong coupling probability of less than 1%. However, for samples with smaller amount of losses and with the already extracted localization length, which should be possible according to the estimates in Chapter 3.4.6, the observation

of strong coupling in Anderson localized modes should be within reach.

4.5 Cavity QED with Anderson Localized Modes

In Sec. 3.4 we described the possibility of studying cavity QED effects in the Anderson localized regime to enhance the light matter coupling and ultimately to reach the strong coupling regime. In this section we demonstrate that it is indeed possible to enhance the light matter coupling by coupling individual quantum dots to a single random Anderson localized mode [46]. This leads the way to a better understanding of the light matter coupling in disordered material with embedded emitters. Extending the current demonstration is important to obtain statistics on the fluctuations in the LDOS.

The important figure of merit for cavity QED in the weak coupling regime is the Purcell factor [76]

$$F_p = \Gamma_c/\Gamma_{\text{hom}} = \frac{3(\lambda/n)^3 Q}{4\pi^2 V_m}, \tag{4.10}$$

where Γ_c is the decay rate into the cavity mode and Γ_{hom} is the decay rate into a homogenous medium. A smaller mode volume V_m enhances the maximum achievable electric field in the mode and the Q-factor determines the photon storage time in the cavity and thereby the interaction time. From the previous section we can estimate the achievable mode volumes and Q-factors. A large part of the experimental modes only consist of a single speckle. With the effective area used in Sec. 3.4.6 of $A_{\text{eff}} = 0.0356\ \mu\text{m}^2$ and the single speckle mode length of 1.4 μm gives an upper limit of the mode volume of $\sim 2(\lambda/n)^3$ for the smallest observed modes. This is comparable to the best designed high-Q cavities. Another estimate can be drawn from the simulation for the mode volume in Sec. 3.4.4; although the simulated results do not extend down to the smallest estimate of $\xi = 3 - 7$ μm, extrapolating them leads to comparable small mode volumes. The observed Q-factors analyzed in the previous section are competitive to Q-factors obtained for modes in highly optimized cavities [25] although higher Q-factors up to 30.000 are found in samples with lower quantum dot densities[3, 77]. In our own samples with optimally designed L3 cavities [78] using the same wafer and fabrication technique we have measured Q-factors between 6.000–10.000. An advantage of the spontaneously forming Anderson localized modes is their inherently robustness towards disorder, which

shows the great potential in utilizing Anderson localized modes. With the high Q-factors observed for the Anderson localized modes (up to 11.000) and the strong indications of very small mode volumes the Anderson localized modes offer a promising system for cavity QED experiments.

Pumping the sample at a low-excitation power below the saturation of the quantum dot ground state, allows us to resolve single quantum dot lines and therefore to enter the regime of cavity QED. In this experiment we used a pump power density of 20 W/cm^2 at a wavelength of 850 nm corresponding to pumping the wetting layer. The Ti:sapphire laser was operated in pulsed mode with repetition rate of 76 MHz and a pulse length of 2 ps. The photoluminescence signal was send to a spectrometer with a resolution of 0.15 nm and finally detected on a APD with a time resolution of 50 ps. The Purcell enhancement is studied by means of time-resolved photoluminescence spectroscopy, where arrival time histograms are collected after repeatedly exciting a quantum dot. Spectra were obtained by measuring the count rate on the APD while scanning the spectrometer grating. The 3% disorder version of the samples described in Sec. 4.2 was used for these experiments. For the samples with lower amounts of disorder and higher Q-factors, the intensity of the quantum dot lines near the cavity mode were suppressed. This is likely due to redistribution of the quantum dot far field emission near the cavity mode frequency.

Figure 4.13a shows an example of a photoluminescence spectrum displaying single quantum dot peaks labeled (QD1–5) and Anderson localized modes (C1-3). The Anderson localized mode (C1) has a Q-factor of 4200, extracted from the high power spectrum (Fig. 4.14b). In the low-excitation power spectra quantum dots and cavity peaks can easily be distinguished from their different temperature dependencies (Fig. 4.13b). This also enables the spectral tuning of single quantum dots into resonance with an Anderson localized mode. Figure 4.13c displays the crossing between a quantum dot and an Anderson localized cavity. No anti crossing is visible, demonstrating that the cavity-quantum dot system is in the Purcell regime where the cavity promotion of vacuum fluctuations enhances the quantum dot decay rate. Two examples of decay curves for the quantum dot tuned on- and off-resonance with an Anderson-localized cavity are presented in Fig. 4.14a. The decay curves are fitted with a multi-exponential decay, that is convoluted with the instrument response, where the fastest component mainly contains contributions from the radiative decay. Up

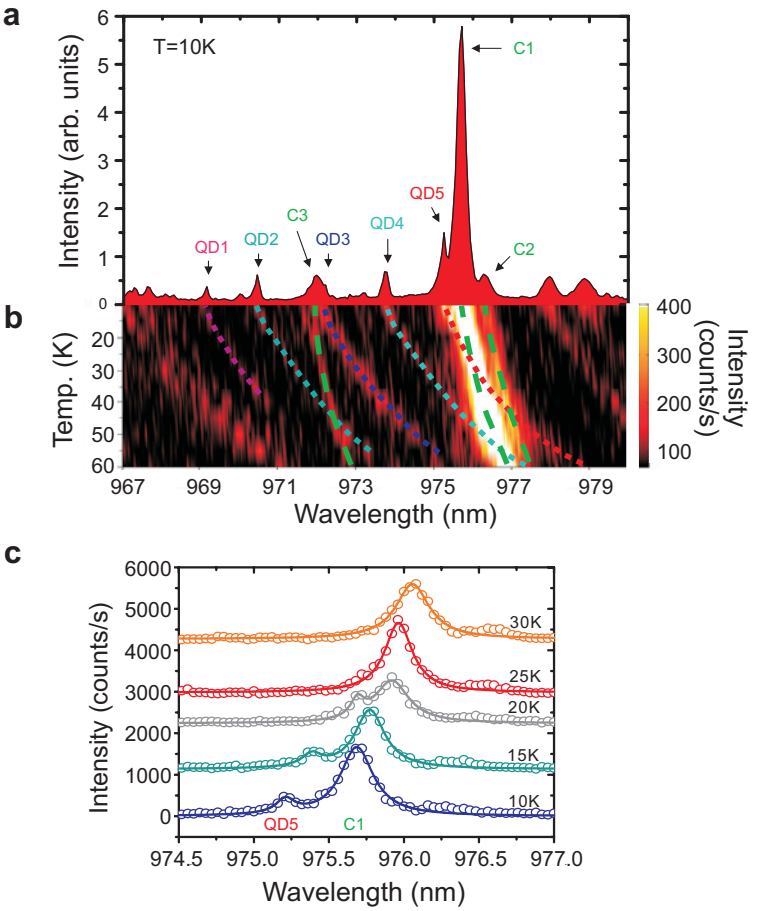

Figure 4.13: Temperature tuning of a single quantum dot into resonance with Anderson-localized cavities. (A) Low-power photoluminescence spectrum of a sample with 3% disorder at 10 K. (B) Photoluminescence spectra collected while varying the sample temperature in steps of 5 K. The dotted (dashed) lines are guides to the eye of the wavelength displacement of selected quantum dot emission (localized mode) lines. (C) Enlargement of the spectra displaying the quantum dots-cavity crossing. The spectra are fitted to two Lorentzians (solid lines) representing the quantum dot and the cavity peak

to three exponentials were used to account for coupling to dark states in the quantum dot and background contribution from other dots. Off- resonance, the quantum dot decay rate is inhibited due to the two-dimensional photonic band gap, leading to an emission rate of $\Gamma_\Delta = 0.5\ \mathrm{ns}^{-1}$ at a detuning off $\Delta = 1.4$ nm. A pronounced enhancement by a factor of 15 is observed on resonance where a fast decay rate of $\Gamma_{\Delta=0} = 7.9\ \mathrm{ns}^{-1}$ is extracted. An important figure-of-merit for, e.g., single-photon sources and nano-lasers is the β factor

$$\beta = \frac{\Gamma_c}{\Gamma_c + \gamma_{\mathrm{rad}} + \Gamma_{\mathrm{nrad}}} = \frac{\Gamma_{\Delta=0} - \Gamma_\Delta}{\Gamma_{\Delta=0}}, \tag{4.11}$$

which expresses the fraction of photons emitted into the cavity mode relative to the total emission rate. By comparing the emission rates on- and off-resonance, we extract $\beta = 94\%$. It represents a lower bound because even for large detuning, residual coupling to the waveguide can persist, increasing Γ_Δ. This high β-factor is comparable with the results obtained in standard PhC nano-cavities with carefully optimized cavity design and quantum dot density. The decay rates of two individual quantum dots being tuned across an Anderson-localized cavity are plotted in Fig. 4.14b. Different enhancement factors (15 and 9 at temperature $T = 25$ and 55 K, respectively) are observed on resonance due to the different positions and dipole orientations of the quantum dots that influence their coupling to the cavity mode. The presence of an additional Anderson localized cavity gives rise to the asymmetric detuning dependence of the decay rate.

Assuming a perfect spatial match between the quantum dot and the cavity mode, we can extract an upper bound on the mode volume of the Anderson-localized cavity of $V \sim 1\ \mu\mathrm{m}^3 = 44(\lambda/n)^3$ from the observed rate on resonance using Eq. (4.10) and a homogeneous decay rate of $1.1\ \mathrm{ns}^{-1}$. Using the calculated effective area we derive a mode length of 28 μm for cavity C1. This is longer than the estimated localization length and the mode length extracted in Sec. 4.9 of $3 - 10$ μm.

Figure Fig. 4.14b shows that Purcell enhancement is observed mainly within the cavity linewidth, which is opposed to the surprisingly far-reaching coupling reported for standard PhC cavities under non-resonant excitation [79]. Consequently, the extracted quantum dot decay rates are sensitive probes of the LDOS of the disordered PhC waveguides. Photon emission in disordered photonic structures was predicted to lead to a new class of infinite-range correla-

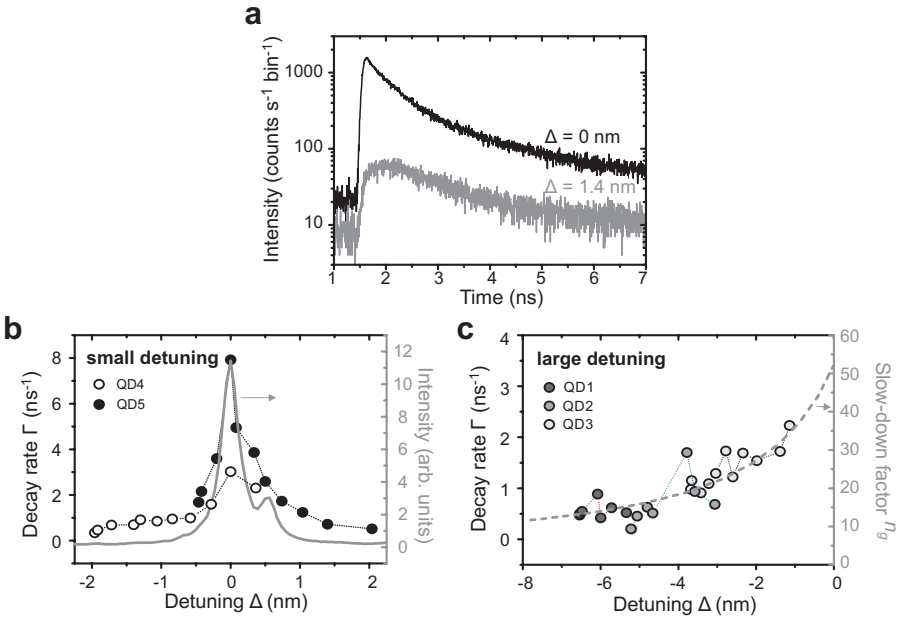

Figure 4.14: Detuning dependence of single quantum dot decay rates. (a) Decay curves of QD5 for two values of the detuning Δ relative to the localized mode C1. (b) Decay rates of QD4 and QD5 versus detuning and cavity emission spectrum. (c) Decay rates of QD1, QD2 and, QD3 versus detuning. The dashed line is the calculated slow-down factor for the unperturbed PhC waveguide. The enhancement at $\Delta = -4$ nm stems from the coupling of QD2 to a weak Anderson-localized cavity mode (C3 in Fig. 3A).

tions manifested as fluctuations in the decay rate of embedded emitters. Thus, the Purcell enhancement stems from the local enhancement of the photonic density of states in the Anderson localized regime that promotes spontaneous emission of photons.

Quantum dots detuned from Anderson-localized cavities may couple to the slowly propagating mode of the PhC waveguide. In this case, the quantum dot decay rate is expected to scale proportional to the group velocity slow-down factor n_g as discussed in Chapter 2. This behavior is observed for three different quantum dots at large detunings Δ from the dominating Anderson-localized cavity mode (Fig. 4.14c). This means that here the radiative coupling

is well described by the local photonic density of states of the unperturbed PhC waveguide even though they are still within the spectral range of the Anderson localized regime. This interesting coexistence of ordered and disordered properties occurs because relatively few periods of the PhC lattice are required to build up the local environment determining the quantum dot decay rate. Thus, the length scale on which the local photonic density of states builds up is mostly shorter than the localization length, which accounts for the success of PhCs despite ubiquitous disorder for, e.g., nano-cavities, single-photon sources, or spontaneous emission control.

4.6 Conclusion

In this chapter we have experimentally demonstrated that disorder in PhC waveguides is an efficient way to strongly localize light on length and time scales that are competitive to highly engineered cavity structure. In PhC waveguides with varying amount of artificial induced disorder we have observed localized modes with Q-factors up to 11.000 and mode length below the spatial resolution of 1.4 μm. Using embedded quantum dots as internal light sources have been show to be an efficient method to excite all the localized modes in disordered waveguide. The Anderson localized modes only appear at the band edge of the waveguides and the average Q-factors decrease with increasing amount of disorder. From the ensemble averaged statistics on the measured Q-factors we have extracted the localization length and losses length as a function of the amount of disorder in the PhC using a Bayesian fitting method. Localization lengths below 10 μm are extracted for sample with only fabrication disorder. As the amount of disorder increases, an increase in both the localization length and the losses are observed. The increased localization length is interpreted as the a result of the broadening of the ensemble averaged density of states at the waveguide band edge. We further more conclude that the losses are distributed as well, which add to the complectly of the description of disordered PhC waveguide. We can reach the regime of cavity QED by tuning single quantum dot emitters though a single Anderson localized mode. We observe a enhanced spontaneous emission rate of 15 and a β-factor of 94%. Our results demonstrate that distributed photonic disorder provides a powerful way of enhancing the interaction between light and matter, enabling cavity QED.

Chapter 5

Conclusion

This thesis has been focused on studying quantum electrodynamics (QED) effects in photonic crystal (PhC) waveguides, and to investigate the effects of disorder in PhC waveguide especially near the slow light regime. In the ideal model the density of states diverges near the band edge of PhC waveguides. However, we have shown that this divergence is resolved as a result of both losses and, most notable, through multiple scattering resulting in the formation of Anderson localized modes for low group velocities. The effects of multiple scattering can therefore not be neglected when treating propagation in slow light waveguides. Both the measured Q-factors and extracted mode volumes of the localized modes are found to be similar to those of state of the art engineered cavities. We have also shown that it is possible to utilize the disorder induced Anderson localized modes as a resource in cavity QED experiments.

We report on the first experiments where single quantum dots are coupled to a PhC waveguide mode. From decay rate measurements can we directly measure the coupling strength to the waveguide, which is seen to be enhanced in the slow light regime. The density of states has been mapped out over a broadband frequency range using a statistical ensemble of single quantum dots. The extracted dispersion of the local density of states (LDOS) matches the theory for a PhC waveguide. After tuning the emission lines of a set of single quantum dots through the waveguide band edge, a limit of the density of states is observed, either as a result of losses or/and localization and a β-factor of more than 85% for a single quantum dot is extracted.

Statistical information on the Anderson localized modes in PhC waveguides with intentional added disorder has been measured. Analyzing photoluminescence from an ensemble of embedded quantum dots has been show to be an efficient way of exciting all the Anderson localized mode. We find a broad distribution of Q-factors that depends strongly on the induced amount of disorder. The highest Q-factors are present in the PhC waveguide with only fabrication disorder. Comparing the extracted Q-factor distributions to the distributions obtained in a one-dimensional model, we have extracted the localization length and loss length as function of disorder. It is found that the localization length is shortest for samples with no intentional disorder, and then increase for larger amounts of disorder. This is the opposite of completely disordered systems and the difference is attributed to the modified density of state of the PhC waveguide that still exist even in the presence of a small amount of disorder. Losses are shown to dominate the measured Q-factor distributions and and the losses themselves present a distribution, which complicate the description of disordered PhC waveguides. From the theoretical model, the distributions of coupling parameters between a quantum dot and the distributions of Anderson localized modes have been extracted, from which we get the strong coupling probability. It is found that in realistic achievable structures a strong coupling probability of 10–20% is obtainable, whereas in the studied samples the probability is below 1%.

Finally, for the first time we report on a QED experiment in the Anderson localized regime where a set of quantum dot line has been tuned through an single localized modes in a PhC waveguide with 3% intentional disorder. A spontaneous emission enhancement factor of 15 is found for a single quantum dot and a β-factor of 94% is extracted on resonance.

Appendices

Appendix A

Bayesian Parameter Inference

First we shortly introduce the basic of Bayesian inference [71] that will be used for estimating the parameters describing the Q-factor distributions. This method is complementary to traditional fitting methods (e.g. least square fitting, most likelihood estimators) in estimating parameters from a model giving a set of data. The Bayesian method allows for arbitrary distributions to describe the data and the result comes as a full probability distribution. The method explicitly include any prior information about the parameters that is available before the analysis. In contrast, traditional fitting procedures only give a most likely parameter estimate and often make implicate assumption that the data are normal distributed. However, the added benefits of the Bayesian method often come at a high cost in computation time.

The basic equation is the Bayesian theorem

$$P(\{\theta_i\}|D,M,I) = \frac{P(\{\theta_i\}|M,I)P(D|\{\theta_i\},M,I)}{P(D|M,I)} \tag{A.1}$$

which relates the resulting joined posterior probability $P(\{\theta_i\}|D,M,I)$ for the set of model parameters $\{\theta_i\}$ to the likelihood $P(D|\{\theta_i\},M,I)$ of the data D given these parameters and the prior probability distribution of the parameters $P(\{\theta_i\}|M,I)$. It is important to keep in mind that the probabilities in Eq. (A.1) are all conditional on the chosen model M and the initial information I, otherwise the obtained uncertainties in the parameters are misleading.

For example the parameter uncertainties can be very small if the model poorly describes the data but still are able to approach the data for a narrow interval of the parameters. This is the reason that it is desirable to compare multiple models, unless the relative prior probability for a particular model is very high. The $P(D|M,I)$ is the total probability of the data conditional on the chosen model M. Its magnitude is only used if multiple competing models are to be evaluated against each other. For this purpose the Bayesian theorem can be written for the posterior probability $P(M_i|D,M,I)$ where M_i is a set of models. An advantage of the Bayesian approach is that by comparing $P(M_i|D,M,I)$ for different models to judge which one best describes the data automatically includes a Occam's razer effect that make models with fewer parameters more probable.

The fact that Eq. (A.1) contains the prior probability distribution has lead to some controversy over the usefulness of the approach when limited information is available prior to the analysis. This has head to the study of uninformed priors that strive to be objective, although only in very limited cases is it possible to prove the objectivity. The most used are the uniform prior $P(\theta_i) \propto k$ and Jaynes prior $P(\theta_i) \propto 1/\theta_i$. Both are improper priers in that they are only normalized over a given interval. Although, the uniform prier at first appear to contain the least information as it assign an equal probability to each unit length it is not scale/unit invariant. The Jaynes prior is scale/unit invariant and assign equal probability to each decade and is often used for scale parameters, ie. parameters that measure a size and have values somewhere in the interval between 0 and ∞. As more data is in included in the analysis the effect on the used prior distribution is reduced as long as the extracted values is in the prier interval and exact choice of prior is not important. If, however, information about a given set of parameters is available e.g. a gaussian probability from a least square fit it is now possible to include this in the further analysis to refine the parameter estimates, leading to a recursive use of Eq. (A.1). In fact, for independent measurements, the recursive use of Eq. (A.1) for each data point or using the likelihood for the combined dataset $P(D|\{\theta_i\},M,I) = \prod_i P(D_i|\{\theta_i\},M,I)$ is seen to be equivalent.

In most cases we are only interested in the probability distribution for a subset of the model parameters and in this case we can marginalize the nuisance parameters by integrating the joined probability distribution over these

parameters, which for one interesting parameter is

$$P(\phi|D,M,I) = \int \cdots \int d\{\tilde{\theta}_i\}\, P(\phi, \{\tilde{\theta}_i\}|D,M,I) \tag{A.2}$$

and in the same way we can calculate the normalization $P(D|M_i,I)$ by integrating over all model parameters. From the probability distributions we can then extract the mean $\langle\phi\rangle$, standard deviation $\sigma(\phi) = \sqrt{\langle\phi^2\rangle - \langle\phi\rangle^2}$ and most likely values $\hat{\phi} = \max_\phi\{P(\phi|D,M,I)\}$ for the interesting parameters where

$$\langle\phi^n\rangle = \int d\phi\, \phi^n P(\phi|D,M,I). \tag{A.3}$$

Bibliography

[1] J. Raimond, M. Brune and S. Haroche. *Manipulating quantum entanglement with atoms and photons in a cavity.* Reviews of Modern Physics **73**, 565 (2001).

[2] H. Haffner, C. Roos and R. Blatt. *Quantum computing with trapped ions.* Physics Reports **469**, 155 (2008).

[3] K. Hennessy, A. Badolato, M. Winger, D. Gerace, M. Atatüre *et al. Quantum nature of a strongly coupled single quantum dot-cavity system.* Nature **445**, 896 (2007).

[4] I. Fushman, D. Englund, A. Faraon, N. Stoltz, P. Petroff *et al. Controlled phase shifts with a single quantum dot.* Science **320**, 769 (2008).

[5] K. Srinivasan and O. Painter. *Linear and nonlinear optical spectroscopy of a strongly coupled microdisk-quantum dot system.* Nature **450**, 862 (2007).

[6] H. J. Kimble. *The quantum internet.* Nature **453**, 1023 (2008).

[7] P. Yao, V. Manga Rao and S. Hughes. *On-chip single photon sources using planar photonic crystals and single quantum dots.* Laser & Photonics Reviews **4**, 499 (2009).

[8] D. Kleppner. *Inhibited Spontaneous Emission.* Physical Review Letters **47**, 233 (1981).

[9] G. Lecamp, P. Lalanne and J. Hugonin. *Very Large Spontaneous-Emission β Factors in Photonic-Crystal Waveguides.* Physical Review Letters **99**, 023902 (2007).

[10] V. Manga Rao and S. Hughes. *Single quantum-dot Purcell factor and β factor in a photonic crystal waveguide.* Physical Review B **75**, 205437 (2007).

[11] T. Baba. *Slow light in photonic crystals.* Nature Photonics **2**, 465 (2008).

[12] Ping Sheng. *Introduction to wave scattering, localization and mesoscopic phenomena* (Academic Press, 1995).

[13] P. Anderson. *Absence of Diffusion in Certain Random Lattices.* Physical Review **109**, 1492 (1958).

[14] A. Lagendijk, B. van Tiggelen and D. S. Wiersma. *Fifty years of Anderson localization.* Physics Today **62**, 24 (2009).

[15] A. Chabanov, M. Stoytchev and A. Genack. *Statistical signatures of photon localization.* Nature **404**, 850 (2000).

[16] J. Bertolotti, S. Gottardo, D. Wiersma, M. Ghulinyan and L. Pavesi. *Optical Necklace States in Anderson Localized 1D Systems.* Physical Review Letters **94**, 113903 (2005).

[17] J. Billy, V. Josse, Z. Zuo, A. Bernard, B. Hambrecht *et al. Direct observation of Anderson localization of matter waves in a controlled disorder.* Nature **453**, 891 (2008).

[18] H. Hu, A. Strybulevych, J. H. Page, S. E. Skipetrov and B. A. van Tiggelen. *Localization of ultrasound in a three-dimensional elastic network.* Nature Physics **4**, 945 (2008).

[19] B. Corcoran, C. Monat, C. Grillet, D. J. Moss, B. J. Eggleton *et al. Green light emission in silicon through slow-light enhanced third-harmonic generation in photonic-crystal waveguides.* Nature Photonics **3**, 206 (2009).

[20] R. C. Somers, M. G. Bawendi and D. G. Nocera. *CdSe nanocrystal based chem-/bio- sensors.* Chemical Society reviews **36**, 579 (2007).

[21] J. Joannopoulos, S. G. Johnson, J. N. Winn and R. D. Meade. *Photonic crystals: molding the flow of light* (Princton University Press, 2008).

[22] M. Soljacić and J. D. Joannopoulos. *Enhancement of nonlinear effects using photonic crystals.* Nature materials **3**, 211 (2004).

[23] S. G. Johnson, M. L. Povinelli, M. Soljačić, a. Karalis, S. Jacobs *et al. Roughness losses and volume-current methods in photonic-crystal waveguides.* Applied Physics B **81**, 283 (2005).

[24] S. Johnson and J. Joannopoulos. *Block-iterative frequency-domain methods for Maxwell's equations in a planewave basis.* Optics Express **8**, 173 (2001).

[25] D. Englund, D. Fattal, E. Waks, G. Solomon, B. Zhang *et al. Controlling the Spontaneous Emission Rate of Single Quantum Dots in a Two-Dimensional Photonic Crystal.* Physical Review Letters **95**, 013904 (2005).

[26] P. Lodahl, A. Floris van Driel, I. S. Nikolaev, A. Irman, K. Overgaag *et al. Controlling the dynamics of spontaneous emission from quantum dots by photonic crystals.* Nature **430**, 654 (2004).

[27] A. F. Koenderink, M. Kafesaki, C. M. Soukoulis and V. Sandoghdar. *Spontaneous emission rates of dipoles in photonic crystal membranes.* J. Opt. Soc. Am. B **23**, 1196 (2006).

[28] J. Johansen, S. Stobbe, I. S. Nikolaev, T. L. Hansen, P. T. Kristensen *et al. Size dependence of the wavefunction of self-assembled InAs quantum dots from time-resolved optical measurements.* Physical Review B **77**, 073303 (2008).

[29] M. L. Andersen, S. r. Stobbe, A. S. n. Sø rensen and P. Lodahl. *Strongly modified plasmon–matter interaction with mesoscopic quantum emitters.* Nature Physics **7**, 215 (2010).

[30] J. Claudon, J. Bleuse, N. S. Malik, M. Bazin, P. Jaffrennou *et al. A highly efficient single-photon source based on a quantum dot in a photonic nanowire.* Nature Photonics **4**, 174 (2010).

[31] A. S. Bracker, D. Gammon and V. L. Korenev. *Fine structure and optical pumping of spins in individual semiconductor quantum dots.* Semiconductor Science and Technology **23**, 114004 (2008).

[32] A. J. Ramsay. *A review of the coherent optical control of the exciton and spin states of semiconductor quantum dots.* Semiconductor Science and Technology **25**, 103001 (2010).

[33] T. Lund-Hansen, S. Stobbe, B. Julsgaard, H. Thyrrestrup, T. Sünner *et al. Experimental Realization of Highly Efficient Broadband Coupling of Single Quantum Dots to a Photonic Crystal Waveguide.* Physical Review Letters **101**, 113903 (2008).

[34] H. Thyrrestrup, L. Sapienza and P. Lodahl. *Extraction of the β-factor for single quantum dots coupled to a photonic crystal waveguide.* Applied Physics Letters **96**, 231106 (2010).

[35] A. Kress, F. Hofbauer, N. Reinelt, M. Kaniber, H. J. Krenner *et al. Manipulation of the spontaneous emission dynamics of quantum dots in two-dimensional photonic crystals.* Physical Review B **71**, 241304 (2005).

[36] M. Bayer and A. Forchel. *Temperature dependence of the exciton homogeneous linewidth in In0.60Ga0.40As/GaAs self-assembled quantum dots.* Physical Review B **65**, 041308 (2002).

[37] J. Johansen, B. Julsgaard, S. Stobbe, J. M. Hvam and P. Lodahl. *Probing long-lived dark excitons in self-assembled quantum dots.* Physical Review B **81**, 081304 (2010).

[38] A. Laucht, F. Hofbauer, N. Hauke, J. Angele, S. Stobbe *et al. Electrical control of spontaneous emission and strong coupling for a single quantum dot.* New Journal of Physics **11**, 023034 (2009).

[39] S. Mosor, J. Hendrickson, B. C. Richards, J. Sweet, G. Khitrova *et al. Scanning a photonic crystal slab nanocavity by condensation of xenon.* Applied Physics Letters **87**, 141105 (2005).

[40] J. Pedersen, S. Xiao and N. Mortensen. *Limits of slow light in photonic crystals.* Physical Review B **78**, 153101 (2008).

[41] S. Hughes, L. Ramunno, J. Young and J. Sipe. *Extrinsic Optical Scattering Loss in Photonic Crystal Waveguides: Role of Fabrication Disorder and Photon Group Velocity.* Physical Review Letters **94**, 033903 (2005).

[42] S. John. *Strong localization of photons in certain disordered dielectric superlattices.* Physical Review Letters **58**, 2486 (1987).

[43] J. Topolancik, B. Ilic and F. Vollmer. *Experimental Observation of Strong Photon Localization in Disordered Photonic Crystal Waveguides.* Physical Review Letters **99**, 253901 (2007).

[44] P. García, S. Smolka, S. Stobbe and P. Lodahl. *Density of states controls Anderson localization in disordered photonic crystal waveguides.* Physical Review B **82**, 165103 (2010).

[45] J. Topolancik, F. Vollmer, R. Ilic and M. Crescimanno. *Out-of-plane scattering from vertically asymmetric photonic crystal slab waveguides with in-plane disorder.* Optics Express **17**, 12470 (2009).

[46] L. Sapienza, H. Thyrrestrup, S. Stobbe, P. D. Garcia, S. Smolka *et al. Cavity quantum electrodynamics with Anderson-localized modes.* Science **327**, 1352 (2010).

[47] A. Z. Genack and A. A. Chabanov. *Signatures of photon localization.* Journal of Physics A: Mathematical and General **38**, 10465 (2005).

[48] L. Deych, A. Yamilov and A. Lisyansky. *Scaling in one-dimensional localized absorbing systems.* Physical Review B **64**, 024201 (2001).

[49] L. Deych, a. Lisyansky and B. Altshuler. *Single-parameter scaling in one-dimensional Anderson localization: Exact analytical solution.* Physical Review B **64**, 1 (2001).

[50] L. A. Coldren and S. W. Corzine. *Diode Lasers and Photonic Integrated Circuits* (Wiley-Interscience, 1995), 1st edition.

[51] A. F. Oskooi, D. Roundy, M. Ibanescu, P. Bermel, J. Joannopoulos *et al. Meep: A flexible free-software package for electromagnetic simulations by the FDTD method.* Computer Physics Communications **181**, 687 (2010).

[52] A. Farjadpour, D. Roundy, A. Rodriguez, M. Ibanescu, P. Bermel *et al. Improving accuracy by subpixel smoothing in the finite-difference time domain.* Optics letters **31**, 2972 (2006).

[53] V. A. Mandelshtam and H. S. Taylor. *Harmonic inversion of time signals and its applications.* The Journal of Chemical Physics **107**, 6756 (1997).

[54] A. Rodriguez, M. Ibanescu, J. D. Joannopoulos and S. G. Johnson. *Disorder-immune confinement of light in photonic-crystal cavities.* Optics letters **30**, 3192 (2005).

[55] R. Engelen, D. Mori, T. Baba and L. Kuipers. *Two Regimes of Slow-Light Losses Revealed by Adiabatic Reduction of Group Velocity.* Physical Review Letters **101**, 103901 (2008).

[56] M. Patterson, S. Hughes, S. Combrié, N.-V.-Q. Tran, A. De Rossi *et al. Disorder-Induced Coherent Scattering in Slow-Light Photonic Crystal Waveguides.* Physical Review Letters **102**, 253903 (2009).

[57] S. Mazoyer, J. Hugonin and P. Lalanne. *Disorder-Induced Multiple Scattering in Photonic-Crystal Waveguides.* Physical Review Letters **103**, 063903 (2009).

[58] V. Savona. *Electromagnetic modes of a disordered photonic crystal.* Physical Review B **83**, 085301 (2011).

[59] S. Smolka. *Quantum correlations and light localization in disordered nanophotonic structures.* Ph.d. thesis, Technical University of Denmark (2010).

[60] C. Beenakker. *Random-matrix theory of quantum transport.* Reviews of Modern Physics **69**, 731 (1997).

[61] K. Novotny and B. Hecht. *Principles of Nano-Optics* (Cambridge University Press, 2008).

[62] P. Kristensen. *Interaction of light and matter in optical micro structures.* Ph.d. thesis, Technical University of Denmark (2007).

[63] H. Schomerus, M. Titov, P. Brouwer and C. Beenakker. *Microscopic versus mesoscopic local density of states in one-dimensional localization.* Physical Review B **65**, 121101 (2002).

[64] T. Kottos. *Statistics of resonances and delay times in random media: beyond random matrix theory.* Journal of Physics A: Mathematical and General **38**, 10761 (2005).

[65] F. Pinheiro. *Statistics of quality factors in three-dimensional disordered magneto-optical systems and its applications to random lasers.* Physical Review A **78**, 023812 (2008).

[66] N. Vats, S. John and K. Busch. *Theory of fluorescence in photonic crystals.* Physical Review A **65**, 043808 (2002).

[67] L. Andreani, G. Panzarini and J.-M. Gérard. *Strong-coupling regime for quantum boxes in pillar microcavities: Theory.* Physical Review B **60**, 13276 (1999).

[68] Y. Akahane, T. Asano, B.-S. Song and S. Noda. *High-Q photonic nanocavity in a two-dimensional photonic crystal.* Nature **425**, 944 (2003).

[69] S. Mazoyer, P. Lalanne, J. Rodier, J. Hugonin, M. Spasenović *et al. Statistical fluctuations of transmission in slow light photonic-crystal waveguides.* Optics Express **18**, 14654 (2010).

[70] N. Le Thomas, H. Zhang, J. Jágerská, V. Zabelin, R. Houdré *et al. Light transport regimes in slow light photonic crystal waveguides.* Physical Review B **80**, 125332 (2009).

[71] P. Gregory. *Bayesian Logical Data analysis for the Physical Sciences - A Comparative Approach with Mathematica® Support* (Cambridge University Press, 2005).

[72] a. Yamilov and B. Payne. *Classification of regimes of wave transport in quasi-one-dimensional non-conservative random media.* Journal of Modern Optics **57**, 1916 (2010).

[73] R. Carminati and J. J. Sáenz. *Density of States and Extinction Mean Free Path of Waves in Random Media: Dispersion Relations and Sum Rules.* Physical Review Letters **102**, 093902 (2009).

[74] C. Conti and A. Fratalocchi. *Dynamic light diffusion, three-dimensional Anderson localization and lasing in inverted opals.* Nature Physics **4**, 794 (2008).

[75] L. O'Faolain, T. P. White, D. O'Brien, X. Yuan, M. D. Settle *et al. Dependence of extrinsic loss on group velocity in photonic crystal waveguides.* Optics Express **15**, 13129 (2007).

[76] J. Gerard. *Solid-state cavity-quantum electrodynamics with self-assembled quantum dots* (2003).

[77] M. Nomura and S. Iwamoto. *Single Quantum Dot Laser with Photonic Crystal Nanocavity.* Integrated Photonics and pp. 1–3 (2009).

[78] Y. Akahane, T. Asano, B.-S. Song and S. Noda. *Fine-tuned high-Q photonic-crystal nanocavity.* Optics express **13**, 1202 (2005).

[79] M. Winger, T. Volz, G. Tarel, S. Portolan, A. Badolato *et al. Explanation of Photon Correlations in the Far-Off-Resonance Optical Emission from a Quantum-Dot–Cavity System.* Physical Review Letters **103**, 11 (2009).